creative commons
COMMONS DEED

저작자표시-비영리-변경금지 2.0 대한민국

이용자는 아래의 조건을 따르는 경우에 한하여 자유롭게

- 이 저작물을 복제, 배포, 전송, 전시, 공연 및 방송할 수 있습니다.

다음과 같은 조건을 따라야 합니다:

저작자표시. 귀하는 원저작자를 표시하여야 합니다.

비영리. 귀하는 이 저작물을 영리 목적으로 이용할 수 없습니다.

변경금지. 귀하는 이 저작물을 개작, 변형 또는 가공할 수 없습니다.

- 귀하는, 이 저작물의 재이용이나 배포의 경우, 이 저작물에 적용된 이용허락조건을 명확하게 나타내어야 합니다.
- 저작권자로부터 별도의 허가를 받으면 이러한 조건들은 적용되지 않습니다.

저작권법에 따른 이용자의 권리는 위의 내용에 의하여 영향을 받지 않습니다.

이것은 이용허락규약(Legal Code)을 이해하기 쉽게 요약한 것입니다.

Disclaimer

dCollection

공학박사 학위논문

A Study on Suspension-level Vibro-acoustic Performance Evaluation Method for Road Induced Noise

노면 가진 소음 개선을 위한 서스펜션 단위의 음향 및 진동 성능 평가법에 대한 연구

2017 년 12 월

서울대학교 대학원

기계항공공학부

송 현 진

A Study on Suspension-level Vibro-acoustic Performance Evaluation Method for Road Induced Noise

by

David P. Song

A Dissertation
Submitted to the Faculty of

School of Mechanical and Aerospace Engineering

at

Seoul National University

in Partial Fulfillment of
the Requirements for the Degree of

Doctor of Philosophy

December, 2017

ABSTRACT

A Study on Suspension-level Vibro-acoustic Performance Evaluation Method for Road Induced Noise

David P. Song

School of Mechanical and Aerospace Engineering

The Graduate School

Seoul National University

Numerous previous studies have been conducted on quantifying road noise through transfer path analysis (TPA) using the matrix inversion and the dynamic stiffness methods. However, the matrix inversion method is a calculation that always contains error, even when treated with the best condition number found by trial and error iteration to match the calculation SPL (Sound Pressure Level) to measured SPL. Furthermore, the caveat of the dynamic stiffness method is that it

requires accurate dynamic stiffness value up to the frequency range of interest, which, in reality, is rarely available and is challenging to seize. For the sake of cost and time reduction, circumventing these limitations is crucial within the vehicle production period. In this regard, a special suspension rig is devleoped to directly obtain the operational forces at the suspension mounting points neglecting the effect of the vehicle body.

To best utilize this developed rig, a dyno excitation method using precision CNC-milled detachable shell is proposed and its proper operational condition for road noise evaluation is investigated as well. In order to investigate which component plays the biggest role and which component to be prioritized to be tackled, the influence of suspension and body stiffness has on operational force change due to softening the connecting elastomer is studied using the impedance modeling method. Using this method, rig measured dynamic force change which is potentially misleading due to large deviation in dynamic stiffness between the rig and an actual vehicle is also investigated under varying suspension and bush's stiffness combination.

Keywords: Sturcture-borne road noise, Suspension rig, Direct operational force transfer path analysis, Mechanical

impedance method, Dyno excitation method, FRF-based sub-structuring, and Inverse formulation method.

Student Number: 2014-30338

TABLE OF CONTENTS

Page

LIST OF FIGURES

CHAPTER 1

INTRODUCTION

With the continuous increase of the market share of electrical and hybrid vehicles, road-induced noise within a vehicle has become a major NVH issue. Road noise is determined with two categories: the structure-borne noise and the air-borne noise. The latter is in most cases dominated by the tire pattern noise and wind noise at high speed and can be reduced by the use of absorption, insulation, and barrier material. On the other hand, the structure-borne noise is transmitted through a variety of structural pathways (e.g. from tire to knuckle and suspension to body) and radiates into the interior. The structure-borne road noise includes the vibration and harshness frequency region which can cause discomfort in both the driver and the passenger(s). Therefore, the structure-borne road noise is being treated by automotive NVH engineers with great precaution. To attenuate undesirable vibration and noise, transfer path analysis (TPA) has been used as the most ubiquitous and powerful tool to quantify and identify how much of acoustical energy is being transmitted and through which structural pathway. Then, the most dominant transfer path can be modified and

optimized to effectively reduce the structure-borne noise. Typically, within the road noise problem, body mounting point's stiffness and suspension bushes are subject to optimization.

To conduct the structure-borne road noise TPA, operational force is either calculated or estimated, as a dynamic force sensor cannot be installed directly in-between the suspension and the body mounting points. Traditional experimental TPA, since it was developed, the full matrix inversion method and the dynamic stiffness methods have been most ubiquitously used for calculating operational forces [1-4]. H. Douville et al. proposed a method to estimate input force using transmissibility functions to calculate operational force [5-6]. To reduce the experimental time and to improve the reliability of force calculations, A.S. Elliott et al. proposed the 'in-situ source path contribution' method [7]. Also, many studies using hybrid and statistical methods to ameliorate operational force calculation have been carried out by P. Mas et al. [8-9].

In the present study, a special suspension rig is designed to accurately acquire direct operational forces for the structure-borne road noise TPA, because full-vehicle level direct forces cannot be obtained without modifying either or both the suspension and body. Besides, the effort and time for such experiment is not affordable, especially during the vehicle development period. Using this method, the low-frequency structure-borne road noise is evaluated

without a vehicle body. According to Bernd Heibing, the author of Chassis Handbook, two thirds of the structure-borne road noise is decided by suspension input forces into the body [10]. Thus, the possibility to evaluate the chassis' road noise NVH performance at the very early stage of vehicle development (i.e. prior to the very first prototype vehicle which is generally available at least several months after the launch of the project) is a great advantage for NVH engineers.

When evaluating road noise, the excitation method and its reproducibility are extremely important, because the measurement results are always a relative quantity to its excitation. In reality, however, for road noise evaluation, references that assure the excitation quality are limited contrasting to powertrain NVH evaluation: intake temperature, oil temperature, and transmission temperature, etc. are not relevant assuring reference for road noise excitation. As a result, a roller bench excitation method is ubiquitously reconnoitered for sophisticated road noise evaluation.

A few different ways of roller bench excitation approaches for road noise have been studied up to now and the cleat excitation method is one of the most cost-effective and commonly used simple excitation methods [11-12]. Although a cleat excitation could be used for evaluating rolling comfort/harshness, vehicle body motion, out-of-phase vibration (shudder), and axle motion, its

usage is limited, since it is more like an impact excitation and is only suitable for low frequency range excitation (up to 240 Hz). In addition, limited operating speed for experiment is one of the limitations of this method (fast operational speed experiment is not possible due to time interval requirement for signal decay between each impact for signal processing [13-14].

Another excitation approach that was developed for road noise is a molding technique that essentially presses the imprints of the actual road on the dyno. The major disadvantage of this excitation method is that not only the macro texture which induces road vibration is copied, but also the long waviness of the road is also copied, thus creating impractical modulation for every roller rotation. To circumvent this problem, randomly pasted gravel stones on a perfectly circled dyno roller have been developed [15]. As a result, unwanted high amplitude modulation was ameliorated. However, its excitation generates different interior noise and vibration amplitude; hence, its results are not compatible with actual proving ground road excitation. Also, the multi-partial coherent input problem still exists with this method which mandates virtual reference spectrum calculation for the in-depth NVH analysis.

On chapter 3, a CNC-milled detachable shell dyno excitation method which is not only compatible with standard proving ground for road noise excitation, but can also cope with unfixed phase problems between each input

has been proposed and empirically validated. In addition, vibration characteristics due to different excitation methods are compared and explained using the tire models and formula for vehicle dynamic behaviors from previous researches [16-24].

Road-induced vibration is a disturbing NVH problem within the low frequency range which is predominantly transmitted through the suspension structure to the vehicle's body [13]. To improve the NVH performance, two factors can be addressed: first, the operational force that enters the vehicle body or, second, the body's noise transfer function that represents the vibro-acoustic characteristics measured in sound pressure level at a response point over the exerted force at a chassis input point. The operational force that enters to the vehicle's body is generally described by the suspension, whereas the body's noise transfer function (NTF) performance up to structure-borne road noise frequency (scoped up to 300 Hz in this study) is largely influenced by the structure, material, and cavity of the vehicle's cabin.

One of the most ubiquitously performed strategies to improve the structure-borne road noise is optimizing the dynamic properties of bushing at a dominant acoustic energy transfer path, as two thirds of the road noise are conquered by suspension to the body input operational forces [10,25]. To closely attend to the problem of improving the operational force, Song et al. developed a suspension rig for practically obtaining the direct force at hard

points, neglecting the vehicle's body and hence solely assessing a suspension's vibro-acoustic performance [24]. The basic schematic representation of the developed suspension rig is shown in Figure1.1.

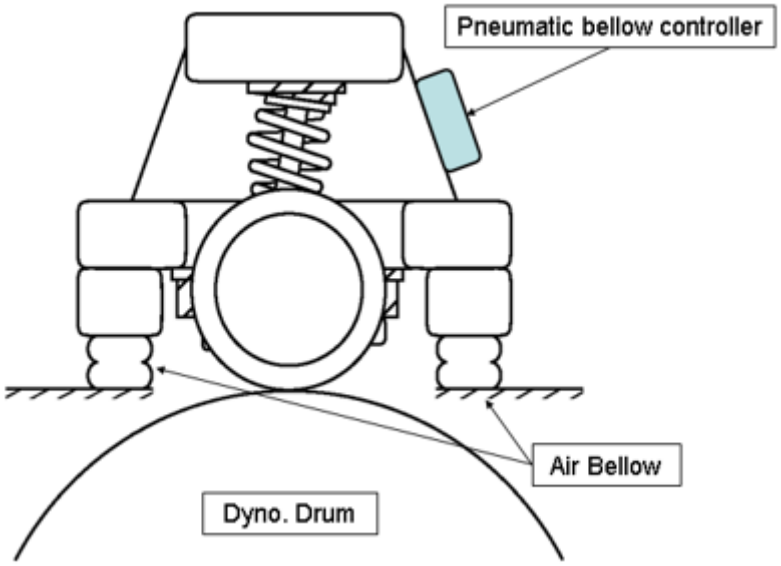

Figure 1.1 Schematics of developed suspension rig for the direct operational force measurement

The principal concept for the rig is that a chassis system is mounted on a heavy structure settled on a relatively soft riding-height adjustable spring air bellow, so that the road induced operational force flows towards the rig, hence neglecting the vehicle body's influence under the actual operational condition. This is achieved by maximizing the impedance of the attachment points for preventing the local deformation effect and isolating transmitted force at the

passive (rig) side. Separating the effect of the vehicle body from the chassis system is definitely an advantageous method for optimizing suspension's vibro acoustic performance (e.g. through benchmarking testing with a better performing system). However, further investigation of the influence that the vehicle body attachment point has on the use of the suspension rig method is, as suggested by Kim et al., is still necessary [26-28]. This suggests that potentially misleading results can be drawn for improving chassis NVH performance when countermeasures are drawn based on the rig testing method. In other words, the improvement achieved from the rig measurement might not be achieved when performed in the actual vehicle testing.

Consequently, to investigate the potential problem mentioned above, in the present study, a suspension coupled to a vehicle body via an elastomer is modeled using the impedance method. Generally, the term impedance is used to describe the relationship between the current and voltage within an electrical circuit, though, in a mechanical system modeling, the definition of the impedance is stretched to be represented by using the frequency response function-based relationship. Each element, which makes up the whole mechanical system when rigidly coupled, is in this regard represented by the input over output [29-31]. As compared to many other modeling methods, the usage of this modeling method has several advantages in terms of tackling aforementioned problem.

Typically, the finite element modeling technique cannot guarantee the accuracy up to the interest frequency of road-induced noise; neither the statistical energy analysis method, nor the asymptotic modal analysis method is suitable for accurately predicting the dynamic behavior under scoped frequency range [32-33]. Otte has proposed the dynamic compliance based sub-structuring method which uses measured FRF of each sub-structure from free-free condition to calculate coupled system's responses [34-35]. Furthermore, Jiantie, Lim, and Lu have provided the inverse formulation method to calculate the connecting stiffness properties between two sub-structures based on measured transfer functions from the total structure and validated the results by both single and multi-coordinate coupling cases [36]. However, the accuracy of these studies has only been validated within a simple or theoretical applications and lacks in practicality when applied to real-world automotive NVH problems (e.g. road noise).

The impedance modeling method proposed on chapter 4 uses measured mechanical impedance (or dynamic stiffness) value which can be obtained within an assembled system, since the modeling assumes each element is represented by its point impedance and is connected via a simple linear formation. Henceforth, changing one element does not alter the impedance of other elements, which is not the case for the dynamic compliance based sub-structuring method. Using the impedance modeling method, a numerical study

is performed to investigate achievable force reduction due to bush optimization under different systems with different properties of the impedance combination. Following the numerical study, the proposed impedance coupling model is validated for actual road excitation application by comparing the estimated and measured force changes between two different suspensions for two different locations: McPherson strut type suspensions in lateral arm Y direction and Multilink type rear suspension in front mount X direction which represent the extremely stiff and the extremely soft coupling cases within typical passenger vehicle suspension, respectively.

In order to improve the road induced noise, throughout the development of vehicles, NVH engineers typically go through many trial and error tasks and many repeated and redundant experiments. The actual body input force due to road excitation is fundamentally caused by both vibration transmitted through the suspension and the effect of the vehicle body at the suspension coupling point. To this end, Kang and Song had deployed a new methodology of the road noise performance evaluation technique using the suspension rig. This rig enables for separate tackling of these influence factors by identifying the vibro-acoustic performance of a sole suspension neglecting the influence of the body coupling effect [24, 37].

While the ability to separately and simultaneously tackle the suspension and the body side is an absolute advantage, this scheme has a limitation. Specifically, after obtaining the force distribution and contribution, it is still necessary to identify which component of the suspension is most practical and inexpensive in terms of maintaining the ride and handling quality (as too much of softening joint bushings negatively influences the vehicle's dynamic behavior). Therefore, it is essential to derive the most effective and practical solution for the road noise improvement factor. Another consideration that needs to be taken into consideration using the rig is that it is inevitable to consider the suspension to rig coupling effect in order to more precisely bring the countermeasures driven from the rig measured data to the actual full vehicle system. In response to these caveats, in the present study, the frequency response function-based substructuring (FBS) method is applied, as it is a well-known typical approach for solving structure-related problems [38-41].

FBS is a method to predict the dynamic characteristics of a target system by relating those of individual subcomponents and those of an assembly system. The studies concerning FBS are far-reaching in various fields [38-40]. Among the variety of different approaches within the FBS method, the most common approach uses the Receptance Coupling method, also known as the RC method, which synthesizes the FRF of an assembly system with the use of two

independent substructures [38]. In chapter 5, the feasibility of using this method to suspension improvement factor derivation is assessed. A cradle with four mout bushings is modeled using FRF-based substructuring theory and each bushing's dynamic stiffness property is extracted using the inverse formulation method. Then, a bushing that contributes to road noise problem the most is prioritiezed by means of joint bushing stiffness sensitivity analysis.

CHAPTER 2

A METHODOLOGY FOR EVALUATING THE STRUCTURE-BORNE ROAD NOISE PRIOR TO A PROTOTYPE VEHICLE USING DIRECT FORCE MEASURED ON A SUSPENSION RIG

2.1 Introduction

In the present study, a special suspension rig is designed to accurately acquire direct operational forces for the structure-borne road noise TPA, because full-vehicle level direct forces cannot be obtained without modifying either or both the suspension and body. Besides, the effort and time for such experiment is not affordable, especially during the vehicle development period. Using this method, the low-frequency structure-borne road noise is evaluated without a vehicle body. According to Bernd Heissing, the author of Chassis Handbook, two thirds of the structure-borne road noise is decided by suspension input forces into the body. Thus, the possibility to evaluate the chassis' road noise NVH performance at the very early stage of vehicle development (i.e. prior to the very first prototype vehicle which is generally

available at least several months after the launch of the project) is a great advantage for NVH engineers. Directly measured forces using proposed method is compared with two indirectly calculated forces towards the end of this chapter.

2.2 Structure-borne road noise transfer path analysis

TPA is a technique that allows to trace the transmission of vibro-acoustic energy from one location, through transfer pathways, to another location. The goal of TPA is to evaluate the energy contribution along each path from the source to the receiver, making it possible to identify which path is critical for noise and vibration transmission. This technique has been ubiquitously used by vehicle NVH engineers to evaluate cabin noise. A pressure target response of cabin noise can be expressed as follows:

$$\mathrm{P}_{\mathrm{receiver}} = \sum_{i=1}^{n} \mathrm{P}_i = \sum_{i=1}^{n} \mathrm{F}_i \times \frac{\mathrm{P}_i}{\mathrm{F}_i}, \tag{2.1}$$

where $\mathrm{P}_{\mathrm{receiver}}$ represents the cabin noise response caused by the structure-borne road noise, which can be calculated by the sum of Noise Transfer Function (NTF) from i to n paths multiplied by exerted operating force at that path of suspension mounting points. Although the most accurate and precise way to obtain the operating forces is the direct measurement method, directly

measuring operational force is not suitable within an actual vehicle due to its limited installation room availability between the chassis and body mounting points.

2.2.1 Operational force calculation

2.2.1.1 Full matrix inversion method

The most frequently used indirect operational force calculation method is the 'full matrix inversion method'. Calculating operational forces using this method can be expressed as follows:

$$\mathrm{F}(\omega) = [\mathbf{H}(\omega)]^{-1} \times a(\omega) \tag{2.2}$$

where $\mathbf{H}(\omega)$ represents the transfer function between the target and the force applied at each transfer path location and, $a(\omega)$ is accelerating spectrum acquired at the passive side (*e.g.* in particular, for road noise TPA, attached at body side of mounting points) of each transfer path location during operating condition. Although this method does not require mount-stiffness curves, the singular value decomposition (SVD) technique has to be utilized to invert the transfer function matrix. The transfer matrix $[\mathbf{H}(\omega)]$ can be decomposed into $m \times m$ unitary matrix $[\mathbf{U}(\omega)]$, $n \times n$ unitary matrix $[\mathbf{V}(\omega)]^{\mathrm{T}}$, and $m \times n$

matrix with non-negative real diagonal term matrix $[\sum(\omega)]$, which can be written in mathematical form as follows:

$$[\mathbf{H}]_{m\times n} = [\mathbf{U}]_{m\times m}[\sum]_{m\times n}[\mathbf{V}]^{\mathrm{T}}_{n\times n}, \tag{2.3}$$

where *m* is the number of responses and *n* is the number of sources and, at all time, the number of response should be equal or larger than the number of sources in order to calculate operational forces. The singular value, σ, can be interpreted as a different independent phenomenon acting in the system and it is ordered from large to small on the diagonal matrix $[\sum]_{m\times n}$ (larger singular value would bring more information as compared to smaller singular values at each frequency) (see Eq. (2.4)).

$$[\sum]^{-1}{}_{m\times n} =$$

$$\begin{bmatrix} \sigma_1^{-1} & 0 & \cdots & 0 \\ 0 & \sigma_2^{-1} & \cdots & 0 \\ \vdots & \vdots & \ddots & \vdots \\ 0 & 0 & \cdots & \sigma_n^{-1} \end{bmatrix}. \tag{2.4}$$

The matrix inversion by the SVD technique is very prone to error and raise noise rate. The operational force calculation is thus controlled with a proper threshold condition number. The condition number can be written as follows:

$$\text{Condition\_number} = \sigma_1/\sigma_n. \tag{2.5}$$

All forces calculated using the matrix inversion method are treated with relative 1% condition numbers, which is the most ubiquitous threshold criterion used for eliminating noise when there is a large difference between σ_1 and σ_n.

2.2.1.2 Dynamic stiffness method

Although the dynamic stiffness method is an accurate way to calculate operational forces and is frequently used to check TPA results, it can be only used for the soft mount force calculation with the availability of a precise dynamic stiffness value. Mathematically, obtaining operating forces using the dynamic stiffness method can be summarized with the hooks law (see Eq. (2.6)):

$$\mathrm{F}_i(\omega) = \mathrm{K}_i(\omega) * \frac{\left[\mathrm{a}_{\mathrm{i,active}}(\omega) - \mathrm{a}_{\mathrm{i,passive}}(\omega)\right]}{-\omega^2} \tag{2.6}$$

where $-\left[\mathrm{a}_{\mathrm{i,active}}(\omega) - \mathrm{a}_{\mathrm{i,passive}}(\omega)\right]/\omega^2$ represents the bush deformation obtained by double integration of relative acceleration spectra in *i* direction and $\mathrm{K}_i(\omega)$ represents the dynamic stiffness of the bush in *i* direction.

2.2.2 Road noise trnasfer paths diagram

The structure-borne road noise is induced from the interaction of the tire and the road surface which transmits the acoustical energy and vibration through wheel knuckle to damper strut, spring, and sub-frame which, ultimately,

excites the vehicle body. Typically, to evaluate the structure-borne road noise, the chassis to body attachment hard points are set to be the transfer paths, because it is crucial to know how much force is actually exerted into the body. In the present study, McPherson strut front sub-frame which is mounted to the body through damper top, front mount, and rear mount, and trailing arm rear sub-frame which is mounted to the body through trailing arm, damper top, front mount, and rear mount, are examined. Figure 2.1 shows the transfer path diagram of tested suspension.

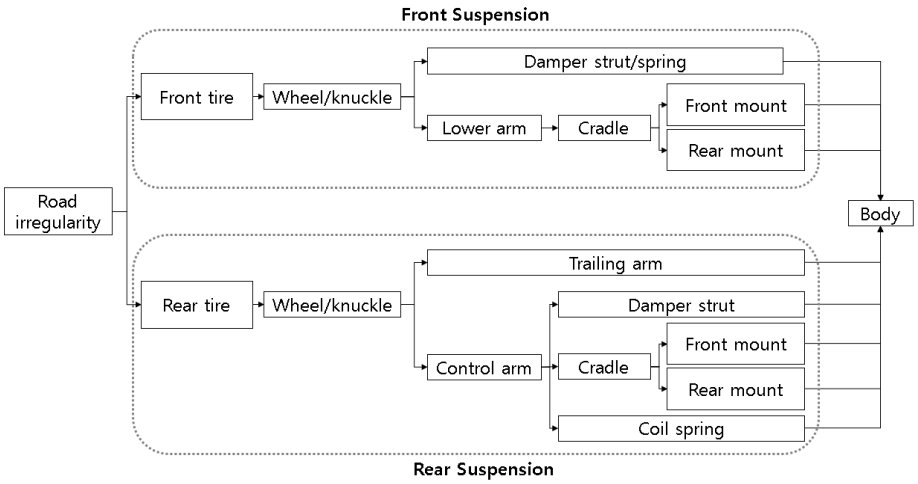

Figure 2.1 Road noise transfer paths diagram of tested suspension (Front suspension: Mcpherson strut; Rear suspension: Trailing arm).

2.3 Direct operational force measurement on suspension rig

2.3.1 Suspension force rig properties

To directly measure operational forces, a special chassis force rig has been developed (see Fig. 2.2). This special rig is a rigid heavy mass structure balanced and leveled by four Festo's air bellow EB-215-155 controlled by pneumatic controller to keep the suspension in position during the entire operation. The bellow is regulated by the developed pneumatic circuit to bellow with constant air pressure once set. Hence, the influence of the bellow to knuckle input and chassis oscillation is prevented. Also, due to its extremely high stiffness and rigidity, operational forces measured on this rig neglect the structure's local or global resonance effect up to 700 Hz. This covers the main frequency range of interest for the structure-borne road noise or is also known as rolling noise. Thus, when operational forces are picked up by using this developed rig, it should be pure chassis force itself which goes into the vehicle's body.

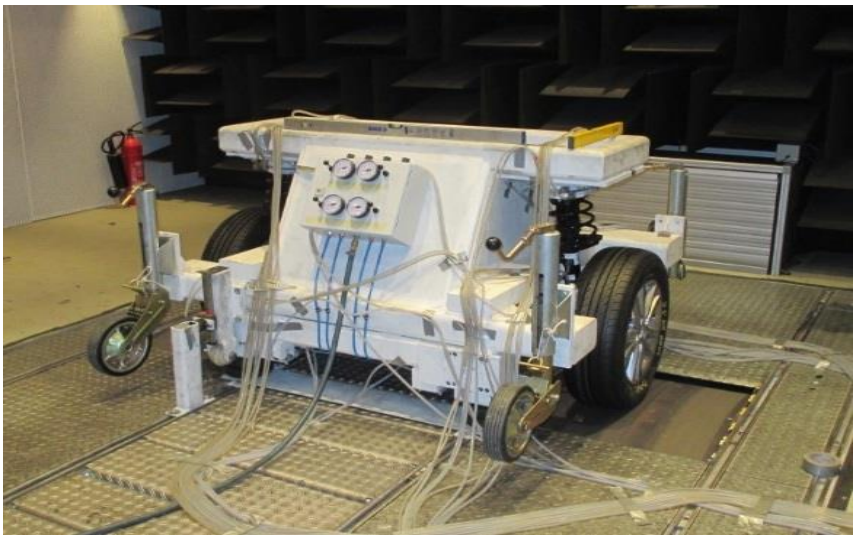

Figure 2.2 Developed suspension rig for the direct operational force measurement.

2.3.2 Experimental setup

The force rig is designed in a way to make it capable of testing different types of suspensions with swapping adapter block sets (e.g. different adapter block sets for front axle and rear axle). Adapter blocks are made by CNC with the CAD data of chassis to body mounting points. These data should be available at an early stage of the vehicle development process, since the hard points get freezes as soon as the vehicle chassis concepts are defined. There are some cases where the 5 axis CNC cut is necessary (e.g. damper top) which is somewhat more time-consuming than other blocks; however, the whole process

of adapter block preparation for a vehicle (both front and rear axle) should be within two weeks.

Two adapter rings for each PCB 260A02 ICP tri-axial force transducer are made to keep the sensor precisely centered and ensure that all sensors do not touch the bolt; in this way, entire forces are measured correctly as it would be installed into an actual vehicle. The tested front suspension and rear suspension have 10 and 14 chassis-to-body connecting points, respectively: 3 points within each side damper top and 4 sub-frame mounting points on the front suspension; 2 points within each damper top, 2 points within each trailing arm, spring, and 4 sub-frame mounting points on the rear suspension. Also, to verify the direct operational force measurement, a PCB 356A15 ICP tri-axial acceleration sensor has been installed on both active (chassis) and passive (body) side (see Fig. 2.3). These two acceleration spectra will later be used to indirectly calculate the operational forces with the dynamic stiffness method.

Direct operational force measurement experiment is conducted on a chassis dynamometer in a semi-anechoic chamber. To assess a variety of vehicle dynamic movements, including ride comfort, body hop, oscillate in the opposite phase, and axis movements, a 20 mm × 8 mm (width × height) cleat bar has been installed on both sides of the dyno roller (see Fig. 2.4a).

The 8 mm impact bar is used for following four evaluation standard excitations: rolling comfort/harshness, vehicle body motion, out-of-phase vibration (shudder), and axle motion. The cleat bar test is known to excite 0-240 Hz frequency range hence, following vibration phenomena are expected: rigid body mode, wheel knuckle resonance, tire modes, and tire cavity resonance. The suspension is leveled by adjusting the pressure on four air bellows and settled with the correct ride height by measuring the distance of the sub-frame from the top of the dyno roller surface (see Fig. 2.4b). The operational speed is maintained at 30 km, so that the tire goes over the impact bar fast enough to excite the suspension up to 250 Hz and slow enough so that the second impact followed by the first impact occurs after complete decay. The impact is captured using B&K laser tacho probe MM-0360 (see Fig. 2.5).

Ten impact signals are linearly averaged to be evaluated with each impact processed with 30% pre-triggered Hanning window. For signal acquisition, resolution is set at 1 Hz and phases are referenced to the right side knuckle acceleration in the positive vertical direction for all data. The comparison between direct measured operational forces obtained on the suspension rig and the calculated forces dynamic stiffness (supplier provided) method applied on the suspension rig on the front suspension front mount is shown on Fig. 2.6.

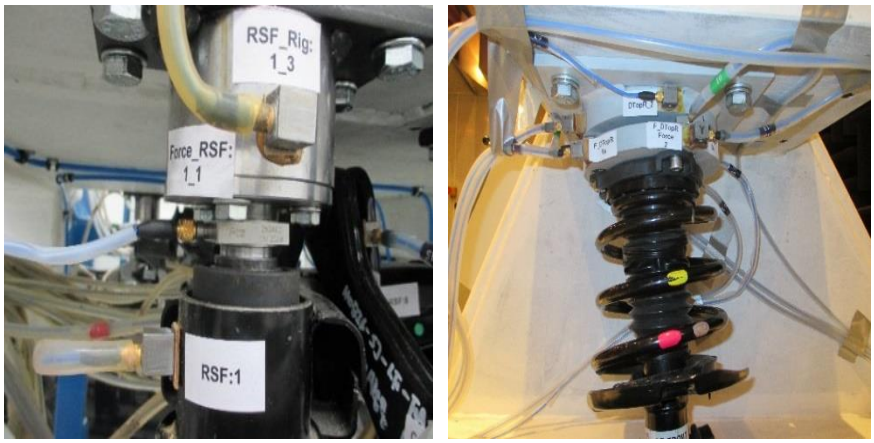

(a) (b)

Figure 2.3 Installed force transducer and two acc. sensors on (a) Rear suspension rear mount; (b) Damper top.

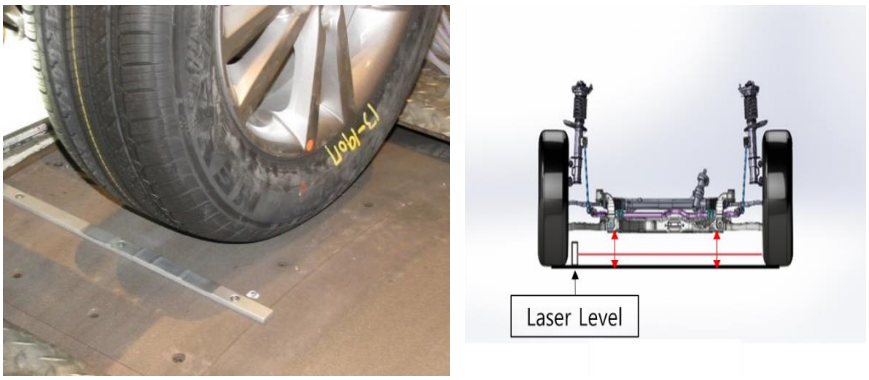

(a) (b)

Figure 2.4 (a) Impact bar on dyno drum; (b) Front suspension leveling with laser level.

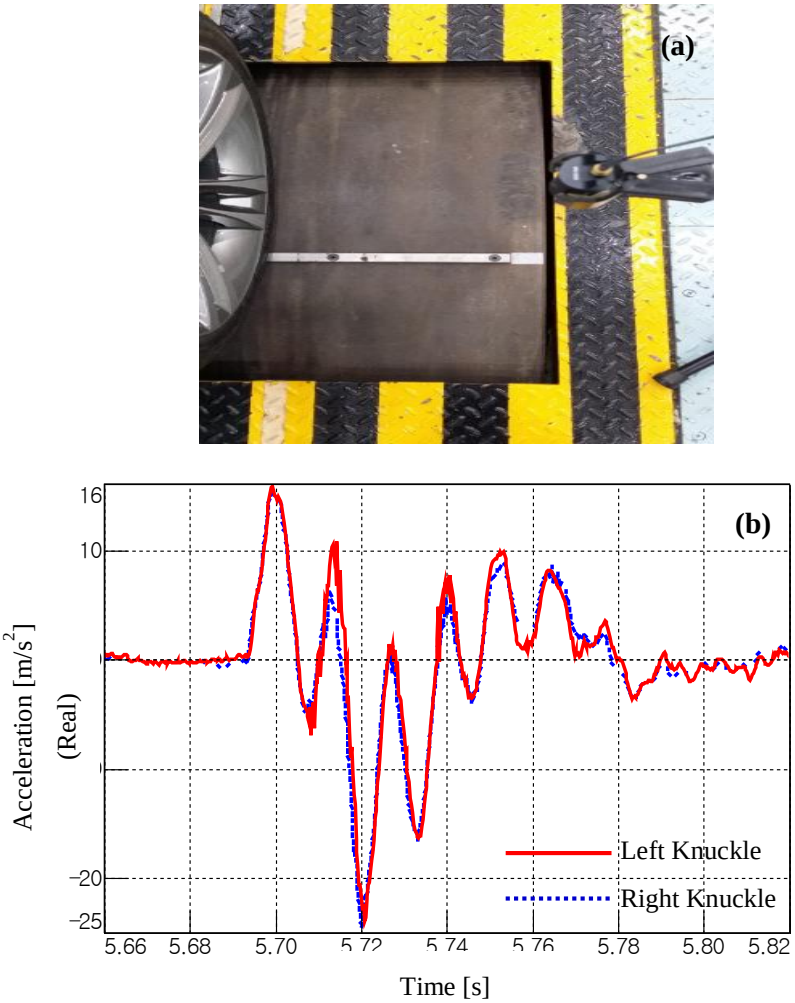

Figure 2.5 (a) Impact bar experiment trigger setup using B&K laser tacho probe; (b) Impact signal time data comparison between left (solid red) and right (dotted blue) knuckle in the vertical direction.

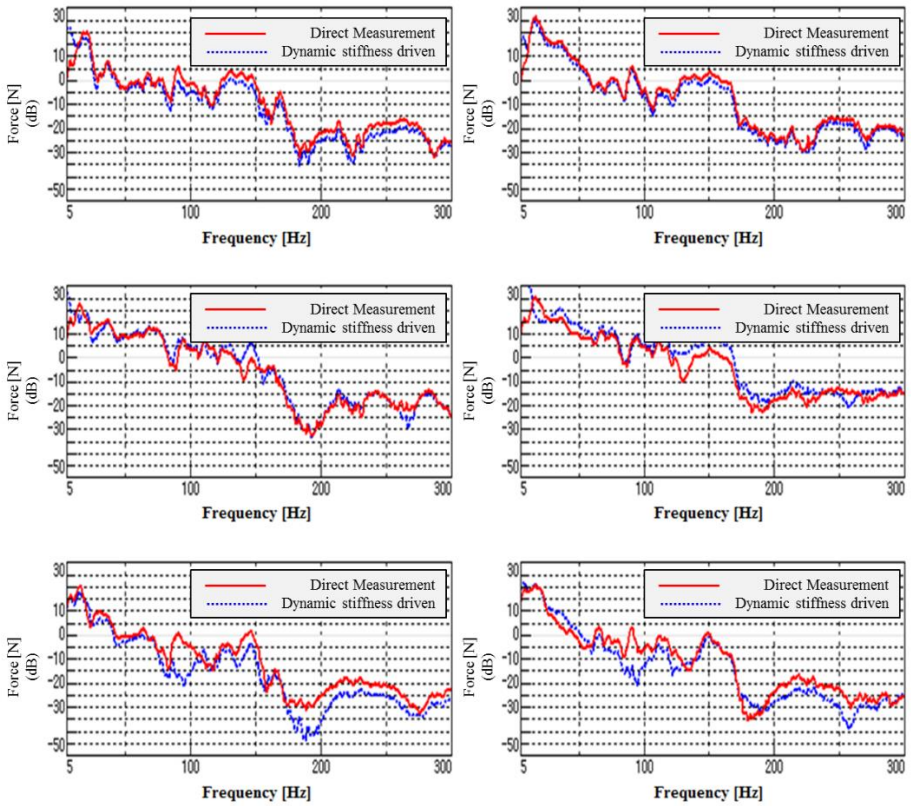

(a) (b)

Figure 2.6 (a) Front suspension rear mount force in x, y, z direction (respective from top to bottom) comparison - (a) Left side; (b) Right side; [dB Ref: 1N] Legend: (red solid) Direct measurement on suspension rig; (blue dotted) Indirect calculation using the dynamic stiffness method applied on the suspension rig;

2.4 Knuckle acceleration spectrum comparison between the baseline vehicle and suspension rig measurements

Prior to comparing the operational forces acquired by three different methods, the knuckle acceleration spectrum measured between the baseline vehicle and the suspension force rig is analyzed first. The baseline vehicle experiment is conducted in the same anechoic-chamber at the same speed using exactly the same impact bar as the suspension rig measurement. Also, to keep the experimental conditions maximally similar, all signals are processed with exactly the same scheme and all operational forces and accelerations are phase-referenced to the vertical knuckle acceleration. Figure 2.7 shows the baseline vehicle experiment setup.

To compare the knuckle acceleration spectrum, the first baseline vehicle test is conducted; then, suspension is removed from the vehicle to install it on the suspension rig. After the data are obtained on the suspension rig, the suspension is then reinstalled back onto the vehicle to observe how much the 'uninstalling and installing process' affects the dynamic acceleration. Fig.2.8 shows the comparison of the front knuckle spectrum among the baseline vehicle, suspension rig, and repro of baseline vehicle after the suspension reinstallation. The distance between each grid in y-axis amounts to 10 dB; note that the

vertical direction phase is seen as a straight line, because it is used as the reference. Important peaks, such as wheel hop around 18 Hz, wheel rotational resonance around 45 Hz, and tire cavity resonance around 200 Hz, seem to be legitimately measured; moreover, all spectra in general agree with each other. Since the entire experiment setup is kept the same, the only possible explanation for the acceleration deviation between the baseline test and the baseline repro test is due to uninstalling and reinstalling process of suspension.

Figure 2.7 Baseline vehicle impact bar experiment setup in an anechoic chamber

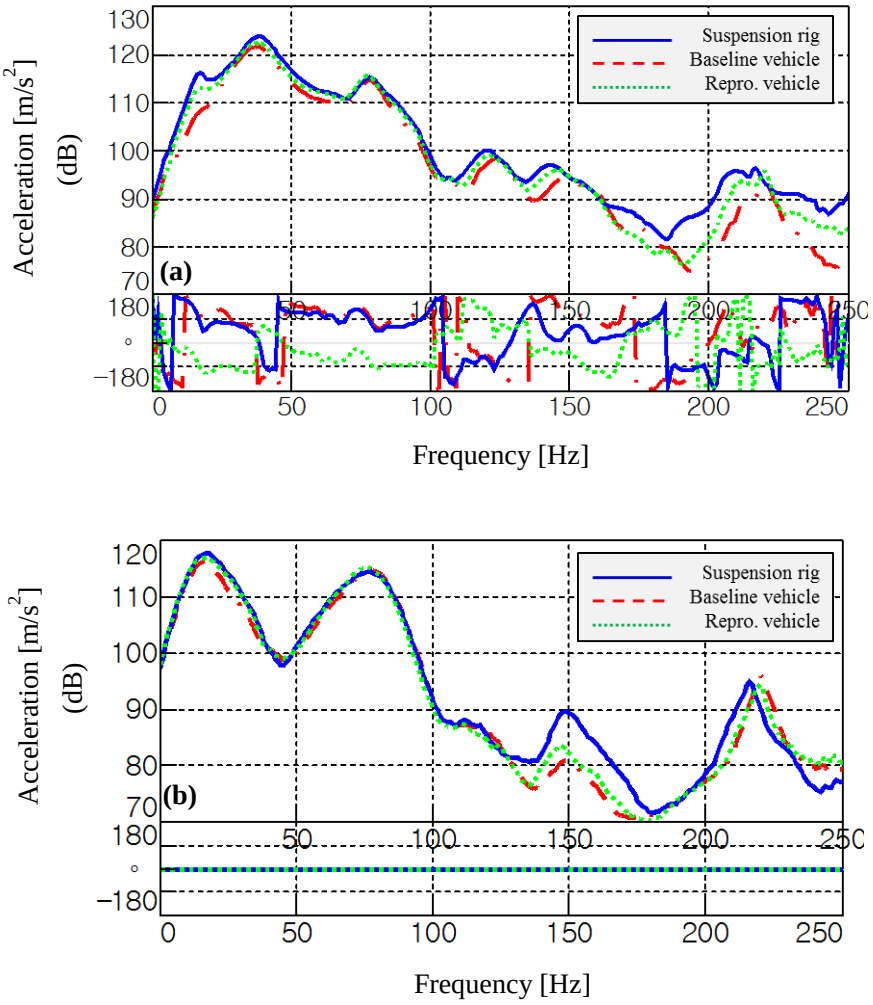

Figure 2.8 (a) Front suspension right side knuckle acceleration in longitudinal direction comparison; (b) Front suspension right side knuckle acceleration in vertical direction comparison.Legend: (blue solid) Suspension rig; (red coarse dash) Baseline vehicle; (green fine dash) Baseline vehicle repro after reinstalling the suspension.

2.5 Operational force comparison acquired by the three methods

Directly obtained forces on the suspension rig have been verified through a comparative analysis with indirectly calculated forces using the matrix inversion method from the baseline vehicle and indirectly calculated forces using the dynamic stiffness value (see Fig. 2.9). The distance between each tick in y-axis is 10 dB. As expected, the directly measured operational forces and indirectly calculated operational force using the dynamic stiffness method on the suspension rig are almost identical and the maximum deviation is within 5 N in dB scale. This deviation is presumably caused by an inaccuracy of the provided dynamic stiffness, the experimental setup differences in operational condition, or the effect of mounting rubber bush installation onto the sub-frame; however, the deviation is acceptable in any case. Forces below 50 Hz cannot be calculated using dynamic stiffness, as a relative movement measured between the active and the passive side is close to zero at lower frequency range; hence, multiplication of dynamic stiffness to mount deflection converges to zero. This is another superiority of direct force method using developed rig.

Indirect force calculation using the dynamic stiffness method applied on the baseline vehicle (see green fine dashed curve in Fig. 2.9) also matches fairly

well with the directly obtained force curve (red curve); however, some deviation is observed at a few peaks and the deviation seems to become larger as it goes to a higher frequency. The possible causes for this deviation are effect of vehicle body and suspension uninstalling and installing effect though, this amount of difference is adequate and acceptable considering that main usage of this rig is within the early stage of vehicle development.

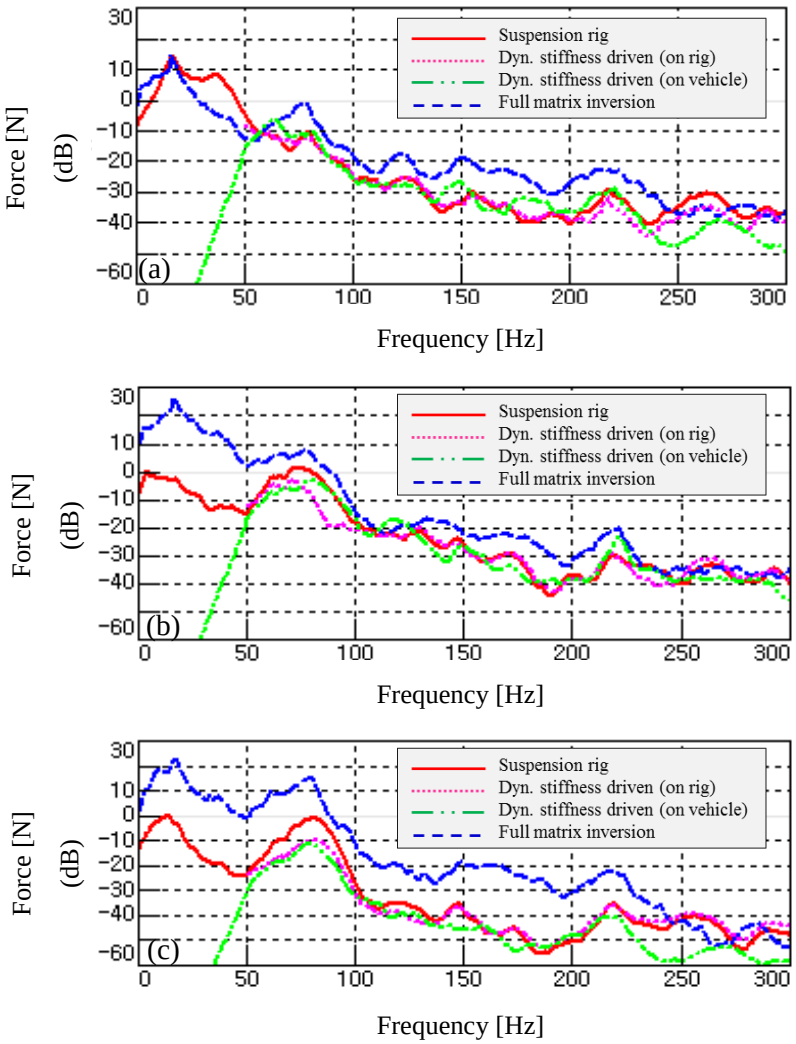

Figure 2.9 Front suspension front mount force comparison in (a) longitudinal direction; (b) lateral direction; (c) vertical direction [dB ref. 1 N]. Legend: (red solid) Direct measurement on the suspension rig; (pink dotted) Indirect calculation using the dynamic stiffness method applied on the suspension rig; (green dash-double dotted) Indirect calculation using the dynamic stiffness method applied on the baseline vehicle; (blue dashed) Indirect calculation using the full matrix inversion method

2.6 Estimation of structure-borne road noise

An accurately evaluation of the cabin noise caused by road-induced excitation requires not only the pure direct operational force from chassis to body, but also an accurate body noise transfer function (NTF). Although it is not possible to precisely estimate the cabin noise with one of two factors missing, having operational force prior to the vehicle body is still a great advantage for NVH engineers when used with following two options: (1) using predicted NTF output from CAE; and (2) using roughly averaged measured NTF from the previous version of the vehicle in the same platform.

The primary aim is to validate the direct force method using the rig; thus, the measured body NTF is used for the interior SPL calculation. Half-inch B&K 4942-A-021 diffuse field microphone and B&K 8206-002 impact hammer with rubber tip were used for this measurement. Figure 2.10 shows the comparison of measured and calculated interior noise at 30km/h rear axle roll. The red curve represents the baseline measurement (measured SPL), the blue curve represents the calculated SPL using direct force obtained from the rig, and the green curve shows the calculated SPL with the matrix inversion method. The dynamic stiffness method was not included in the comparison, because it is only valid for calculating forces at a certain path (e.g. sub-frame mount with rubber).

Although, in general, the SPL calculated with direct forces better match the baseline (measured SPL in full vehicle), there are perceptible deviations throughout the target frequency range. The possible causes for this phenomenon may be related to an inaccuracy in the NTF measurement and the effect of the uninstalling and reinstalling process of suspension. Coster and Franz stated that the NTF results can vary up to 5 dBs below 200 Hz due to the use of different excitation methods (*e.g.* from shaker to impact hammer). In addition, the person who carries out the NTF measurement, excitation angle, and the position of the sensor could also cause errors in the NTF measurement.

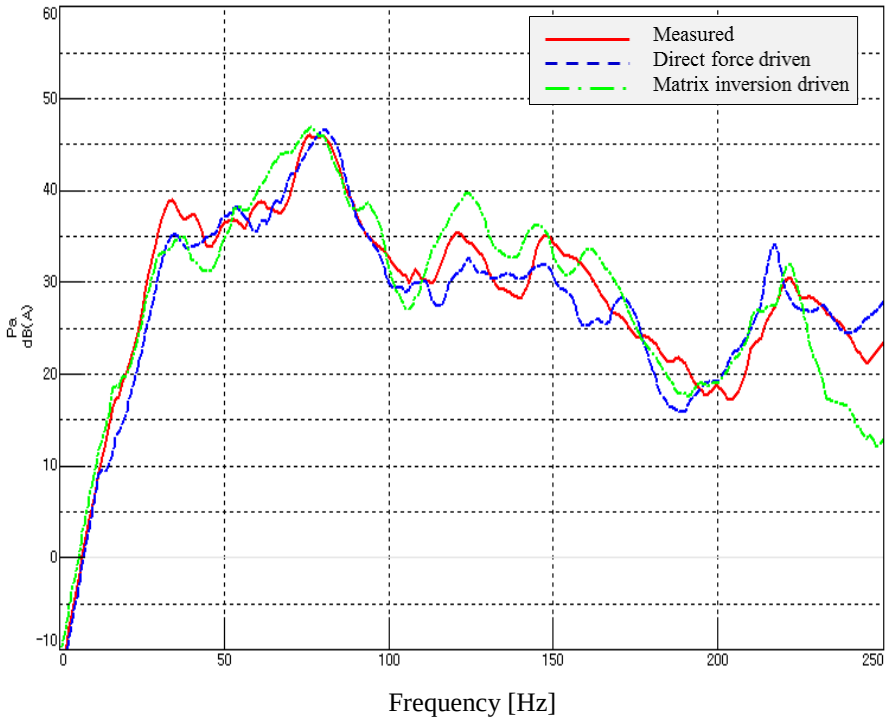

Figure 2.10 Interior SPL comparison at 30kmh rear axle roll. Legend: (red solid) Measured SPL; (blue dashed) Calculated SPL using direct forces; (green dash dotted) Calculated SPL using matrix inversion method (calculated with no extra indicator with relative 1% condition number)

2.7 Benchmarking technique: suspension level dynamic stiffness extraction

One of the best uses of the suspension rig developed in the present study is for benchmarking analysis of the competitor's suspension. Through a direct comparison of the competitor's suspension and developing suspension, the improvement factor can be seized. By simply substituting measured force and mount deflection (measured by two accelerometers as shown on Fig. 2.3) into Eq. 6, the dynamic stiffness value can be extracted (see Fig. 2.11). Y-axis denotes the dynamic stiffness value (N/mm) in log scale and x-axis denotes frequency in linear scale. Actual dynamic stiffness values are hidden for security purposes.

The third-degree polynomial curve fitted technique and the peak hold technique are applied to get rid of outliers that are predominantly caused by low excitation transmitted to the mount. Having actual dynamic stiffness values to cross reference for the developing suspension at the very early stage of vehicle development is certainly a huge advantage for NVH engineers. From this particular experimental case, it appears that the developing suspension's mount is much stiffer in all three directions than that of competitors and, thus, NVH engineers can use these data to negotiate with R&H engineers to bring down its

stiffness. The reported case is just one simple example of how to make use of the developed suspension rig through establishing the chassis road noise performance improvement factor.

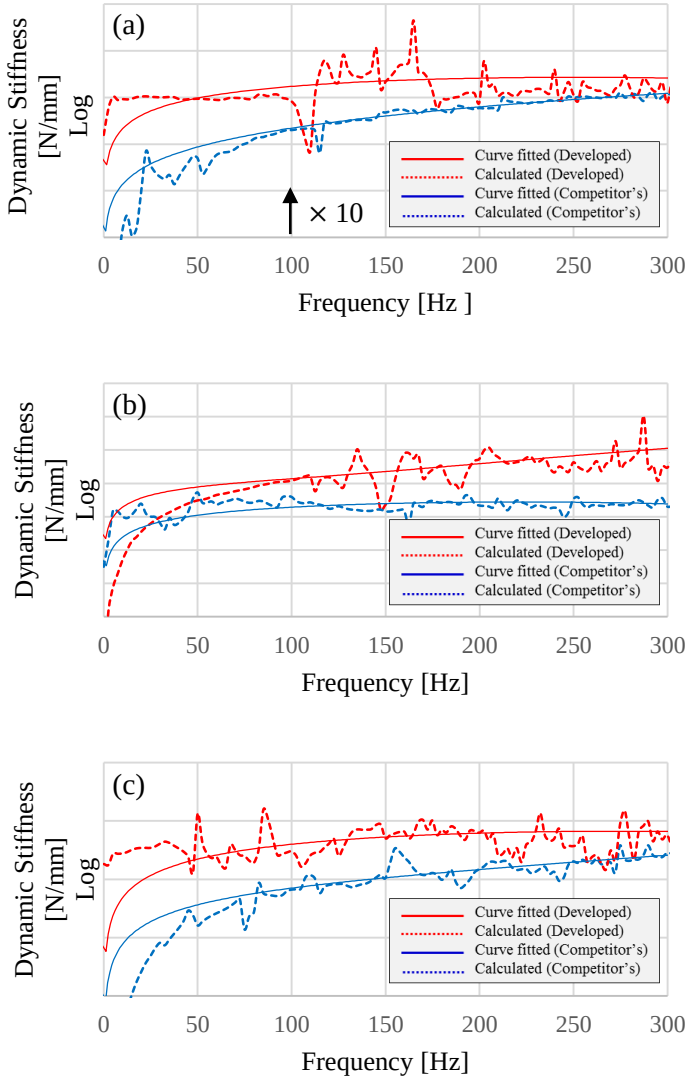

Figure 2.11 Comparison of the competitor's and developing rear suspension front mount dynamic stiffness. Legend: (red dotted) Calculated dynamic stiffness of developing suspension; (red solid) Curve fitted dynamic stiffness of developing suspension; (blue dotted) Calculated dynamic stiffness of competitor's suspension; (blue solid) Curve fitted dynamic stiffness of competitor's suspension;

2.8 Summary

In this chapter, a special suspension rig has been developed to measure direct operational forces primarily for estimating the structure-borne cabin noise prior to the production proto vehicle. The rig has been verified by cross-referencing the knuckle acceleration spectrum measured on the baseline vehicle and the forces calculated by indirect methods up to 250 Hz. The comparison between the knuckle acceleration spectrum of the baseline vehicle and the suspension rig illustrates that the signal is almost identical in both vertical and longitudinal directions.

Directly obtained forces using the force rig are then compared to the calculated forces using two different indirect methods (dynamic stiffness and the full matrix inversion method). The results of the comparison clearly demonstrate that the forces obtained with the direct measurement method are almost identical to those obtained with the dynamic stiffness method applied on the suspension rig. When this dynamic stiffness method is applied on the baseline vehicle, some deviations are observed; however, most of major peaks agree with direct forces. Although the calculated force using the matrix inversion method can be optimized by selecting and omitting singular values and doubling or even tripling the indicators into the TPA model, the directly

obtained force is the most accurate and reliable way to obtain the road noise input forces.

The dynamic stiffness of mount bushing is extracted on the suspension level using measured direct forces and mount deflection. The third degree polynomial curve fitting technique is used for smoothing out the curve and peak hold technique is used for where not much deflection has occurred at the mount. Theses extracted mount dynamic stiffness values allow NVH engineers to seize improvement factors for road noise NVH performance of developing suspension and make a smarter compromise with R&H engineers possible.

Vehicle road induced noise is always a relative measure related to the specific road surface; thus, the forces obtained with a cleat excitation represent only at that specific operational condition. In this regard, various excitation surfaces have to be adopted for indoor road noise evaluation process. This work is currently under progress using a 3-D laser scanning and precise milling technique to replicate several different actual road conditions to our dyno roller. Also, the estimation of effect of the suspension's structural modification on vehicle rolling noise using the rig to full vehicle correlation and the inertance method is currently under progress as well.

CHAPTER 3

A VALIDATION STUDY OF THE DETACHABLE SHELL DYNO EXCITATION METHOD FOR STRUCTURE-BORNE ROAD NOISE EVALUATION

3.1 Introduction

When evaluating road noise, the excitation method and its reproducibility are extremely important, because the measurement results are always a relative quantity to its excitation. In reality, however, for road noise evaluation, references that assure the excitation quality are limited contrasting to powertrain NVH evaluation: intake temperature, oil temperature, and transmission temperature, etc. are not relevant assuring reference for road noise excitation. As a result, a roller bench excitation method is ubiquitously reconnoitered for sophisticated road noise evaluation.

A few different ways of roller bench excitation approaches for road noise have been studied up to now and the cleat excitation method is one of the most cost-effective and commonly used simple excitation methods. Although a cleat excitation could be used for evaluating rolling comfort/harshness, vehicle body

motion, out-of-phase vibration (shudder), and axle motion, its usage is limited, since it is more like an impact excitation and is only suitable for low frequency range excitation (up to 240 Hz). In addition, limited operating speed for experiment is one of the limitations of this method (fast operational speed experiment is not possible due to time interval requirement for signal decay between each impact for signal processing.

Another excitation approach that was developed for road noise is a molding technique that essentially presses the imprints of the actual road on the dyno. The major disadvantage of this excitation method is that not only the macro texture which induces road vibration is copied, but also the long waviness of the road is also copied, thus creating impractical modulation for every roller rotation. To circumvent this problem, randomly pasted gravel stones on a perfectly circled dyno roller have been developed. As a result, unwanted high amplitude modulation was ameliorated. However, its excitation generates different interior noise and vibration amplitude; hence, its results are not compatible with actual proving ground road excitation. Also, the multi-partial coherent input problem still exists with this method which mandates virtual reference spectrum calculation for the in-depth NVH analysis.

In this chapter, a CNC-milled detachable shell dyno excitation method which is not only compatible with standard proving ground for road noise

excitation, but can also cope with unfixed phase problems between each input has been proposed and empirically validated.

3.2 Road Excitation: structure-borne road noise evaluation

Typically, a structure-borne road noise is evaluated under several different constant speed operations because in reality, the straight test track length is practically not long enough to provide wide variation of speed operation. With limited track length, several constant speed operation measurements are often measured, which is very inefficient for road noise evaluation. Figure 3.1 shows the left and right front knuckle acceleration in three directions measured on standard proving ground with different speeds starting from 40 km/h (All results are plotted in dB scale with reference of 1 m/s^2). When the vehicle reaches a speed of 40 km/h and higher, the excitation generated by powertrain can be simply neglected as the road induced noise become dominant. The driver has strived to keep the vehicle in exactly the same lane for each measurement which in reality, is difficult and time-consuming. Under the assumption that all the excitation was kept the same for all measurements, one could immediately observe changes in the characteristics of 95 Hz peak in vertical direction as vehicles speed changes from 40 km/h to 60 km/h. This phenomenon might have been not captured if not all operational speeds have been tested.

Unlike powertrain measurement where many reference signals can be interpreted for the quality of the excitation, only knuckle signal is selected for road excitation reference signal. Hence, the reproducibility of the excitation is critically important for investigating the modification effect for road noise. Deviated excitation may generate huge differences when performing the in-depth NVH analysis, *e.g.* TPA or ODS that require phase reference signal. Few well-known disadvantages of conventional road noise TPA using the full matrix inversion method are: erroneous operational force calculation due to matrix inverting process, time-consuming uninstalling and reinstalling process of input side and response side for transfer function acquisition, and requiring many extra indicator sensors than define the number of path for reliable accuracy. The operational force, $\mathrm{F}(\omega)$, can be calculated by using the full matrix inversion method by using Eq. (3.1)-(3.2):

$$\mathrm{F}(\omega) = [\mathbf{H}(\omega)]^{-1} \times a(\omega) \ . \tag{3.1}$$

where $\mathbf{H}(\omega)$ is the transfer function matrix and $a(\omega)$ respresents the operational acceleration at a defined transfer path. To invert the transfer function matrix, the singular value decomposition (SVD) technique is used.

$$[\mathbf{H}]_{m\times n} = [\mathbf{U}]_{m\times m}[\sum]_{m\times n}[\mathbf{V}]^{\mathrm{T}}_{n\times n}. \tag{3.2}$$

Where the $[\mathbf{H}]_{m\times n}$matrix is decomposed into $m\times m$ unitary matrix, $[\mathbf{U}]$, $n\times n$ unitary matrix $[\mathbf{V}]^{\mathrm{T}}$, and $m\times n$ non-negative real singular value diagonal matrix,

$$[\sum]^{-1}{}_{m\times n} = \begin{bmatrix} \sigma_1^{-1} & 0 & \cdots & 0 \\ 0 & \sigma_2^{-1} & \cdots & 0 \\ \vdots & \vdots & \ddots & \vdots \\ 0 & 0 & \cdots & \sigma_n^{-1} \end{bmatrix}. \quad (3.3)$$

where *m* represents the number of responses and *n* represents the number of sources. The singular value, σ, contains independent phenomenon acting in the system and it is ranked from large to small on the diagonal matrix $[\sum]_{m\times n}$. The ratio between the largest to smallest singular value is called condition number and is defined as

$$\text{Condition\_number} = \sigma_1/\sigma_n. \quad (3.4)$$

The signal to noise ratio is controlled by changing the condition number and the results changes operational force calculation. Small singular values are often omitted to increase the accuracy of the operational force calculation. Additionally, the over-determination method is also used to increase the accuracy of the operational load calculation. This can be expressed as follows (see Eq. (3.5)):

$$\begin{Bmatrix} \mathrm{F}_1^{oper} \\ \mathrm{F}_2^{oper} \\ \vdots \\ \mathrm{F}_n^{oper} \end{Bmatrix}$$

$$= \begin{bmatrix} \mathbf{H}_{(1,1)} & \mathbf{H}_{(1,2)} & \cdots & \mathbf{H}_{(1,n)} \\ \mathbf{H}_{(2,1)} & \mathbf{H}_{(2,2)} & \cdots & \mathbf{H}_{(2,n)} \\ \vdots & \vdots & \ddots & \vdots \\ \mathbf{H}_{(n,1)} & \mathbf{H}_{(n,2)} & \cdots & \mathbf{H}_{(n,n)} \\ \mathbf{H}_{(n+1,1)} & \mathbf{H}_{(n+1,2)} & \cdots & \mathbf{H}_{(n+1,n)} \\ \vdots & \vdots & \ddots & \vdots \\ \mathbf{H}_{(m,1)} & \mathbf{H}_{(m,2)} & \cdots & \mathbf{H}_{(m,n)} \end{bmatrix} \begin{Bmatrix} \mathrm{a}_1^{oper} \\ \mathrm{a}_2^{oper} \\ \vdots \\ \mathrm{a}_n^{oper} \\ \mathrm{a}_{n+1}^{oper} \\ \vdots \\ \mathrm{a}_m^{oper} \end{Bmatrix} \tag{3.5}$$

where F^{oper} is the load at each path intended to be calculated, a^{oper} is the acceleration at that location under operational condition. By over determining the matrix by extending responses to *m*, *n* forces can be estimated with improved accuracy.

Nevertheless, all this effort of indirectly calculating operational load within a complicated system where the path contains nonlinear parts like damper, spring and bushings is not only imperfect but also exceedingly time-consuming. Hence, this conventional TPA using the matrix inversion method is often not viable to be performed during the vehicle development period. To circumvent these limitations, the empirical approach of 'detachable TPA' and 'direct force acquisition rig approach' can be used in combination with the proposed CNC-milled detachable shell excitation.

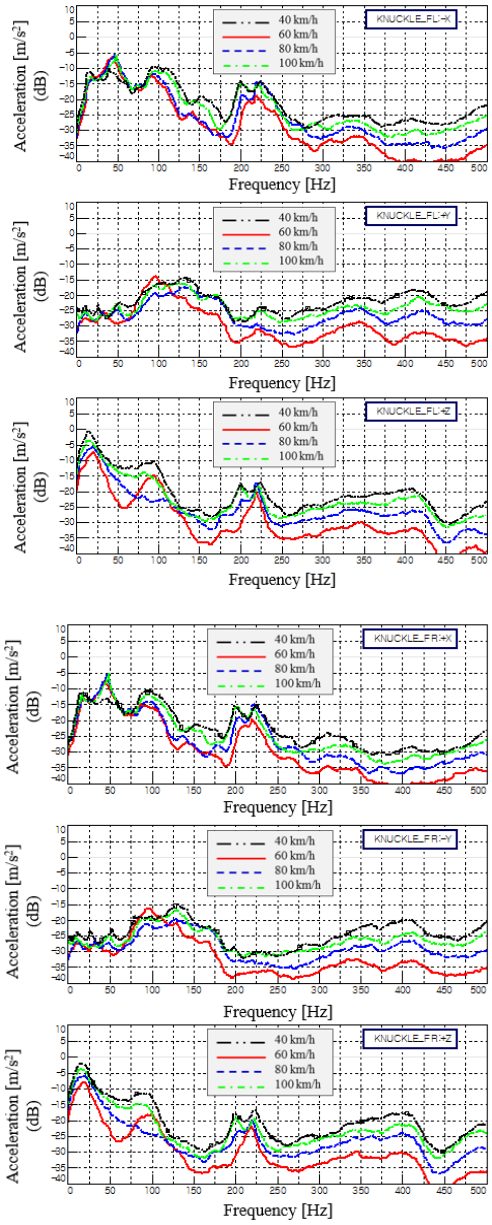

Figure 3.1 Front knuckle autopower at different vehicle speeds measured on standard rough proving ground. (black dash double dotted line) 40 km/h (red solid line) 60 km/h (blue dashed line) 80 km/h (green dash dotted line) 100 km/h

3.3 Dyno excitation method: precision CNC-milled detachable replicated road shell

AICON Breuckman 3D laser scanner was used for replicating exact print of proving ground surface and converted to digital data. 10 m stretches of three different proving ground surfaces (standard, smooth, and rough) shown in Figure 3.2 were scanned for validation study in this paper. Then, the long wave unevenness was filtered out using spline interpolation and averaging techniques. Detailed technical criteria information was omitted in this paper however, averaging values and interpolation length were chosen with the following considerations:

Insufficient long wave reduction of the profile will generate unrealistic repeated periodic modulation and heave motion when installed on dyno. On the other hand, excessively smoothed profile perchance changes in structural noise and vibration transmission characteristics if there is not enough excitation in amplitude to break the damper's static friction.

Figure 3.3 shows the comparison between the originally scanned surface profile and the filtered profile with two different averaging and spline interpolation length on a 10 m dyno roller. This filtered profile was used for the direct precision CNC mill and was fabricated in arched plate shells surrounding

the dyno roller (see Figure 3.4). This milled surface ring was then cut into plates (16 for 3.18 mØ and 9 for 1.68 mØ) for the installation and uninstallation purposes. One important consideration that was taken into account when separating the shell plates was the order effect due to it divided plates. In this regard, plates were precisely fabricated at each plate-to-plate connection and carefully installed on the dyno. The installation process shall not exceed an hour for mounting 16 plates on to the dyno when two people are in labor simultaneously. The ability to remove and change the excitation surface is another advantage of the proposed method, since it broadens the usability of dyno facility without limiting the objectives of the experiments.

To investigate road noise issue, techniques such as TPA and/or ODS analysis are ubiquitously performed. Such tasks require phase information; hence, a reference point has to be selected. Typically, input signal is chosen for the phase reference point which contains sufficient correlation to other measurement points. For road noise evaluation, however, due to multiple coherent input issue, selecting one input as the phase reference point is not inappropriate. This problem can potentially be circumvented if fixed phase relation among each input excitation is achieved. For this purpose, the left and right side surface is mirrored about the longitudinal axis, so that the excitation between the left and right wheel can be in the fixed phase relation when a

vehicle is exactly set on the middle of the dyno. In-phase excitation is prone to generate a higher interior sound pressure level; thus, this was also taken into account when profile filtering values were chosen for achieving compatible excitation amplitude level to the actual road excitation and fixed phase relation between inputs simultaneously. Figure 3.5 depicts the detachable road shell installed on all-wheel drive dyno set up for in-door road noise excitation.

(a) (b) (c)

Figure 3.2 Proving ground road surface profile with three different roughnesses. (a) Smooth (b) standard rough (c) rough

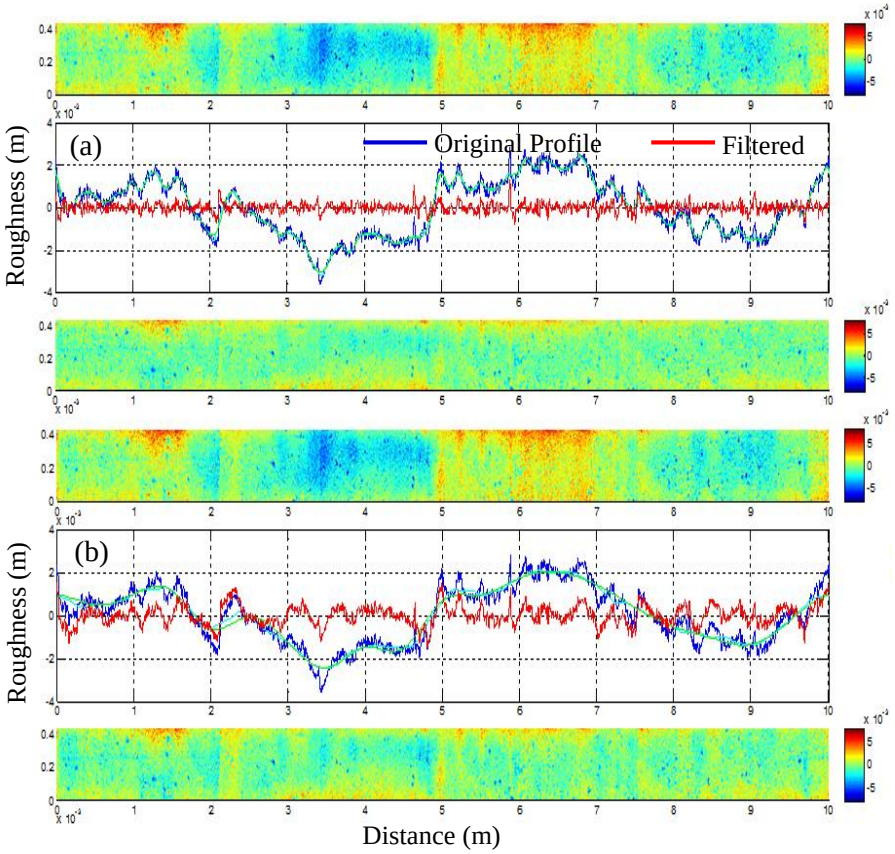

Figure 3.3 Original 10 m scanned surface profile and long wave filtered out profile comparison. (a) Averaging with 0.1 m length spline interpolation points; (b) averaging with 0.5 m length spline interpolation points.

Figure 3.4 CNC-milling process of road surface into arched plates.

Figure 3.5 Detachable shell installed on dyno for indoor structure-borne road noise excitation.

3.4 Experimental setup

3.4.1 Measurement equipment and sensor locations

For validation purposes, the same spec wheel and tire (235/45/R18 94V Bridgestone Potenza) sets were installed on the test vehicle for both front and rear wheels. The test vehicle had McPherson front suspension and trailing-arm type rear suspension. A PCB 356A15 ICP tri-axial accelerometer was installed on each knuckle and one extra accelerometer was installed on for each front and rear sub-frame for coherence study. Four half-inch B&K 4942-A-021 diffuse field microphones were installed in the following positions for cabin noise measurement: (1) driver's seat; (2) passenger's seat; (3) VIP seat, and (4) rear center. Figure 3.6 shows the acceleration measurement points used for both proving ground and in-door dyno measurements. Data acquisition was carried out with SCL220 SIEMENS LMS SCADAS for indoor dyno measurement and LMS mobile SCADAS for proving ground actual road measurement.

To achieve a high reproducibility and in-phase excitation between the left and right knuckle, the vehicle was set on the exact same position for all measurement using a one-point fixation device. The vehicle was attached to this fixation device at the front towing eye through an elastic rubber molding that minimizes the vehicle's

constrain effect in both transverse and longitudinal directions. The vertical direction of the vehicle can be moved freely, so that ideal actual driving condition is maintained, e.g. for heave motion and load changes (for powertrain measurement). By mounting the one-point fixation device at specific position defined for the baseline measurement, the testing vehicle is constrained at the exact same position for every measurement. A previous study has demonstrated that the one-point fixing method does not influence dynamic behavior and interior noise of the vehicle up to the frequency range of interest for structure-borne road noise as compared to the conventional constraining method, a tie-down strap fixing method. Figure 3.7 shows the test vehicle constrained on the dyno using the one-point fixing device.

Figure 3.6 Acceleration measurement points for dyno excitation method validation. (a) Front knuckle (only right side shown on the picture); (b) rear knuckle (only right side shown on the picture); (c) front cradle; (d) rear cradle.

Figure 3.7 One-point vehicle constraining device for dyno excitation measurement.

3.4.2 Operational condition for dyno measurement

Dyno measurements are conducted under idling engine in neutral transmission position, so that the transmission dose not heat up when the dyno forces to roll the vehicle to avoid any damages in transmission. The effect of engine idle is negligible as its amplitude is subtle compared to tire-road interaction excitation on rough surface rolling measurements and, if necessary, its dominant frequency can be simply traced and removed. Prior to all measurements, the tire pressure is checked and warmed up by repeating run-up/run-down between the minimum and maximum speed of intended measurement operational speeds.

The dyno excitation using CNC milled shell generates periodically repeated excitation of every roller circumferential length (10 m for the larger roller and 5.27 m for the smaller roller, in this particular case, see Figure 3.8). Therefore, in contrast to actual road random-like excitation, periodical harmonic excitation is generated on dyno. Using the frequency-wavelength relation

$$f = v/\lambda, \tag{3.6}$$

where f is the frequency, v is the rolling speed of the wheel, and λ is the wavelength, roller's harmonic components at varying speed with different roller size can be calculated (the first order component of dyno roller rotation gives the frequency of 6.3 Hz at the maximum velocity within the measurement of 120 km/h for a 5.27 m roller). Run up/run down operational condition essentially averages out unwanted roller's harmonic frequencies and therefore all peaks in the measured spectra are only related to the vehicle. This effect is further elaborated in Figure 9 (both signals are averaged 20 times over 10 seconds with 1 Hz of resolution). The vertical knuckle signal obtained during stationary shows a rippled peak like a noisy spectrum, while rundown operational condition shows a smooth curve. This plot clearly depicts that rippled peaks from stationary speed operation is ameliorated with rundown operation since it's components are solely due to road-to tire induced vibration. However, the following aspect needs to be considered when this averaging approach: a quasi-static condition of each time window is required for sufficient frequency resolution as the

vehicle speed and the roller's diameter determines the frequency band of roller's harmonic components. In this paper, to achieve 1 Hz resolution, 1 km/h/s run up operation is performed from 20 km/h to 120 km/h and signal is tracked with 0.5 km/h increments. In addition, 50 % averaging overlap for Hanning window is used as it is an optimal overlap value for typical vibration analysis.

The phenomena around 95 Hz peak that was observed from the actual road test (see Figure 3.1) are quickly and intuitively identified on the color map plot using a wide speed range operation using dyno excitation, as shown in Figure 3.10. (For road noise evaluation, run down/run up excitation will give the same results and, therefore, can be used for reproducibility quality check). 20 – 120 km/h wide range of varying speed is measured in one single run on dyno. Then, the data are processed further for identifying the best matching compatible operational condition to stationary proving ground measurement.

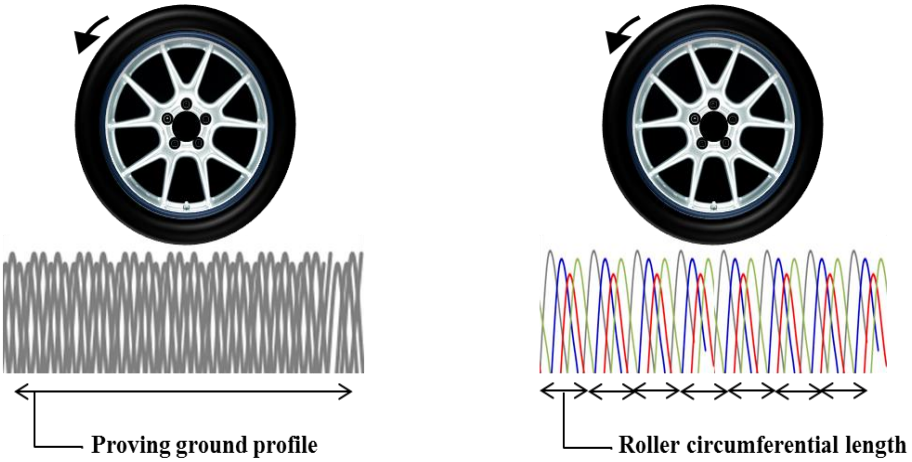

Figure 3.8 Excitation comparison between actual proving ground road and CNC- milled detachable shell dyno.

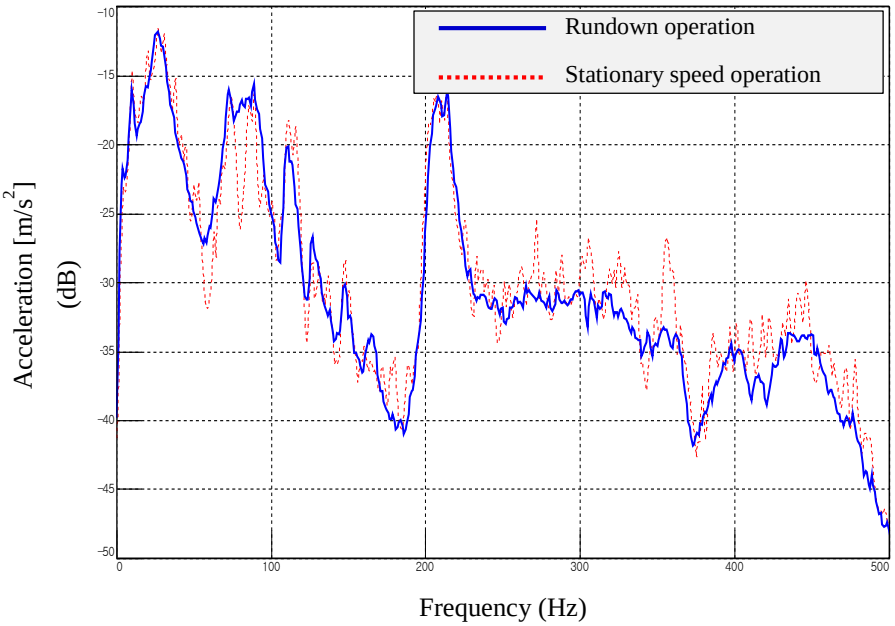

Figure 3.9 Comparison of vertical knuckle Autopower obtained under stationary speed of 30 km/h (red dashed line) and rundown (blue solid line) operational condition on dyno excitation.

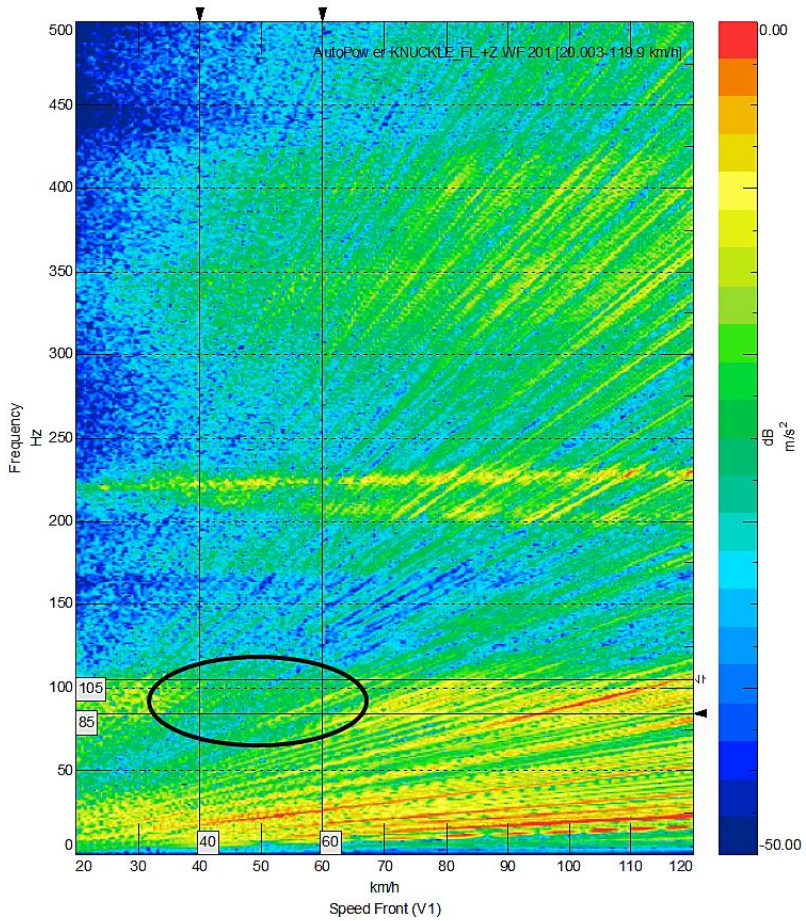

Figure 3.10 Colormap plot of front knuckle Autopower in vertical direction measured on dyno with standard rough surfaces.

3.4.3 Operational condition for proving ground measurement

Actual proving ground experiment was conducted under the constant velocity condition and cruise-control was used to maintain such condition. To assure vehicle's

operating speed during the measurement, tire's first order was reverse calculated (e.g. circumference of 235/45/R18 tire used in this paper gives 2.1 m and, thus, the first tire order at 60 km/h is 7.93 Hz) and checked on longitudinal direction knuckle signal, where the first tire order could be observed.

By contrast to dyno measurement, the engine was engaged to the transmission throughout the experiment in order to maintain the constant velocity. The highest gear was engaged in order to minimize its possible influence on the measurement. The measured data were processed with 2 averages per second and processed with 1 Hz resolution over 10 s duration, for all 40 km/h, 60 km/h, 80 km/h, and 100 km/h operation.

3.5 Influence of dyno roller size

One of the major concern using the replicated profile shell excitation method was the unrealistic contact area between the roller and tire that might not generate realistic actual road excitation and, hence, the interior noise, if the size of the roller is too small. To investigate this, two different setups were made (see Figure 3.11) for comparison. With the use of the one-point fixing device, the position of the vehicle was exactly and conveniently secured going back and forth between these two set ups (for reproducibility check of the excitation).

Energy averaged knuckle signal in vertical direction obtained under 20-120 kmh runup on the rough surface is plotted in Figure 3.12. Front axle on 3.18 mØ (which automatically puts the rear axle on 1.68 mØ) is represented in the blue curve and vice versa for the red. The spectrum shows that not perceptible difference was observed on the front knuckle; however, when the rear axle was set on the smaller roller, vertical direction knuckle acceleration was observed to be slightly overestimated as compared to when it was set on the larger roller in-between 300-450 Hz. To further investigate this phenomenon, the colormap was plotted (see Figure 3.13) for the rear knuckle measurement in all three directions on different roller sizes.

As it could be seen in Figure 3.12, vertical direction rear axle acceleration measured on the smaller roller is higher than that measured on the larger roller. Also, the lateral direction excitation shows similar results. The difference becomes perceptible as the vehicle goes up to higher speed towards 120 km/h. However, a clear explanation of the root cause still cannot be drawn, even with analyzing the colormap and the fact that this effect was not observed on the front axle cannot be explained. It is possible that it is also affected by the combination of the vehicle's suspension type and its weight distribution, which possibly creates a different effect as the contact area between the tire and the roller changes. To validate this finding, further experiments are necessary in order to clarify this phenomenon, with several

sets of different test vehicles with different suspension types. Once these data are available, perhaps the analysis of the effect of tire contact patch, stick-slip effect, and even suspension geometry can be performed using a theoretical model and formulation. The necessity of investigation is clear and well understood; however, exploring this issue is excluded for future study.

However, this phenomenon results in causing maximum 5 dB(A) differences in cabin noise in the given frequency range (see Figure 3.14). To minimize the overestimated order effect at higher speed, the dominant axle in this frequency range should always be measured on the larger roller for the future measurement in order to get the best matching result to actual road measurement.

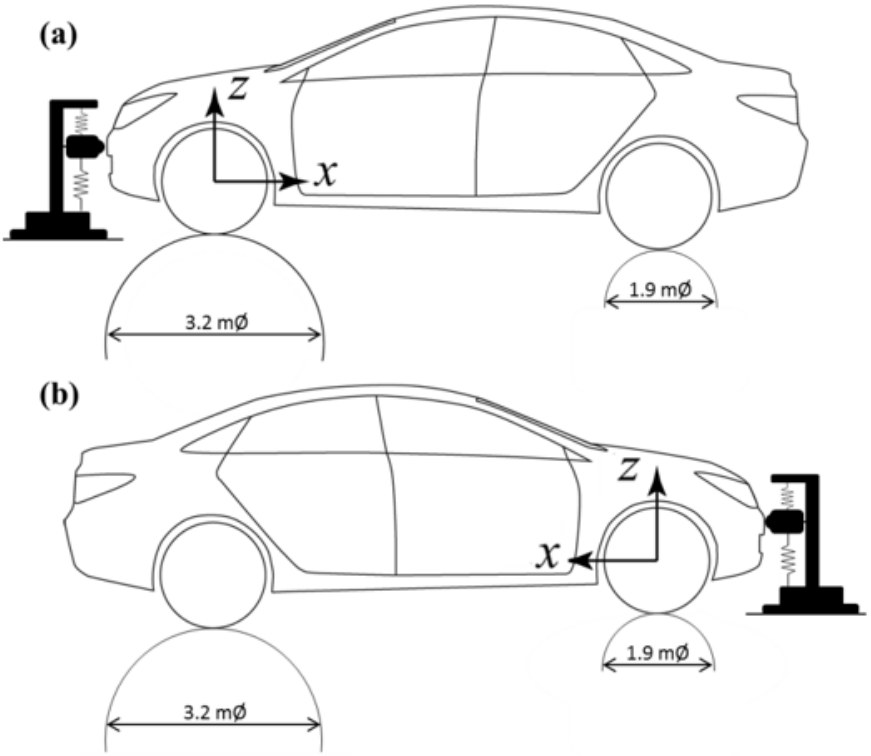

Figure 3.11 Experimental setup for investigating the influence of dyno size on excitation. (a) front axle on 3.2 mØ roller; (b) rear axle on 3.2 mØ roller

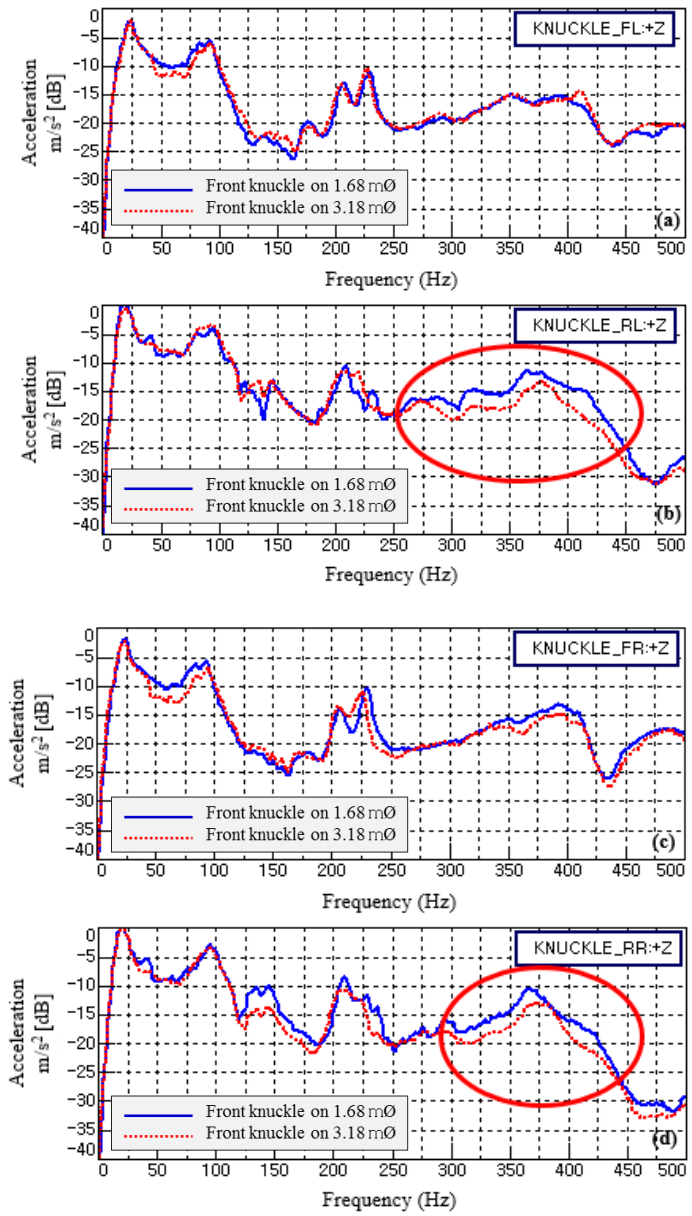

Figure 3.12 Rough surface measured knuckle acceleration comparison in vertical under 20-120 km/h run-up operation. (red dotted) front knuckle on 1.68 mØ (blue solid) front knuckle on 3.18 mØ. (a) front left knuckle; (b) front right knuckle; (c) rear left knuckle; (d) rear right knuckle

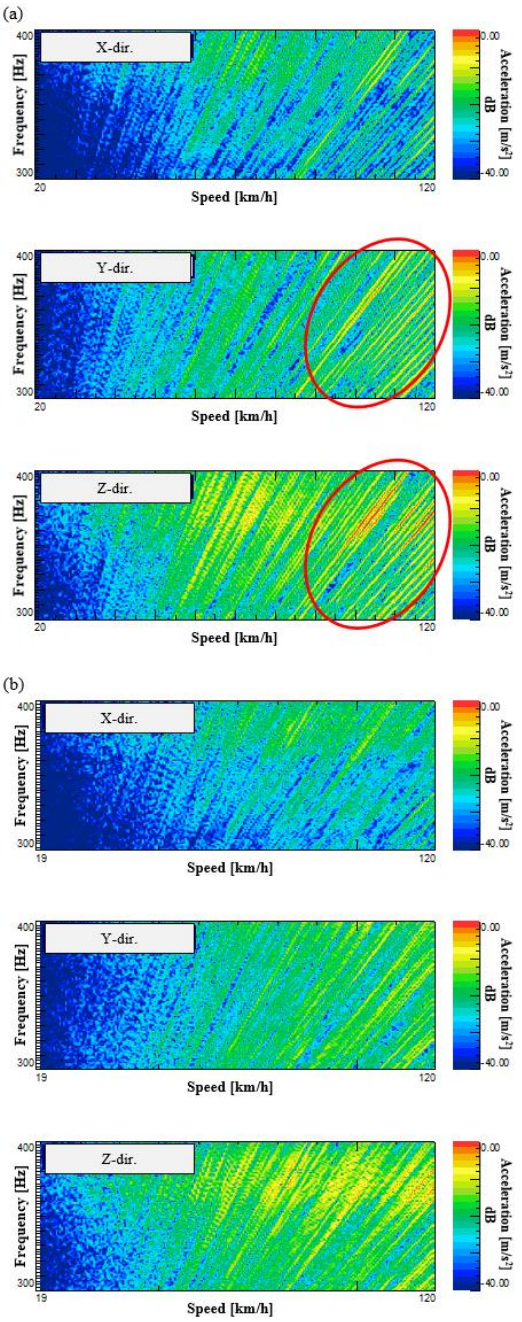

Figure 3.13 Rear knuckle acceleration colormap comparison measured on (a) 1.68 mØ roller (b) 3.18 mØ roller.

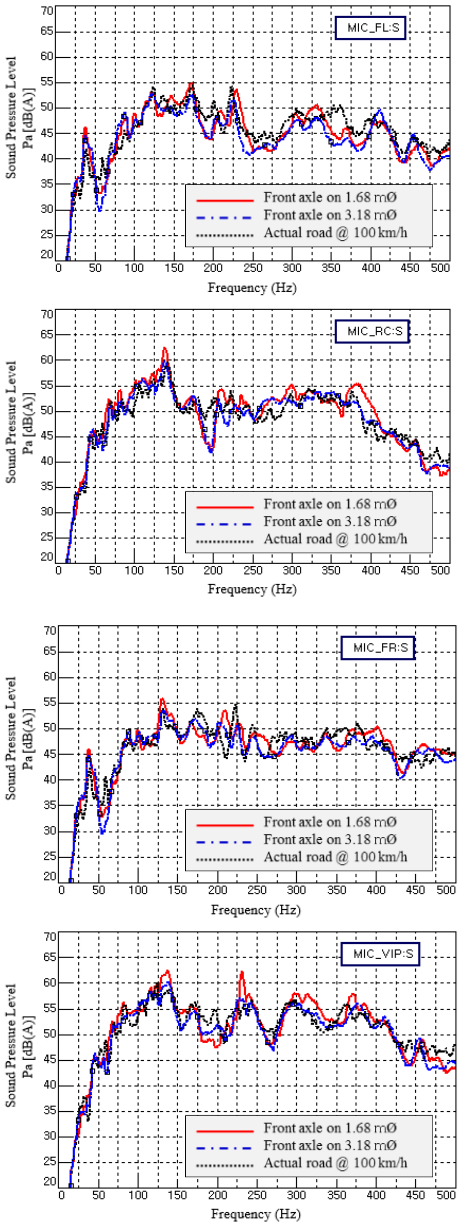

Figure 3.14 Cabin noise comparison (red solid line) 20-120 km/h runs up operation with front axle on 1.68 mØ (blue dash dotted line) 20-120 km/h runs up operation with front axle on 3.18 mØ. (black dotted line) 100 km/h constant speed actual road measured.

3.6 Knuckle signal comparison between proving ground excitation and dyno excitation

The primary purpose of using replicated detachable shell dyno excitation is that it can be utilized for the in-depth NVH investigation, such as refined ODS, empirical TPA, and test bench measured, as well as for actual road vehicle measured data comparison and synthesis. Thus, matching excitation between the dyno and actual measurement is crucial.

3.6.1 Rough and standard surface

Figures 3.15 and 3.16 show rough surface measured energy averaged knuckle acceleration signal comparison between the dyno excitation and the actual road excitation. For both front and rear knuckle, a very good match of the excitation level is in general achieved, considering that two signals are obtained under two different operational conditions (100 km/h constant speed operation for the actual road and 20 – 120 km/h run-up operation for the dyno excitation).

By comparing the signal obtained under two different operational conditions, one consideration has to be taken into account for tire cavity noise. Unlike other structural modes, the tire cavity resonance is caused by oscillating air column within the cavity

of the tire and its frequency splits and shifts with the change of its rotational speed. This is intuitively observed from figure 3.10 (splitting two tire cavity color lines between 200 Hz and 250 Hz as the vehicle velocity changes). Therefore, the tire cavity resonance seen in varying speed operation cannot be directly compared to that of the constant speed data. The exact frequency and amplitude of tire cavity resonance at particular speed can be drawn from the colormap or can be calculated using Eq. (3.7).

$$f = c \pm v/\overline{U}. \tag{3.7}$$

where f is the tire cavity resonance frequency, $\overline{U}$ is the mean circumference of outer and inner tire, c is speed of sound at warmed up tire temperature, and v is the speed of the vehicle. Similarly, a very good match was achieved for standard surface measured energy averaged front knuckle acceleration signal (see Figure 3.17). However, the rear knuckle energy spectrum shown in Figure 3.18 was measured on the smaller roller and 350 Hz above frequency were seem to be exaggerated as compared to that of the actual road measurement.

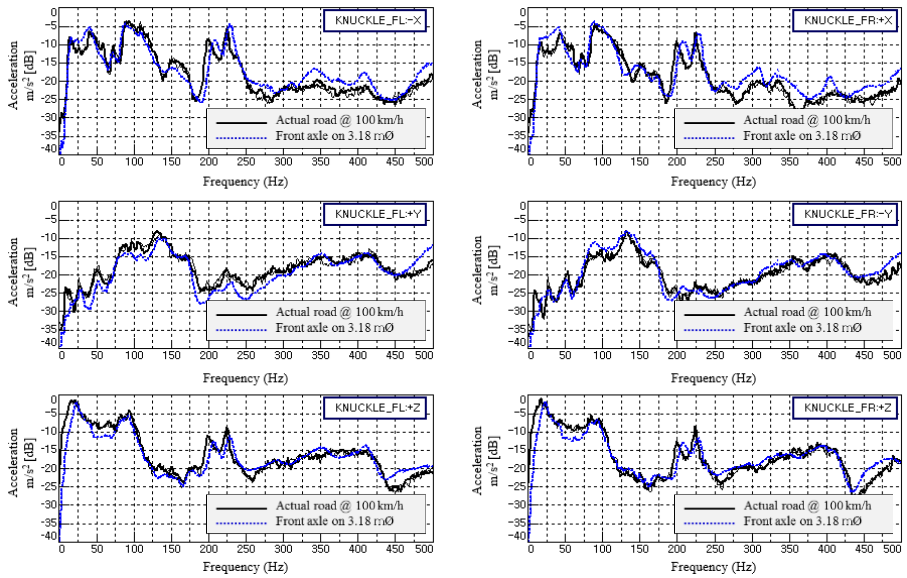

Figure 3.15 (blue dotted line) 20-120 km/h dyno excited (front axle on 3.18 mØ roller) to (black solid line) 100 km/h constant speed actual road excited front knuckle signal comparison on rough surface.

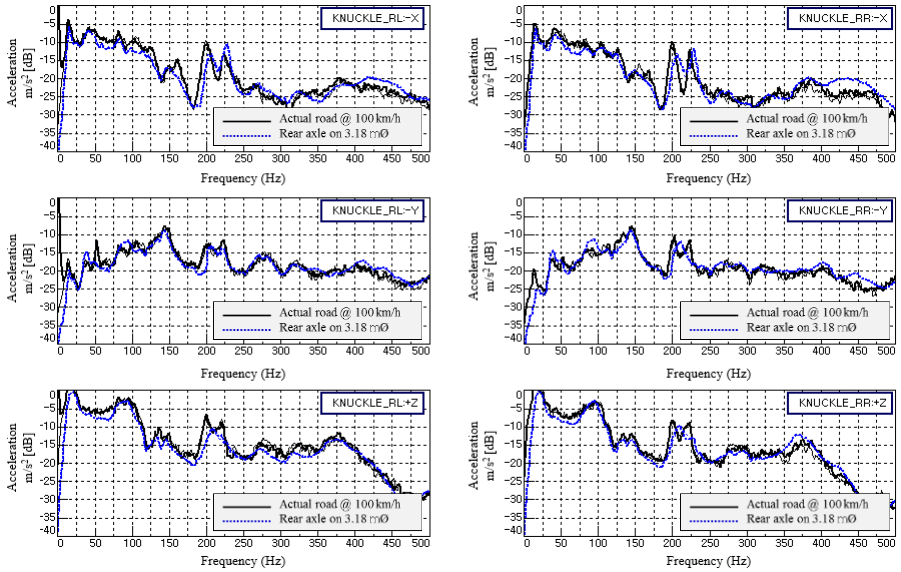

Figure 3.16 (blue dotted line) 20-120 km/h dyno excited (rear axle on 3.18 mØ roller) to (black solid line) 100 km/h constant speed actual road excited rear knuckle signal comparison on rough surface.

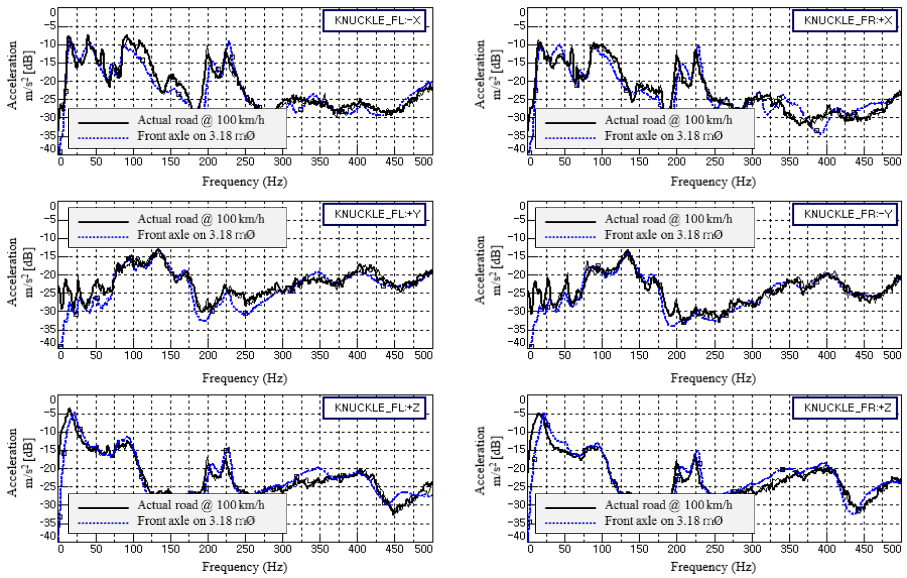

Figure 3.17 (blue dotted line) 20-120 km/h dyno excited (front axle on 3.18 mØ roller) to (black solid line) 100 km/h constant speed actual road excited front knuckle signal comparison on standard surface.

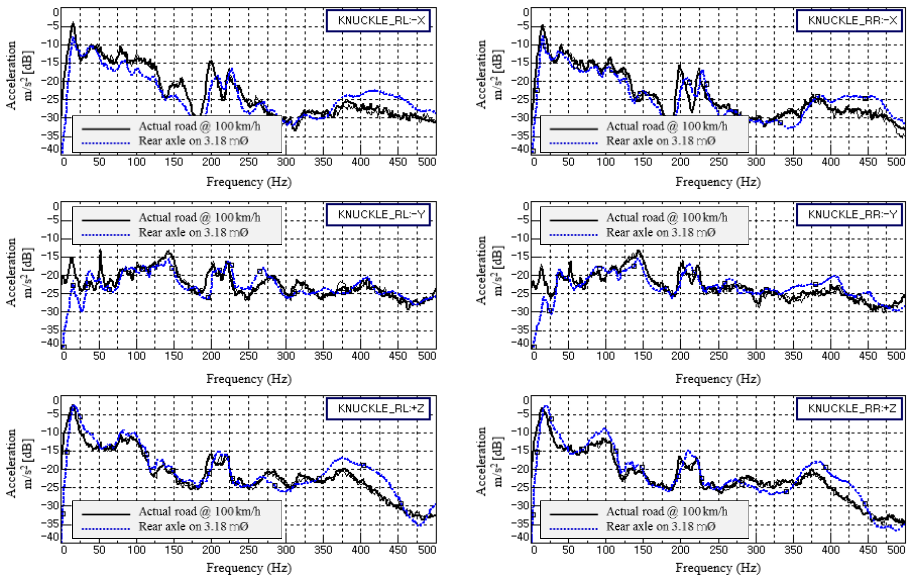

Figure 3.18 (blue dotted line) 20-120 km/h dyno excited (rear axle on 1.68 mØ roller) to (black solid line) 100 km/h constant speed actual road excited rear knuckle signal comparison on standard surface.

3.6.2 Smooth surface

Similarly to rough and standard surface results, a very good match between the actual road excitation and the dyno excitation is overall observed on smooth surface (see Figures 3.19 and 3.20. However, an unrealistic peak is observed on both front and rear knuckles in longitudinal and vertical directions in-between 50 to 100 Hz as high as up to 10 dB from the dyno excited measurement.

Since most of excitation is due to its tire and wheel on smooth surface, rather than the interaction with the profile of the shell (as compared to the rough surface

excitation), these data lose their validity and cannot be accepted as the vehicle's characteristics. Thus, the color map was plotted for vertical direction knuckle signal (see Figure 3.21) for further detail analysis. From this figure, a clear over-exaggerated order is observed as the vehicle's speed increases.

After tracking the colormap with both tire and dyno, it was clear that this unrealistic order component was due to the dyno's 32^{nd} order. The root cause for this exaggerated 32^{nd} order was obvious, since total 16 shell plates were installed for the front roller and two bolts are screwed in the middle of each plate designed to hold the shell on to the roller for high-speed operation. This indicates that the previous consideration of 16^{th} order pertinent to 16 detachable plates can be neglected, since it does not influence the measurement; however, excitation due to the installation bolt became prominent as the smooth surface dose not generate much excitation.

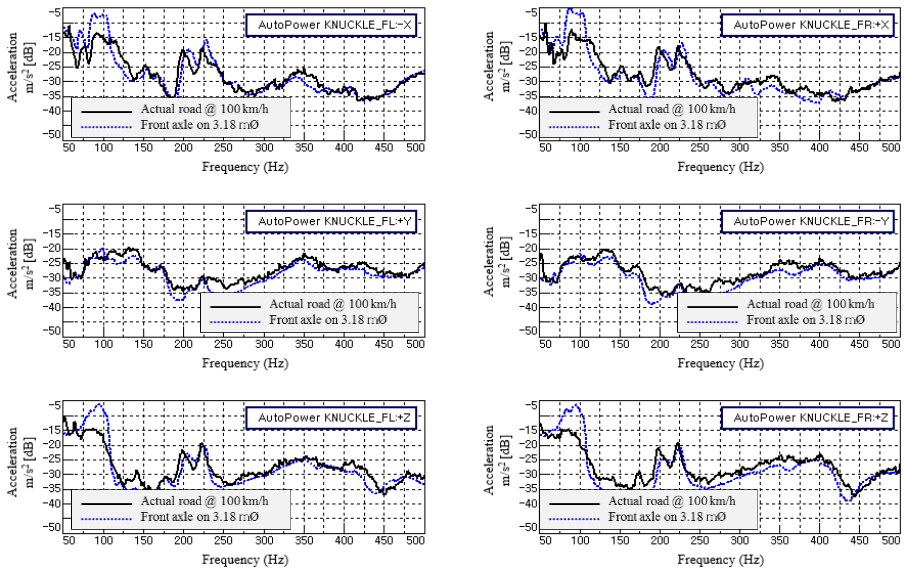

Figure 3.19 (blue dotted line) 20-120 km/h dyno excited (front axle on 3.18 mØ roller) to (black solid line) 100 km/h constant speed actual road excited front knuckle signal comparison on smooth surface.

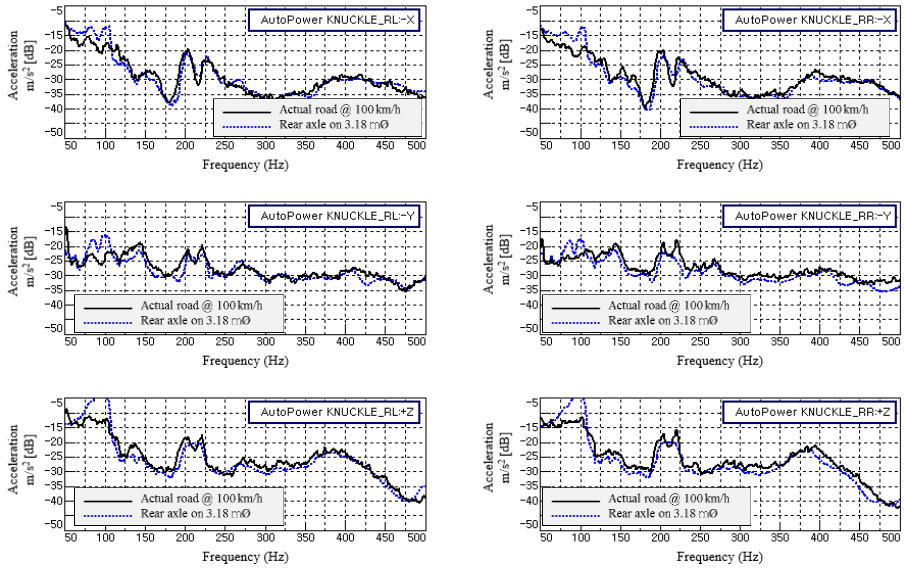

Figure 3.20 (blue dotted line) 20-120 km/h dyno excited (rear axle on 3.18 mØ roller) to (black solid line) 100 km/h constant speed actual road excited rear knuckle signal comparison on smooth surface.

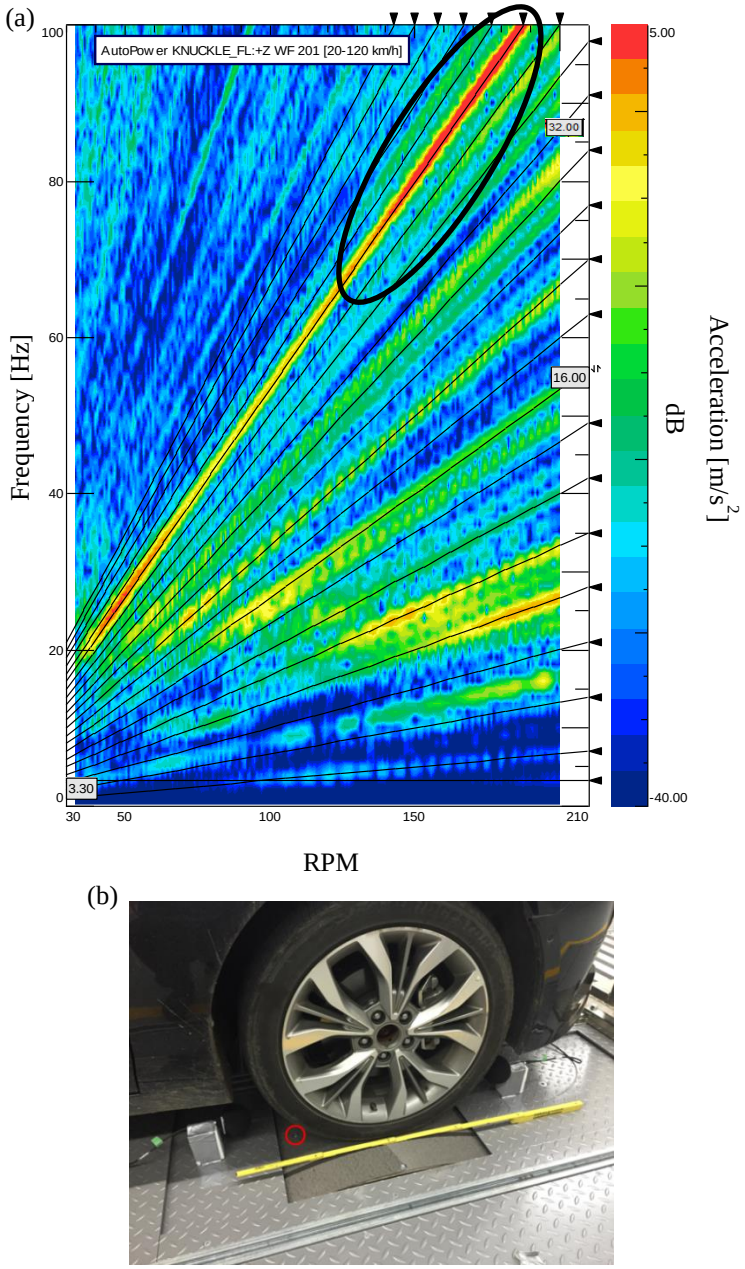

Figure 3.21 (a) Colormap (tracked with 3.18 mØ dyno rpm) plot of the front knuckle in vertical direction measured on smooth surface and (b) the root cause for over exaggerated 32nd order components.

3.7 Coherence study

ODS is one of most frequently used NVH tools which essentially displays the relative displacements in terms of amplitude and phase of responses with respect to reference signal to identify the system's dynamic behavior in actual operating condition. By using spectral transmissibility, ODS can be performed within a defined system (see Eq. (3.8)):

$$[\mathrm{T}(\omega)]_{i\times j} = \{\mathrm{X}(\omega)\}_i / \{\mathrm{X}(\omega)\}_j. \tag{3.8}$$

where $\mathrm{X}(\omega)_i$ indicates the response spectrum at *i,* $\mathrm{X}(\omega)_j$ indicates the reference spectrum at *j,* and, therefore, $[\mathrm{T}(\omega)]_{i\times j}$ represents the spectral transmissibility. In road noise application, due to its unfixed phase relation between each input, virtual reference signals are often generated in order to perform ODS. With the proposed replicated dyno shell excitation method, this problem is coped with having the excitation profile mirrored about the longitudinal axis. The coherence between the left and right wheel in vertical direction is calculated with H1 estimation method (see Figure 3.22). The coherence is compared among different roller sizes, when the vehicle is set on the dyno off centered, when not in-phase excitation (90 degree offset between left and right) is used, and measured on actual road.

Up to 300 Hz, overall 0.7, sufficient coherence between the left and right input signal is observed for both smaller and larger roller measurements. To observe how

much improvement can be achieved by using the proposed excitation method when a single reference is selected for road noise ODS processing, the actual road measured and the dyno measured acceleration at front sub frame and SPL at driver's ear were processed with the left and right knuckle vertical signal and compared (see Figure 3.23). For the actual road measured data, almost randomized phase and significantly deviated amplitude is observed. It is obvious that single knuckle spectrum is inappropriate to be selected as a phase reference for this case. On the other hand, two curves seem to be practically identical up to 400 Hz with the proposed in-phase excitation method.

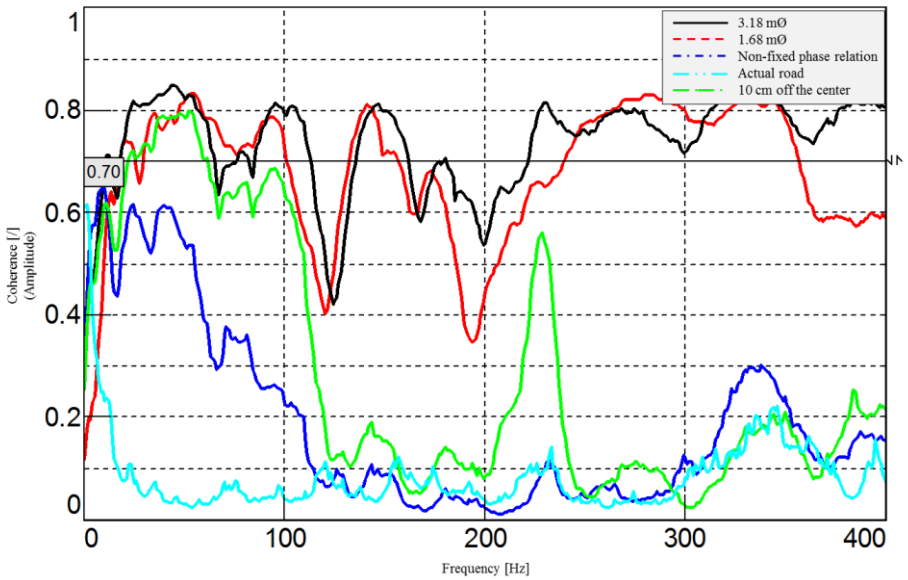

Figure 3.22 Coherence between rear left wheel and rear [illegible] vertical direction (black solid line) measured on larger roll[illegible]e) measured on smaller roller (blue dash dotted line) measured on non-fixed phase relation profile (turquoise dash double dotted line) measured on actual road (green double dash dotted line) measured on dyno but 10 cm shifted from the centerline.

3.18 mØ
1.68 mØ
Non-fixed phase relation
Actual road
10 cm off the center

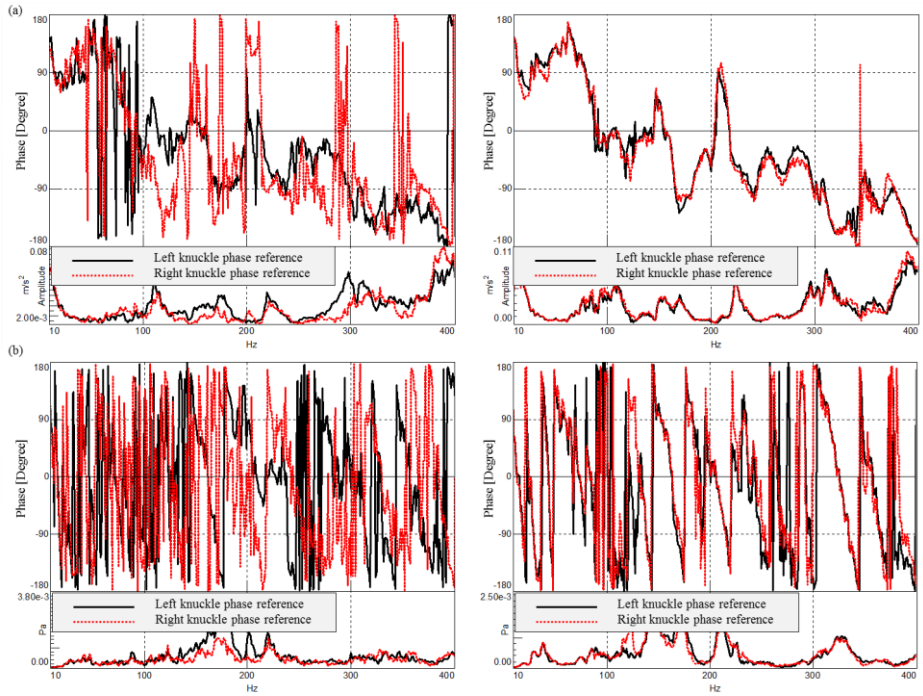

Figure 3.23 (a) Actual road excited (left) and proposed dyno excited (right) sub-frame cradle signal comparison. (b) Actual road excited (left) and proposed dyno excited (right) Driver's ear SPL comparison. (black solid line) Vertical direction left knuckle spectrum phase referenced, (red dotted line) vertical direction right knuckle spectrum phase referenced.

3.8 Road noise evaluation examples using proposed dyno. Excitation: detachable TPA approach and direct force rig approach

Figure 3.24 depicts an application example of detachable TPA that empirically identifies structure-borne road noise path contributors. By physically detaching parts that is suspected to road noise contributor, its contribution effect can be accurately investigated by checking the improvement achieved by its detachment of the vehicle.

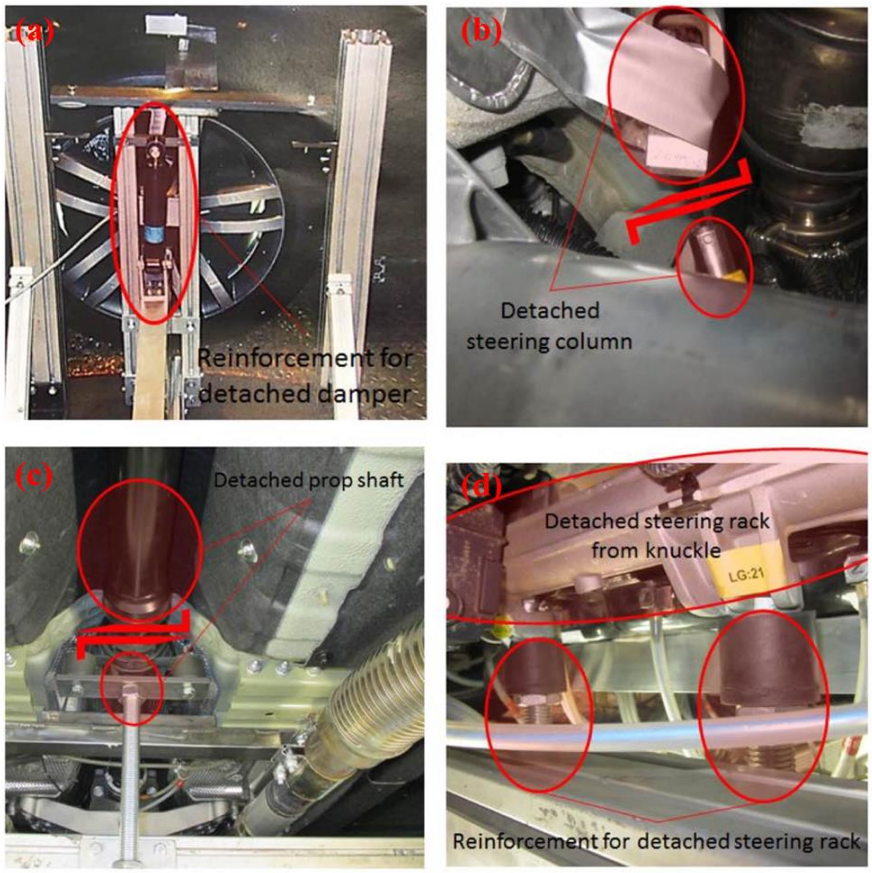

Figure 3.24 Empirical road noise evaluation using the detachable TPA method using replicated detachable shell excitation. (a) Detached front damper; (b) detached steering column; (c) detached prop shaft; (d) detached steering rack

3.9 Summary

In this chapter, the precision CNC-milled road surface dyno excitation method is validated up to 500 Hz through a comparative study with actual road excitation. In addition, a coherence study has been included, as one of its intended purposes includes circumventing typical multiple coherent input problem for road noise TPA and ODS. The following conclusions can be drawn from the results:

1) An excellent reproducibility is achieved for all measurements with the proposed detachable road shell dyno excitation method in combination with the one-point fixing device.
2) Constant speed operation on dyno with the proposed excitation method creates rippled signal due to the repeated excitation of revolution of the roller. Run up/run down operation has to be carried out in order to alleviate this phenomenon.
3) Hence, constant speed actual road measurement is compared with run-up/rundown on dyno and a significantly good match between 100 km/h actual road excitation and 20-120 km/h run-up dyno excitation is observed.
4) For smooth surface dyno excitation, 32^{nd} dyno order dominants the excitation characteristics causing overestimation around 80 to 100 Hz.

This is due to the effect of the plate bolts (2 bolts per plate and total 16 plates, which is designed to be flushed with the surface) that becomes prominent as the excitation from smooth surface is low. Yet, an excellent match is observed from 100 – 500 Hz.

5) When the rear axle is set on the smaller roller (1.68 mØ), it tends to overestimate lateral and vertical knuckle acceleration as high as up to 4 dB within 300 to 400 Hz band compared to that of the larger dyno roller (3.18 mØ).

6) Up to 400 Hz, 0.7coherence is achieved between the left and right wheel with the proposed excitation method, when the vehicle is set exactly at the center of the road profile shell for both smaller and larger rollers.

7) To investigate how much influence it can have on the ODS analysis, the sub- frame acceleration is processed with the left and right knuckles as a phase reference and compared. A nearly identical spectrum is obtained when the proposed dyno excitation method is used.

CHAPTER 4

ESTIMATION OF BODY INPUT FORCE TRANSMISSION CHANGE DUE TO PARTS' MODIFICATION USING THE IMPEDANCE METHOD UNDER ROLLING EXCITATION

4.1 Introduction

One of the most ubiquitously performed strategies to improve the structure-borne road noise is optimizing the dynamic properties of bushing at a dominant acoustic energy transfer path, as two thirds of the road noise are conquered by suspension to the body input operational forces. To closely attend to the problem of improving the operational force, Song et al. developed a suspension rig for practically obtaining the direct force at hard points, neglecting the vehicle's body and hence solely assessing a suspension's vibro-acoustic performance.

The principal concept for the rig is that a chassis system is mounted on a heavy structure settled on a relatively soft riding-height adjustable spring air bellow, so that the road induced operational force flows towards the rig, hence

neglecting the vehicle body's influence under the actual operational condition. This is achieved by maximizing the impedance of the attachment points for preventing the local deformation effect and isolating transmitted force at the passive (rig) side. Separating the effect of the vehicle body from the chassis system is definitely an advantageous method for optimizing suspension's vibro acoustic performance (*e.g.* through benchmarking testing with a better performing system). However, further investigation of the influence that the vehicle body attachment point has on the use of the suspension rig method is, as suggested by Kim et al., is still necessary. This suggests that potentially misleading results can be drawn for improving chassis NVH performance when countermeasures are drawn based on the rig testing method. In other words, the improvement achieved from the rig measurement might not be achieved when performed in the actual vehicle testing.

Consequently, to investigate the potential problem mentioned above, in the present study, a suspension coupled to a vehicle body via an elastomer is modeled using the impedance method. Generally, the term impedance is used to describe the relationship between the current and voltage within an electrical circuit, though, in a mechanical system modeling, the definition of the impedance is stretched to be represented by using the frequency response function-based relationship. Each element, which makes up the whole

mechanical system when rigidly coupled, is in this regard represented by the input over output. As compared to many other modeling methods, the usage of this modeling method has several advantages in terms of tackling aforementioned problem.

Typically, the finite element modeling technique cannot guarantee the accuracy up to the interest frequency of road-induced noise; neither the statistical energy analysis method, nor the asymptotic modal analysis method is suitable for accurately predicting the dynamic behavior under scoped frequency range. Otte has proposed the dynamic compliance based sub-structuring method which uses measured FRF of each sub-structure from free-free condition to calculate coupled system's responses. Furthermore, Jiantie, Lim, and Lu have provided the inverse formulation method to calculate the connecting stiffness properties between two sub-structures based on measured transfer functions from the total structure and validated the results by both single and multi-coordinate coupling cases. However, the accuracy of these studies has only been validated within a simple or theoretical applications and lacks in practicality when applied to real-world automotive NVH problems (*e.g.* road noise).

The impedance modeling used in this chapter uses measured mechanical impedance (or dynamic stiffness) value which can be obtained within an

assembled system, since the modeling assumes each element is represented by its point impedance and is connected via a simple linear formation. Henceforth, changing one element does not alter the impedance of other elements, which is not the case for the dynamic compliance based sub-structuring method. Using the impedance modeling method, a numerical study is performed to investigate achievable force reduction due to bush optimization under different systems with different properties of the impedance combination. Following the numerical study, the proposed impedance coupling model is validated for actual road excitation application by comparing the estimated and measured force changes between two different suspensions for two different locations: McPherson strut type suspensions in lateral arm Y direction and Multilink type rear suspension in front mount X direction which represent the extremely stiff and the extremely soft coupling cases within typical passenger vehicle suspension, respectively.

4.2 Transmission force characterization and estimation of changing force due to parts' modification using the impedance modeling method

Figure 4.1 (a) shows a simplified coupling of a suspension link to the vehicle body via an elastomer bush under road induced excitation. Each element (link, bush, and body) from the scheme is represented with its point impedance, $Z(\omega)$, which, in this study, adopts input/output driving point transfer function as the definition where the input is in force $F(\omega)$ and the response is in velocity $v(\omega)$, to convert into Thévenin's equivalent circuit as shown in Figure 4.2 (b). From the definition of mechanical impedance of a point on a structure, the ratio of the force applied to the resulting velocity at that point, force exerted to the body and the force exerted to the internal (chassis) are expressed as follows (see Eq. (4.1)-(4.2)):

$$F_{body} = Z_{body} * v_{body} \tag{4.1}$$

$$F_{internal} = Z_{internal} * v_{internal}. \tag{4.2}$$

If all the elements are rigidly connected, the equilibrium of force and continuity of motion holds true for coupling as follows (see Eq. (4.3)):

$$F_{chassis} = F_{internal} + F_{body} \tag{4.3}$$

$$v_{internal} = v_{body}. \tag{4.4}$$

Substituting Eq. (4.1) and (4.2) into Eq. (4.3), the total force $F_{chassis}$ is defined as follows (see Eq. (4.5)):

$$F_{chassis} = Z_{internal} * v_{internal} + Z_{body} * v_{body}. \quad (4.5)$$

Applying the continuity of motion in Eq. (4.4) into Eq. (4.5) and solving for v_{body} gives Eq. (4.6).

$$v_{body} = \frac{F_{chassis}}{Z_{\text{internal}} + Z_{body}}. \quad (4.6)$$

Substituting the v_{body} back into Eq. (4.1), the force transmitted to the body is represented with the impedance combination of the system multiplied with the Thévenin source, $F_{chassis}$ (see Eq. (4.7))

$$F_{body} = \frac{Z_{body}}{Z_{\text{internal}} + Z_{body}} * F_{chassis}. \quad (4.7)$$

Bringing the force terms to the left side of the equation rewriting the internal impedance in terms of link and bush separately, the excitation transmission characterization is defined as follows (see Eq. (4.8)):

$$ETC = \frac{Z_{body}}{\frac{1}{\frac{1}{Z_{link}}+\frac{1}{Z_{bush}}} + Z_{body}} \quad (4.8)$$

where, as shown in Eq. (4.9)

$$Z_{internal} = \frac{1}{\frac{1}{Z_{link}} + \frac{1}{Z_{bush}}}. \quad (4.9)$$

The ETC represents the characteristics of how excitation is transmitted from active side to passive side as the ratio of the Thévenin source input force to the

transmitted force to the body. From Eq. (4.8), it can be seen that the impedance of the link and bush is inversely proportional to the excitation transmission characteristics. That is, as the impedance of link and bush gets smaller, a higher force transmission is achievable from the source (active) to the receiver (passive) point. To observe how the maximum ETC value is achieved, the impedance of the body is set to extremely large in comparison to that of the chassis. That is, if, as shown in Eq. (4.10),

$$\mathrm{Z}_{body} \gg \mathrm{Z}_{chassis} \tag{4.10}$$

(For simplicity purpose, from here on, the term $\mathrm{Z}_{chassis}$ is substituted for $\mathrm{Z}_{internal}$) then, as shown in Eq. (4.11),

$$\mathrm{ETC}_{max} \approx 1. \tag{4.11}$$

This can be interpreted that, if the impedance of the body is relatively large in as compared to the impedance of chassis (combination of link and bush), the transmitted force at the response point ideally reduces with the reduced input chassis force.

Likewise, the suspension system attached to a body is modeled using the Norton's equivalent system (see Figure 4.2) to relate the resulting body force to a velocity term (as the velocity can easily be measured using the accelerometer within the system, even for complex system like a suspension). The resulting

force F_{body} is expressed using the impedance combination of elements multiplied to the v_{free} (see Eq. (4.12)):

$$F_{body} = \frac{Z_{chassis} * Z_{body}}{Z_{chassis} + Z_{body}} * v_{free}. \quad (4.12)$$

Ideally, the free velocity v_{free} is the velocity of the source due to the road excitation where the source is detached from other elements within the system. However, within the actual suspension testing, this is challenging to obtain, since one of the most important roles of the suspension is to make the wheel remain in contact with the road; therefore, disconnecting the suspension element will affect the total behavior of the system. For this purpose, the link's velocity (active side) is used to reversely estimate the free velocity using the following linear relationship (see Eq. (4.13)):

$$v_{free} = \frac{Z_{link} + \frac{Z_{bush} * Z_{body}}{Z_{bush} + Z_{body}}}{Z_{link}} * v_{link}. \quad (4.13)$$

Substituting Eq. (4.13) into Eq. (4.12), the force transmitted to the body is calculated as follows (see Eq. (4.14)):

$$F_{body} = \frac{Z_{chassis} * Z_{body}}{Z_{chassis} + Z_{body}} * \frac{Z_{link} + \frac{Z_{bush} * Z_{body}}{Z_{bush} + Z_{body}}}{Z_{link}} * v_{link}. \quad (4.14)$$

Then, the force change (reduction force) due to parts modification from the original (system 1) to the modified (system 2) is solved in dB scale (see Eq. (4.15)).

$$
\begin{aligned}
\mathrm{F}_{body\_reduction} = 20 * \log[\\
\{\mathrm{Z}_{chassis,1} * \mathrm{Z}_{body,1}\left(\mathrm{Z}_{chassis,2} + \mathrm{Z}_{body,2}\right) \\
* \frac{\mathrm{Z}_{link,1} + \frac{\mathrm{Z}_{bush,1} * \mathrm{Z}_{body,1}}{\mathrm{Z}_{bush,1} + \mathrm{Z}_{body,1}}}{\mathrm{Z}_{link,1}} * \mathrm{v}_{link,1}\}/ \\
\{\mathrm{Z}_{chassis,2} * \mathrm{Z}_{body,2}\left(\mathrm{Z}_{chassis,1} + \mathrm{Z}_{body,1}\right) \\
* \frac{\mathrm{Z}_{link,2} + \frac{\mathrm{Z}_{bush,2} * \mathrm{Z}_{body,2}}{\mathrm{Z}_{bush,2} + \mathrm{Z}_{body,2}}}{\mathrm{Z}_{link,2}} * \mathrm{v}_{link,2}\}]
\end{aligned}
\tag{4.15}
$$

However, for practical usage of Eq. (4.14), to estimate the force change without actually having the parts change within the system, it is essential to acquire v_{free} that is not driven from Eq. (4.13), because v_{link} is the value that is strongly influenced by modified or substituted parts (e.g. bush substitution). In this regard, measureable velocity that can represent the free velocity expressing the pure road input that is not highly affected by suspension parts modification is required: knuckle's velocity is the only suitable option. Thereupon, by setting the following (see Eq. (4.16)):

$$
\mathrm{v}_{knuckle} = \mathrm{v}_{free}, \tag{4.16}
$$

And, under the identical excitation for system 1 and system 2, the following assumption is drawn (see Eq. (4.17)):

$$
\mathrm{v}_{free,1} \approx \mathrm{v}_{free,2}. \tag{4.17}
$$

Applying Eq. (4.16) into Eq. (4.12), the $F_{body\_reduction}$ can be estimated solely in terms of the impedance combination of link, bush, and body (see Eq. (4.18)).

$$F_{body_{reduction}} = 20 * \log[\{Z_{chassis,1} * Z_{body,1}(Z_{chassis,2} + Z_{body,2})\}/ \{Z_{chassis,2} * Z_{body,2}(Z_{chassis,1} + Z_{body,1})\}] \quad (4.18)$$

Higher the similarity between the two systems' knuckle signal means the higher the validity of assumption (Eq.4.17) hence, increases practicality of estimating force change utilizing proposed method.

Similarly to$F_{body_reduction}$, the velocity change at the active side due to parts' modification can be solved by the following (see Eq. (4.19)):

$$v_{link_{reduction}} = 20 * \log[Z_{link,1} * \left\{ Z_{link,2} + \left(\frac{Z_{bush,2} * Z_{body,2}}{Z_{bush,2} + Z_{body,2}} \right) \right\} / Z_{link,2} * \left\{ Z_{link,1} + \left(\frac{Z_{bush,1} * Z_{body,1}}{Z_{bush,1} + Z_{body,1}} \right) \right\}] \quad (4.19)$$

Direct force pick-up at a chassis to the body coupling location within the actual vehicle is difficult; therefore, the results calculated using Eq. (4.19) are used for a comparison with the measured value for checking its utilization validity.

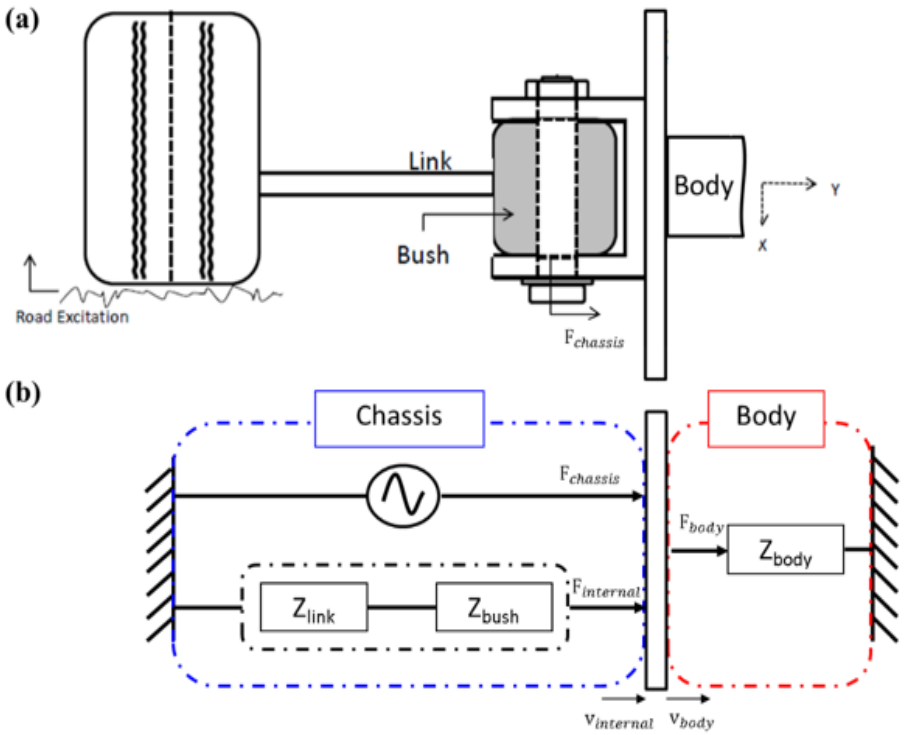

Figure 4.1 (a) Schematic representation of the simplified suspension to body coupling model; (b) Thévenin's equivalent system for the model

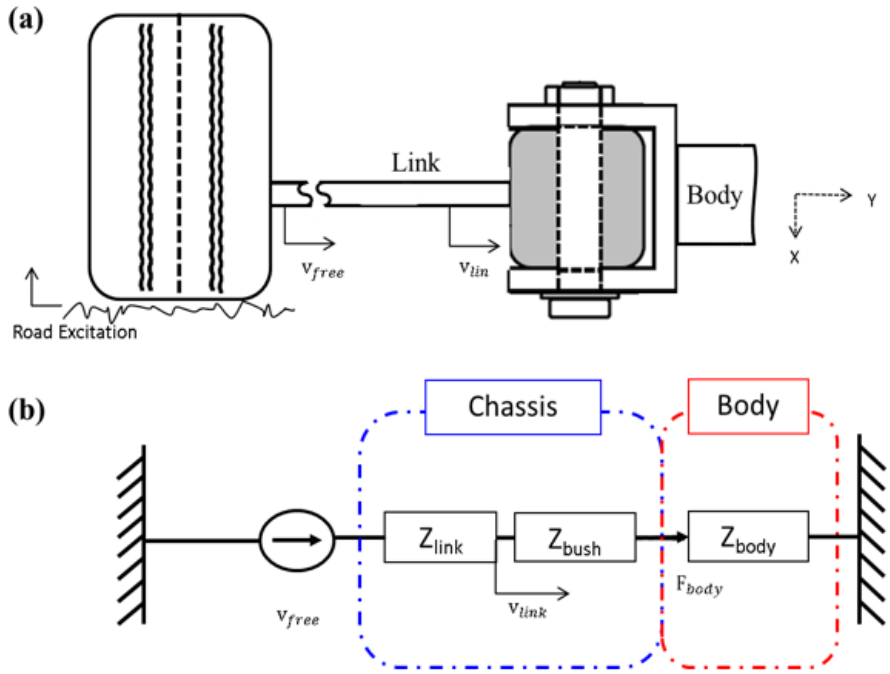

Figure 4.2 (a) Schematic representation of the simplified suspension to body coupling model; (b) Norton's equivalent system for the model

4.3 Numerical study: force change (reduction) estimation due to part modification

Prior to the actual road excitation validation, a numerical study has been performed to get the idea how the force transmission changes with different impedance combinations of suspension parts. All impedance values are substituted with the driving point dynamic stiffness, since the vehicle bush's property is frequently expressed in dynamic stiffness within the automotive

NVH engineering field. Simple substitution is allowed, as both the driving point impedance and dynamic stiffness are transfer functions that characterize the mechanical system, but in different quantities: velocity over force and displacement over force.

As shown in Eq. (4.15), the force reduction is defined as a function of impedance combination of link, bush, and body altogether. In this regard, the numerical cases are separately carried for two different cases: first, to investigate how reducing the bush's stiffness by 50 % differently influences reducing forces within different dynamic stiffness combinations of a system. Second, to investigate how the body stiffness differences (from 80000 N/mm to 20000 N/mm to represent the stiff rig and soft vehicle body) potentially influence the directly picked-up force within different dynamic stiffness combination of a system. The values used for this numerical study are chosen considering the realistic actual passenger vehicle applications from extra soft to extremely stiff dynamic stiffness within the frequency range of interest for road induced excitation.

4.3.1 Softening the dynamic stiffness of the connecting bush by 50%

Nowadays, a passenger vehicle uses many different types of suspension depending on its size, price, segment, and so on. These suspensions are developed to serve their primary roles of isolating the vibro-acoustical energy transmission to the body and maximizing the handling and ride quality by means of structural and elastomer bush optimization. As the vehicle development phase gets into design freezes, the most feasible fine tuning method to improve the road noise is achieved through softening the suspension to the body connecting elastomer bushing. For this purpose, in this part, we will investigate how much of force reducing is achievable due to 50 % softened bush within a suspension with varying link and body's stiffness. The estimated reduction force results are plotted in Figure 4.3.

From top to bottom, the plotted results depict estimated force reduction for varying link's stiffness set at 20000 N/mm, 40000 N/mm, 80000 N/mm, and 160000 N/mm. Theoretically, using the Hook's law relation, maximum reduction of 6 N (dB) is expected by softening the bush by 50 %. However, the results show that this is only achieved for certain cases (i.e. the maximum body's and link's stiffness connected via extremely soft bush). Specifically,

with high body's stiffness, a yet higher force reduction is achieved when the connecting bush is extremely soft and the force reduction approaches the ideal force reduction even for soft body. On the other hand, when the connecting bush is set to be extremely stiff (i.e. $Z_{bush} = 20000\ \mathrm{N/mm}$), the achievable force reduction steeply falls down for soft body. Even with the same percentage of bush's stiffness reduction, achievable reduction force is different for different combinations and it appears that the connecting bush's original stiffness plays a decisive role. Therefore, a relatively soft link and a soft body system coupled via a relatively stiff bush makes it the most difficult transfer path to reduce the transmission force (i.e. only 2.5 N (dB) reduction achieved when $Z_{link,1} = Z_{body,1} = Z_{bush,1} = 20000\ \mathrm{N/mm}$). These results suggest that, prior to tackling the most dominant transfer path, investigating achievable force reduction at each transfer path also needs to be considered.

In Figure 4.4, the calculated ETC is plotted for the exact same initial values (prior to 50% bush's stiffness reduction) used in Figure 4.4. It can be intuitively noticed that the trends of the curves are in accordance with the numerical study results plotted in Figure 4.3. As previously seen in Eq. (4.7), the maximum ETC is equal to 1, which indicates the response force reduces ideally with reduced input force. The ETC value maximizes with an increase of the stiffness of the body and as the link and bush gets softer. This result indicates that the

impedance modeling-base calculated ETC value allows for a rough forecast of achievable force reduction without actually having the parts modified.

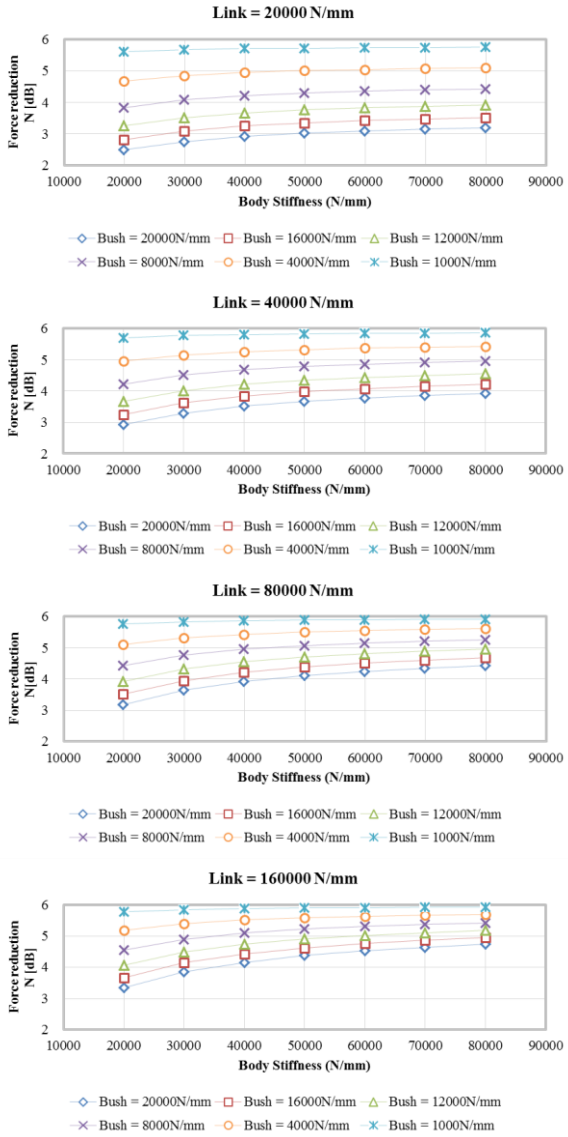

Figure 4.3 Estimated force reduction due to bush's stiffness reduction by 50% for different dynamic stiffness combinations: (a) $Z_{link,1}$ = 20000 N/mm; (b) $Z_{link,1}$ = 40000 N/mm; (c) $Z_{link,1}$ = 80000 N/mm (d) $Z_{link,1}$ = 160000 N/mm

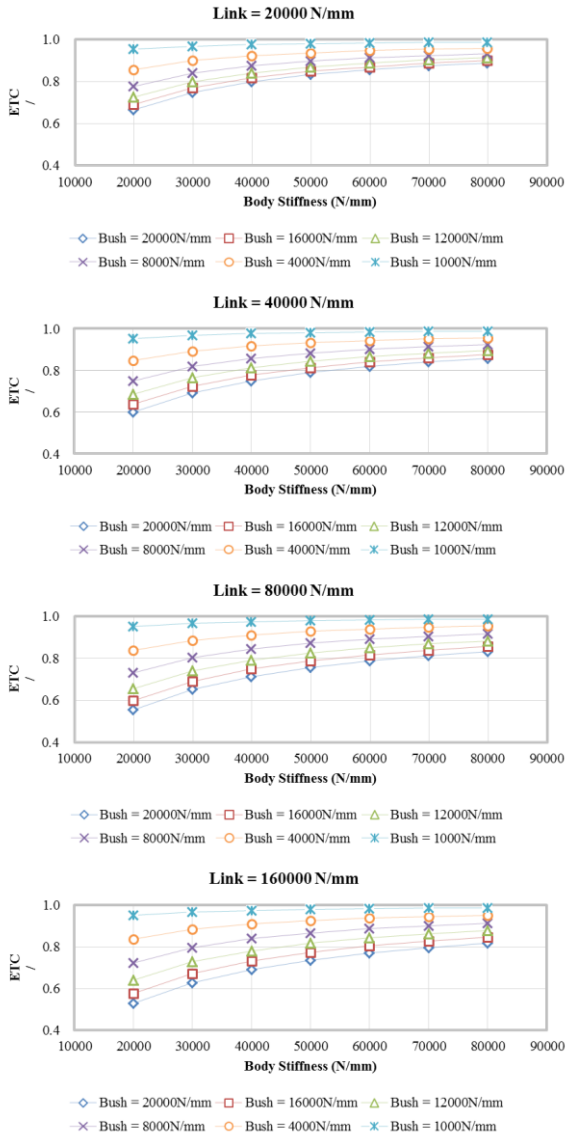

Figure 4.4 Excitation transmission characterization for the system with different dynamic stiffness combinations: (a) $Z_{link,1}$ = 20000 N/mm (b) $Z_{link,1}$ = 40000 N/mm; (c) $Z_{link,1}$ = 80000 N/mm; (d) $Z_{link,1}$ = 160000 N/mm

4.3.2 Studying the relation of the suspension rig to vehicle: reducing the stiffness of the body attachment point

One of the primary purposes of modeling a suspension system using the impedance method is to predict the potential misleading force reduction obtained from the suspension rig to the actual vehicle due to a considerable stiffness difference on the passive side of their attachment point. Since the development objective of the previously developed suspension rig includes early stage suspension's component change testing, it is important to learn whether the optimization made on suspension under rig testing is valid when it is moved to the actual vehicle body. In this regard, the initial body's stiffness is set at 80000 N/mm to represent the rigid suspension rig's attachment point and reduced to 20000 N/mm to represent a soft attachment point on the actual passenger vehicle's body. The numerical study results and ETC plots for rig to actual vehicle relation study are shown on Figures 4.5 and 4.6, respectively.

The results show that the potential misleading deviation in force due to body stiffness differences is up to ca. 4 dB with the link's stiffness set to 160000 N/mm and bush's stiffness set to 20000 N/mm. Accordingly, its pertinent excitation transmission characterization value drops down to ca. 0.8. By contrast, when the link and bush's stiffness values are set to be the lowest,

almost no misleading force reduction is observed between the rig and the actual vehicle. Another observation point is that the deviation is strongly influenced by stiff bush connection, whereas almost no deviation in reduction force is observed for soft bush connection cases, even when the link's stiffness increases 8th-fold from 20000 N/mm. Therefore, the ETC value reaches the maximum when the bush's stiffness is low and not much deviation is observed even with a different link's stiffness. However, this value steeply drops for stiff link cases and gradually falls for softer link cases with increasing stiffness of the connecting bush. Therefore, the maximum potential force deviation case is represented with the lowest ETC value.

This result suggests that as the link to body coupling bush gets stiffer, more the deviation in the reduction force is expected between the rig and the actual vehicle when the suspension's vibro-acoustic performance is optimized by means of softening the connecting bush. Said differently, force reduction achieved from the rig measurement by component modification may not result in identical reduction on the actual vehicle, even if the exact counter measure is performed for the case where the link to body is connected via a stiff bush. Besides, the fact that the force reduction is considerably more difficult to achieve for the stiff bush connection case as compared to the soft bush

connection (although both the link and body's stiffness was also an influential factor) implicates that extra consideration is needed to tackle these paths.

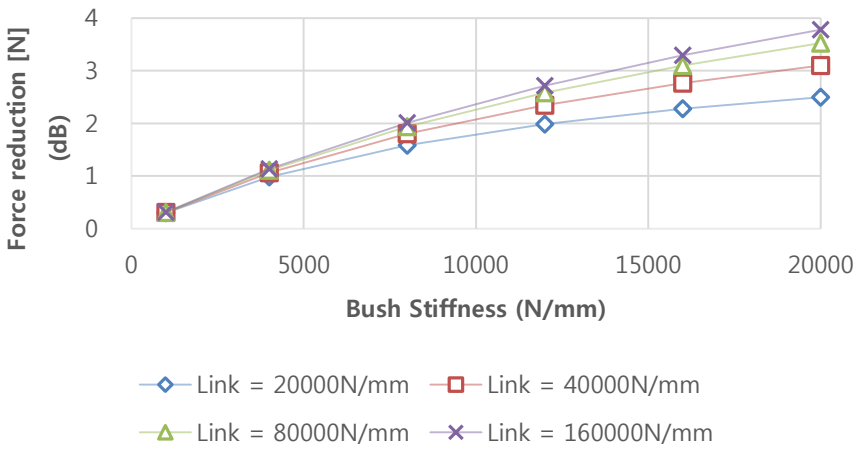

Figure 4.5 Potential force deviation between the rig ($Z_{body,1} = 80000\ \mathrm{N/mm}$) and the actual vehicle body ($Z_{body,2} = 20000\ \mathrm{N/mm}$) for different dynamic stiffness combinations of suspension link and bush

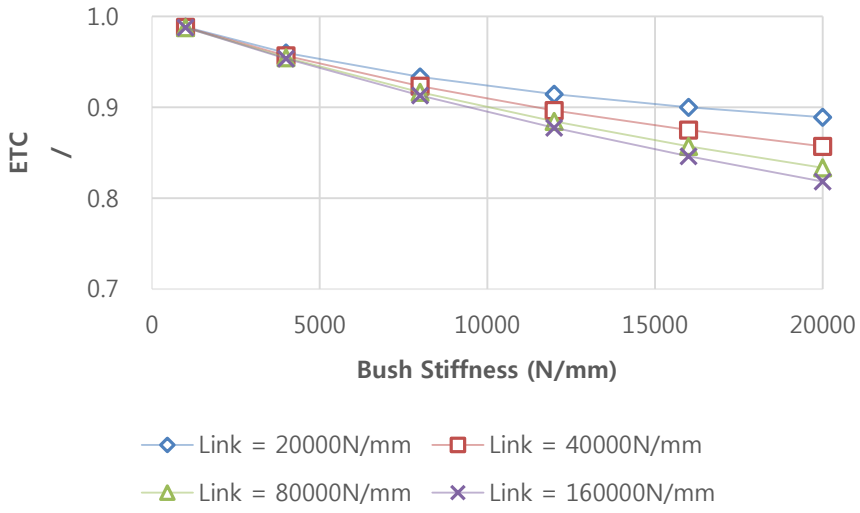

Figure 4.6 Excitation transmission characterization for rig ($Z_{body,1} = 80000\ \mathrm{N/mm}$) to the actual vehicle body ($Z_{body,2} = 20000\ \mathrm{N/mm}$) for different dynamic stiffness combinations of suspension link and bush

4.4 Validation for road excitation

4.4.1 Experimental setup

To further validate and use the impedance method and the developed suspension rig, an empirical test is performed under road excited application. Two different paths are chosen from two different manufacturer's suspensions for this experiment: (1) McPherson strut type front suspension's lateral arm in lateral direction (U1 Y-dir.), which is typically designed with a very stiff bush

amongst other vibro-acoustic transfer paths, as its primary role includes handling of a vehicle; (2) Multi-link type rear suspension's front mount in longitudinal direction (RAFM X-dir.), which is typically designed with a relatively soft bush for vehicle compliance and comfort.

4.4.1.1 Operational measurement

Road induced excitation is reproducibly generated using the gravel surfaced shell attached to a dyno roller (see Figure 4.7). To avoid repeated order effect caused from shell installed dyno excitation, operational speed is continuously increased from 20 km/h to 120 km/h with the ramp up rate of 1 km/h/s. Acquired data are processed with 1 Hz resolution tracked with 0.5 km/h increment so that 50 % averaging overlap is achieved, as it is the suggested optimal value for Hanning windowing for vibration analysis[16, 17]. For every measurement, the tire is warmed up to constant temperature by running the dyno at 15 km/h prior to the actual measurement. The suspension rig set up on the dyno for operational measurement is depicted in Figure 4.8.

Displacement spectra are derived from the measured acceleration (PCB 356A15 ICP sensor is used) by double integrating the signal. All spectra are processed with phase referenced with knuckle signal (Y-direction for U1 and X-direction RAFM). In this way, the least information of signal in that particular

direction is lost, but the phase information is preserved. Two PCB 260A02 ICP tri-axial force transducers are installed in the predefined location (see Figure 4.9) for direct force acquisition at the lateral arm and RAFM. In order not to lose bypass transmission through the bolt, two force signals from each location are added with the phase information. The bush's dynamic stiffness is derived from two accelerometers (one for passive and one for active) installed at the location where the force is picked (See Figure 4.9).

Figure 4.7 Road-mimicked gravel patch installed on the dyno roller for reproducible excitation

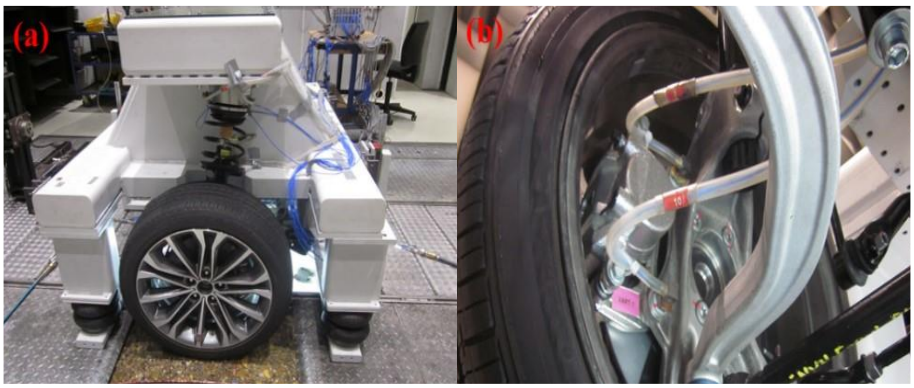

Figure 4.8 (a) Suspension rig operational measurement set up on dyno; (b) Knuckle input acceleration measurement point

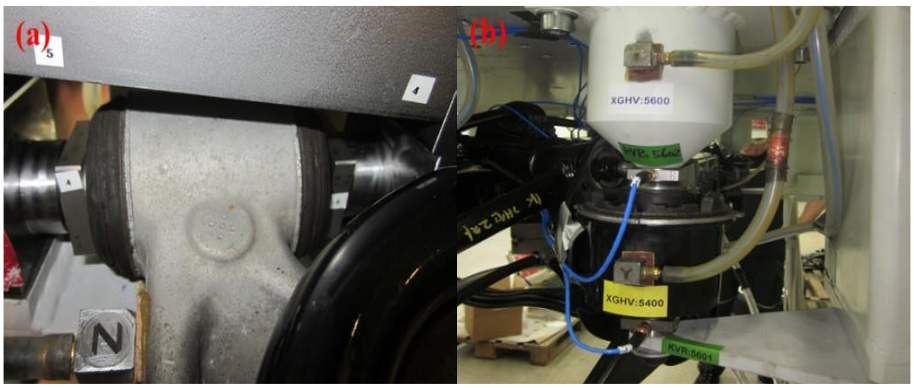

Figure 4.9 Direct force measurement points: (a) McPherson strut type suspension's lateral arm; (b) Multi-link rear suspension's front mount

4.4.1.2 Dynamic stiffness measurement for link and body

The driving point dynamic stiffness for the link and body is acquired using the conventional impact hammer measurement method. LMS Test.lab impact testing module, B&K 8206-002 impact hammer, and PCB 356A15 ICP accelerometers are used for signal acquisition. Force-exponential windowing and exponential decay windowing are applied for input hammer force and

response spectrum, respectively. The FRF measurement is performed using the H_v estimator, which is a built-in algorithm provided from LMS that uses total lease square or load to the response noise balancing method. The set-up is shown in Figure 4.10.

Obviously, the ideal boundary condition for impact measurement would be letting the system to remain identical as compared to the operational measurement. However, the measurement was performed on the lift due to complex structure of the suspension, which makes impact hammer experiment nearly impossible within the same boundary condition as the operational condition on the dyno. Nevertheless, striving to obtain the accurate estimation, the active side driving point dynamic stiffness value is averaged from three different nearby locations of each point, since this value is the essence in the calculation.

The passive sides' driving point dynamic stiffness is measured in a similar way (see Figures 4.10(b) and 4.01(d)). This process is performed in a straightforward manner for rear axle front mount, as the adapter block for its attachment point is robust and easy to be excited. For front axle's lateral arm on the other hand, suspension is removed and replaced with aluminum-mimicked block in order to carry out the measurement. A total of 5

accelerometers are installed and the averaged value is used as an input for this point.

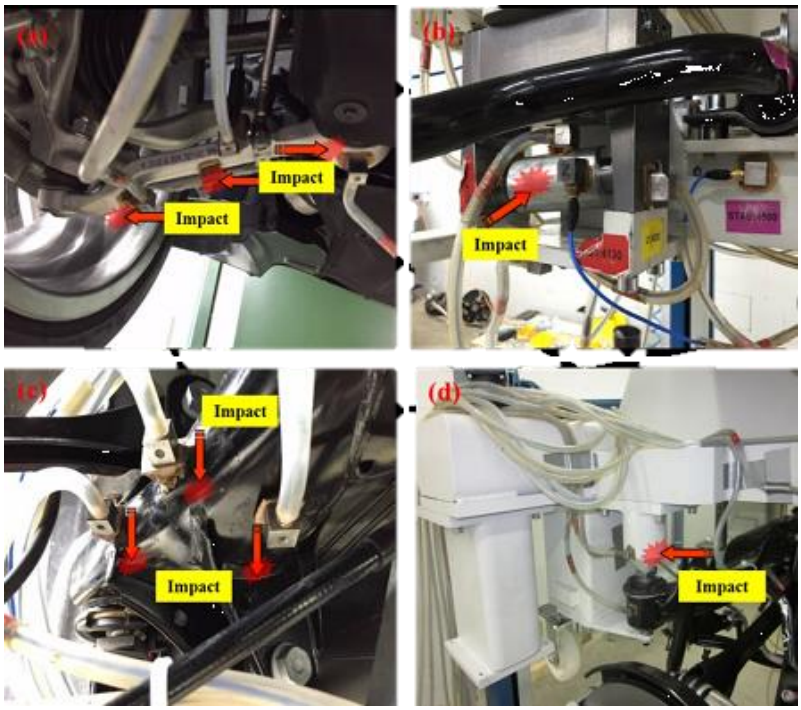

Figure 4.10 Dynamic stiffness measurement setup for (a) McPherson strut suspension lateral arm active side; (b) McPherson strut suspension lateral arm passive (body) side; (c) Multilink suspension front mount active side (d) Multilink suspension front mount passive (body) side

4.4.2 Obtained input values for force change estimation

In this section, inputs used for the validation are plotted. Figures 4.11 and 13 depict the measured and the calculated knuckle displacement derived from

the measured v_{link} signal; Figures 4.13 and 4.14 show the measured and calculated link displacement derived from the measured $v_{knuckle}$ signal. Although a slight deviation is observed between the measured and calculated at the suspension 1's front knuckle (see Figure 4.11(a)) within the 100 to 200 Hz range, in general, calculated values reasonably match with the measured values up to the frequency range of interest (300 Hz). Note that all spectra are obtained under 20 – 120 km/h dyno run-up operation and the reproducibility of the excitation is checked for each measurement.

Figures 4.15 and 4.16 show the plot of the obtained dynamic stiffness values for all three components at lateral arm in Y-direction and rear axle front mount in X-direction, respectively. It should be noted that, at the lateral arm, the stiffness of suspension 1's coupling bush is ca. 3 times higher than that of the suspension 2 and a ca. 2.5 times stiffer coupling bush is used for rear axle front mount for suspension 2 as to that of suspension 1. The body's stiffness is not much different, since the validation test was performed on the suspension rig (the deviation comes from the different design and material of the mounting blocks).

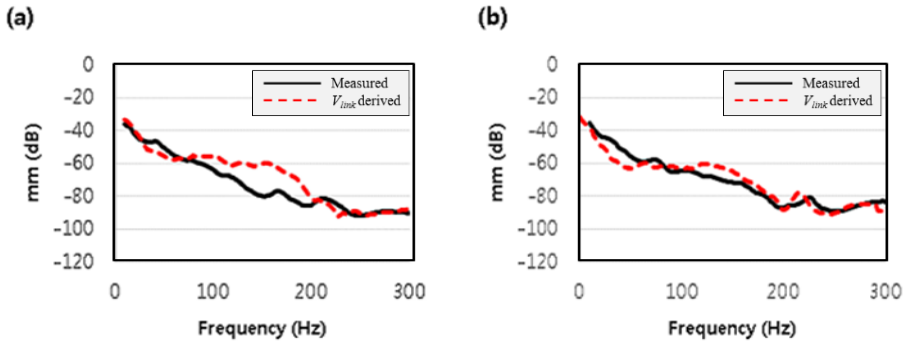

Figure 4.11 Measured (solid) and v_{link} derived (dotted) Y-dir. front knuckle displacement spectrum for (a) suspension 1 and (b) suspension 2

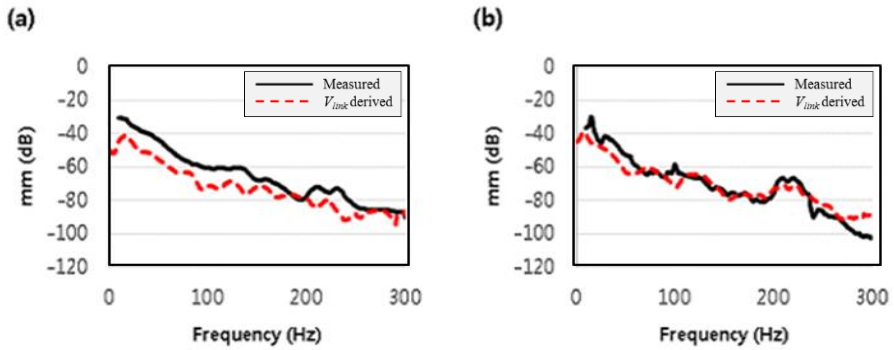

Figure 4.12 Measured (solid) and v_{link} derived (dotted) X-dir. Rear knuckle displacement spectrum for (a) suspension 1 and (b) suspension 2

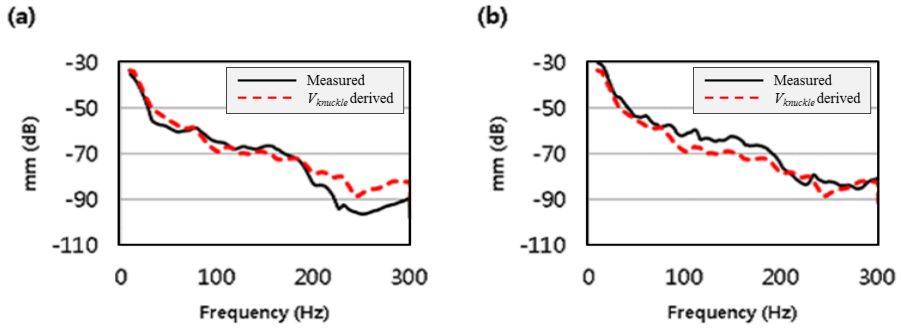

Figure 4.13 Measured (solid) and $v_{knuckle}$ derived (dotted) Y-dir. U1 displacement spectrum for (a) suspension 1 and (b) suspension 2

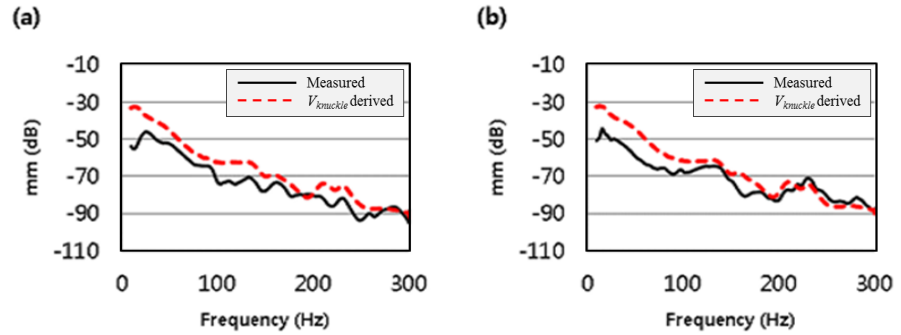

Figure 4.14 Measured (solid line) and $v_{knuckle}$ derived (dotted line) X-dir. RAFM displacement spectrum for (a) suspension 1 and (b) suspension 2

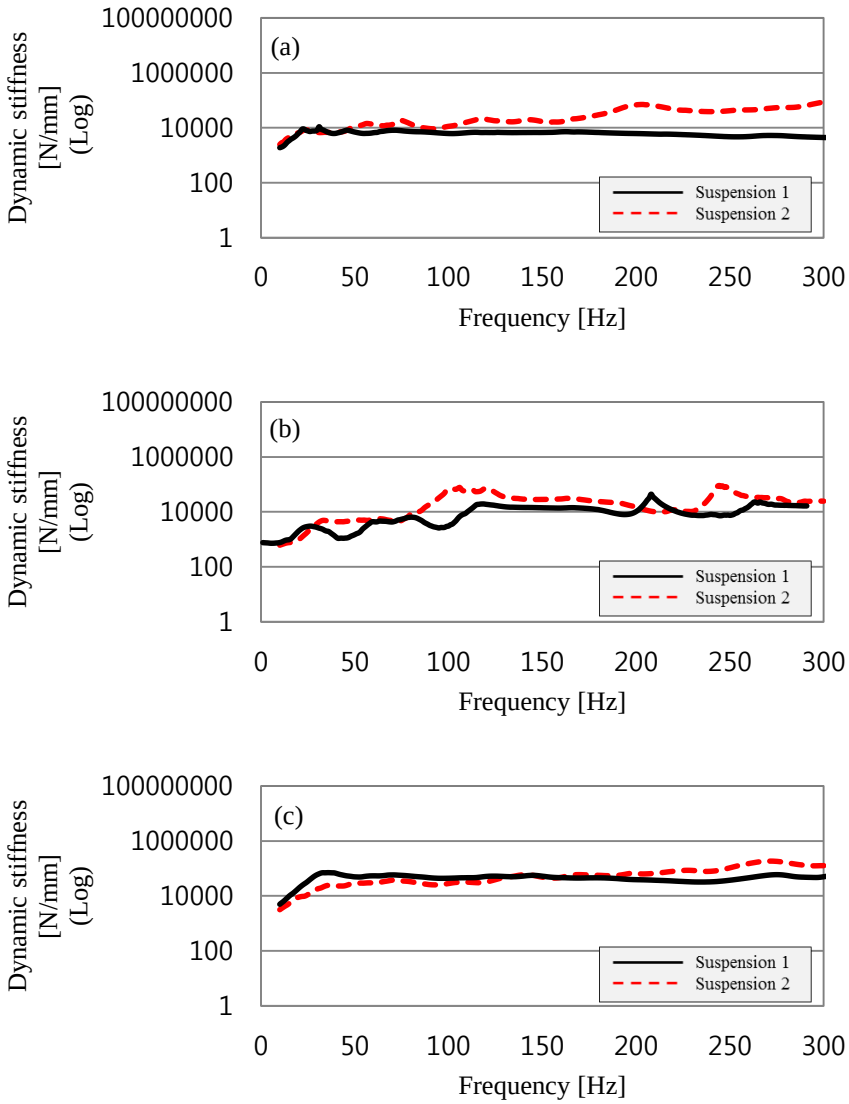

Figure 4.15 Measured dynamic stiffness value for (a) link; (b) bush; and (c) body at Y-dir. lateral arm. (solid) suspension 1, (dotted) suspension 2

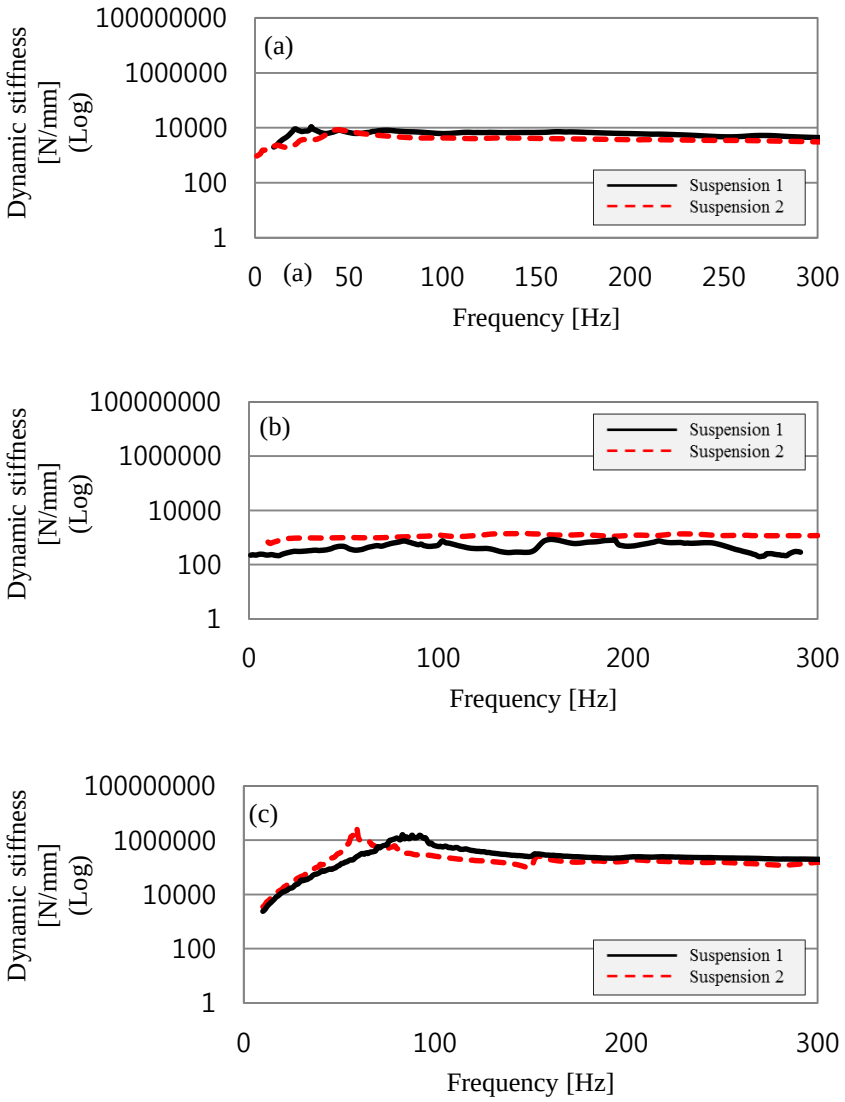

Figure 4.16 Measured dynamic stiffness value for (a) link; (b) bush; and (c) body at X-dir. rear axle front mount. (solid) suspension 1and, (dotted) suspension 2

4.5 Validation results

Figures 4.17 and 4.18 show the calculated force results compared to the measured for U1 and RAFM, respectively. The measured curve is represented in solid line and the calculated curve derived from measured v_{link} is shown in dotted line. The line in dash-dotted represents the calculated curve derived from measured $v_{knuckle}$ signal. The plotted results show that both the calculation driven from the link's active side signal and the knuckle's signal are highly consistent with the measured value for the front suspension. An explanation for this is fairly straightforward: the lateral arm is directly connected to the knuckle, so that the difference between the two calculated curves dose not deviate considerably. The low accuracy of the link driven calculation for this location can be also explained, since the obtained signal contains a high displacement movement causing a strong influence of the rotational components. The rotational influence estimation method can be found in the appendix of this thesis.

On the other hand, for RAFM, the calculation driven from the active side signal is an excellent match to the measured curve. The main reasons for such a high accuracy that was not achieved from the U1 case are as follows: this point is directly mounted to the rigid rig which means that the obtained bush's

dynamic characteristics during the operational excitation are much more reliable as compared to the lateral arm case (which is dominant factor for calculating the force). Also, the excitation's displacement does not contain a large displacement variation; therefore, rotational effect is nearly negligible at this location. The accuracy of the knuckle driven calculation results in contrast is relatively low due to the input to RAFM being far distanced and separated through multi-link and cradle in which vibro-acoustic energy is distributed in many ways. Nevertheless, the curve follows the trend of the measured curve. Therefore, a rough estimation of the force is achievable when using the average value to compare the results with the measured value.

Figure 4.19 is plotted to show how much improvement of force transmission can be achieved by parts' modification from suspension 1 to suspension 2. This can be thought of as the suspension's development scenario where suspension 1 is the first prototype and suspension 2 is the second prototype developed from suspension 1. The measured curve is represented with the solid line, the calculated curve derived from the measured v_{link} is represented with the dotted line, the calculated curve derived from the measured $v_{knuckle}$ is represented with the dash-dotted line, and the estimation with the assumption in Eq. (4.17) is represented with the dash double dotted line.

While the results of the estimated force difference curve (dash double dotted) are not completely satisfactory according to Figure 4.19, it can be clearly seen that the results follow the measured line trend. These results are comprehensible considering that, while all active, passive, and bush's dynamic stiffness values are different between the two systems, in a typical situation within the vehicle development, only one component is changed or modified at a time.

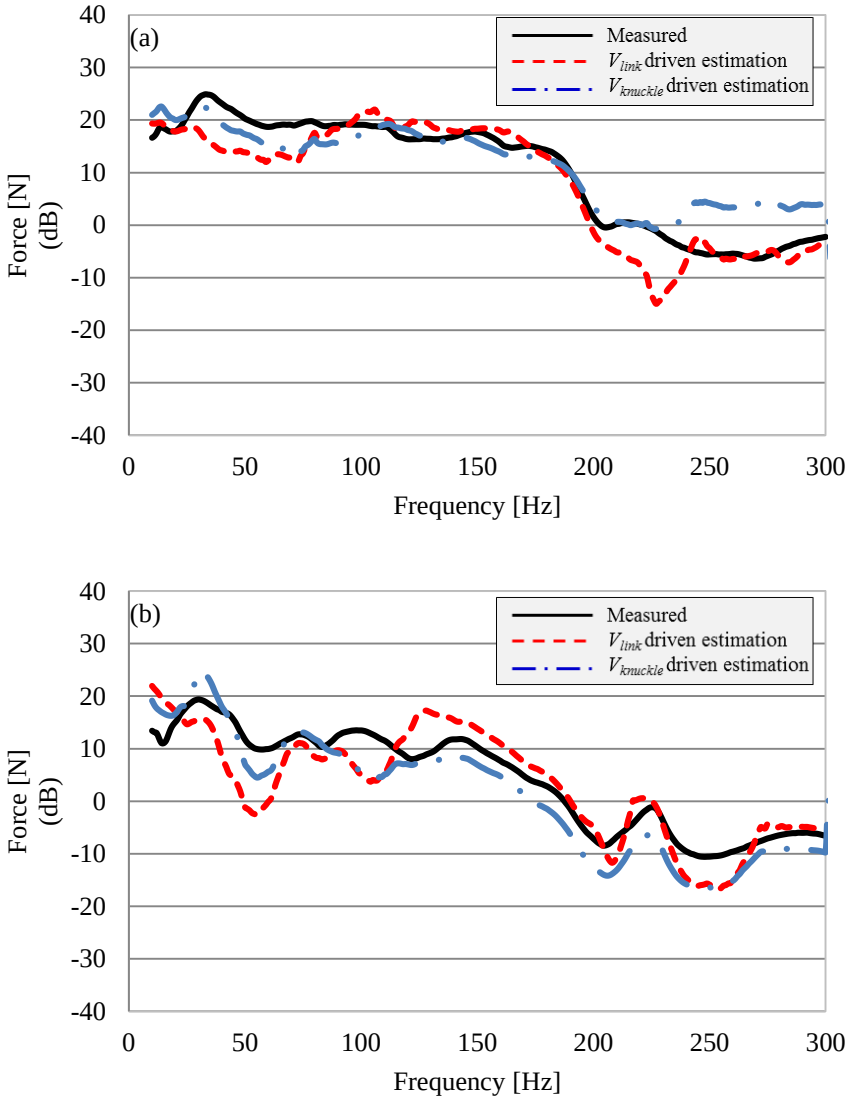

Figure 4.17 The measured (solid line), v_{link} driven calculation (dotted line) ,and $v_{knuckle}$ driven calculation (dash-dotted line) dynamic force comparison at lateral arm Y-dir. for (a) suspension 1 and (b) suspension 2

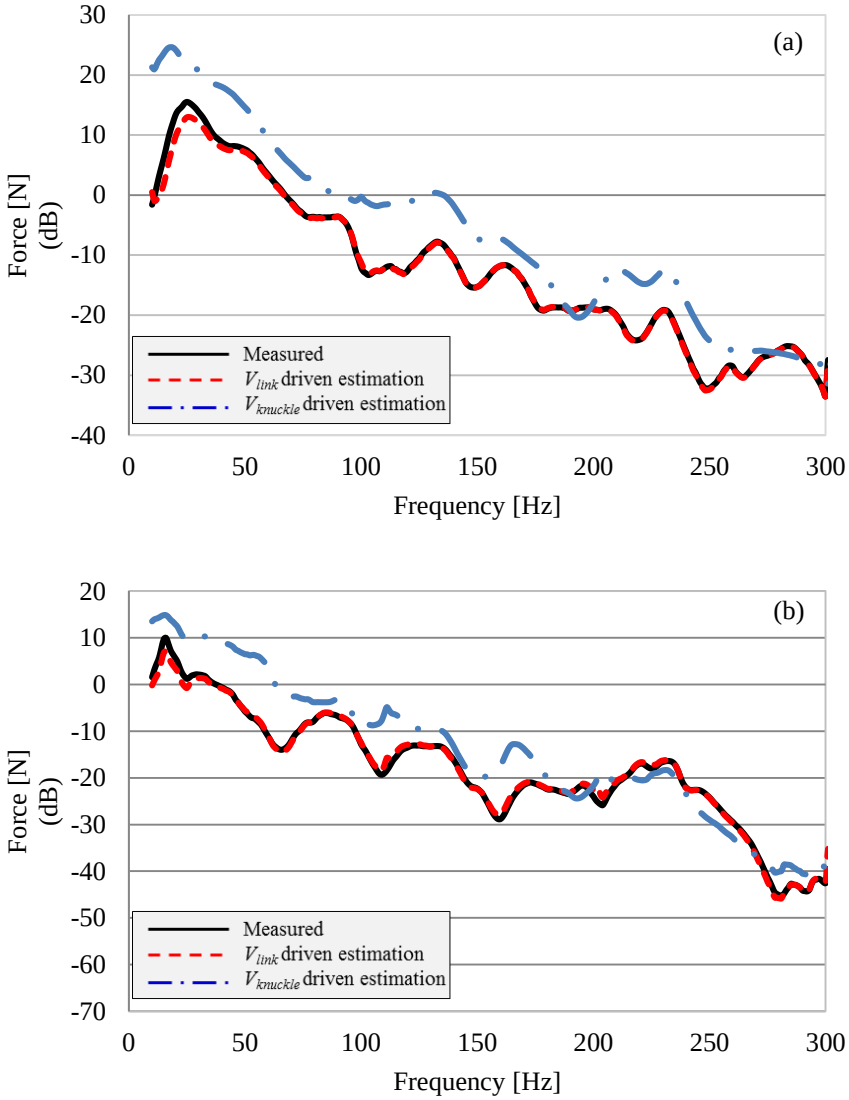

Figure 4.18 The measured (solid line), v_{link} driven calculation (dotted line), and $v_{knuckle}$ driven calculation (dash-dotted line) dynamic force comparison at RAFM X-direction for (a) suspension 1 and (b) suspension 2

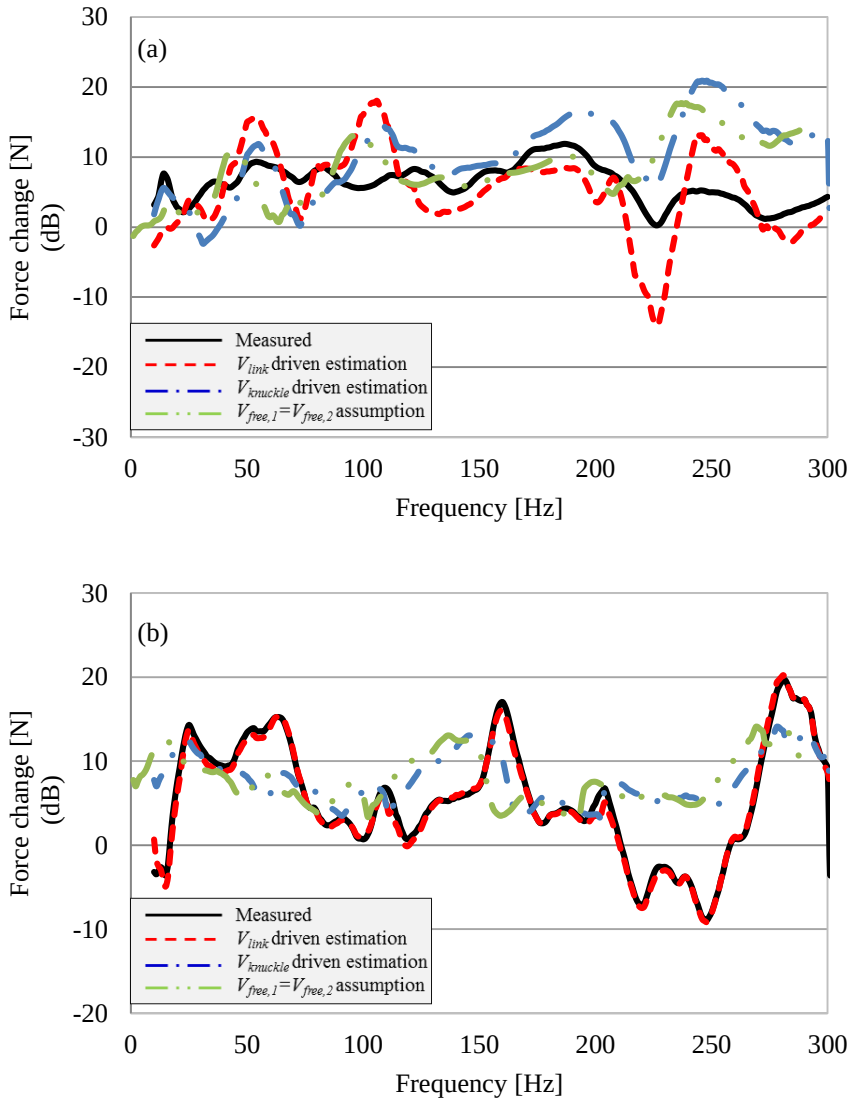

Figure 4.19 Force deviation between suspension 1 and suspension 2. (a) McPherson strut lateral arm in Y-dir., (b) Rear axle front mount in X-dir. measured difference (solid line), v_{link} driven calculation (dotted line), $v_{knuckle}$ driven calculation (dash dotted line), and $v_{free,1} = v_{free,2}$ assumption applied (dash double dotted line).

4.6 Application scenario: bush change on the lateral arm within an actual vehicle

For an actual vehicle development after the design freeze, it is most common that only the connecting bush is optimized, as it is most practical counter measuring solution for improving the structure-borne road noise without a considerable alteration of the system. In this section, to investigate the validity, the lateral arm's link is taken as the actual vehicle development scenario, as it is relatively easy to uninstall and reinstall for swapping the connecting bush in comparison to RAFM. Suspension 1's lateral arm is taken out from the vehicle and substituted with suspension 2's bush and then reinstalled back to the vehicle for the measurement (see Figure 4.20). After this measurement, the bush is substituted back to its original to check the reproducibility of the knuckle's signal. The results are plotted in Figure 4.21.

The front knuckle spectrum measured on the actual vehicle equipped with the original bush (baseline measurement) is represented with the solid line, its bush changed with that of the suspension 2 is represented with the dotted line, and the reproducibility validation curve is represented with the dash dotted line; the excitation method and setup are identical to the previous suspension rig operational condition for all the measurements. According to the results shown

in Figure 4.20, although substituted bush's dynamic stiffness is lower than that of the original bush by nearly the factor of three, the knuckle displacement spectrum is hardly affected, except for a slight peak shift at 87 Hz. This indicates that the previously made assumption (Eq. (4.17)) is valid for estimating the force transmission to vehicle's body due to part modification under the real-world structure-borne road noise application.

Assuming that only the first prototype is available so that there is the absence of the actual dynamic stiffness value of the modified bush, the modified bush's dynamic stiffness value is simply derived by linearly reducing the original bush's dynamic stiffness curve by the factor of three (which is already acquired from dynamic stiffness testing bench) (see Figure 4.22). For validation, due to difficulties of directly measuring the body input force from the actual vehicle, the measured displacement deviation is compared with that of the estimated, rather than with that of the force deviation (see Figure 4.23). The measured displacement difference is represented with the solid line, the estimated one is represented with the dotted line, and the maximum displacement deviation (calculated using the simple Hook's law relation with the assumption that no force transmission is different between the two systems) is represented with the dash dotted line.

The plotted results show, as expected due to only one variable (bush) being changed, the estimated curve is in a very good agreement with the measured curve. The estimated curves being in a perfect agreement with that of the measured curve ensures the accuracy of the force change estimation, even though it cannot be directly compared with the measured data. Therefore, the force change estimation can be only plotted with the maximum possible deviation line calculated with the Hook's law relationship by setting the displacement deviation due to bush swap to zero (see Figure 4.24)

Figure 4.20 Left: Suspension 1's lateral arm with (a) its original bush and (b) swapped suspension 2's bush; Right: Lateral arm's measurement point on the actual vehicle

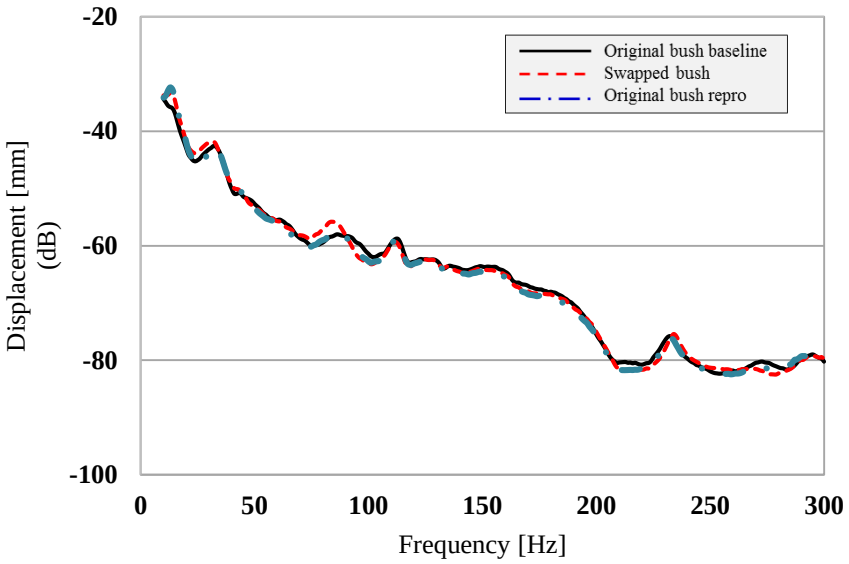

Figure 4.21 Front knuckle displacement spectrum (Y-dir.) obtained from the actual vehicle equipped with suspension 1's original bush (solid line), after the substitution of suspension 2's bush (dotted line), and its original bush substituted back (dash dotted line).

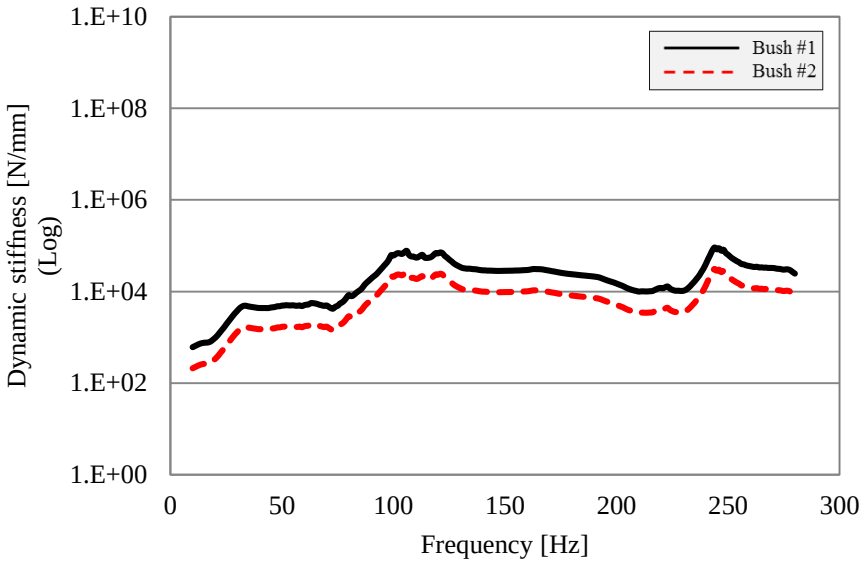

Figure 4.22 Lateral arm bush's dynamic stiffness comparison: prototype 1 (solid line) and prototype 2 (dotted line)

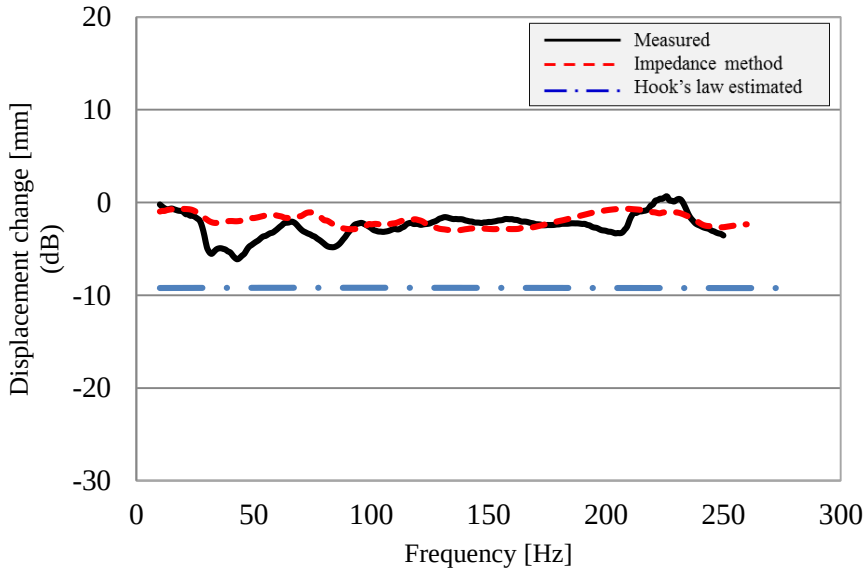

Figure 4.23 Lateral arm's displacement deviation estimation on the actual vehicle: measured (solid line), estimated (dotted line), and maximum deviation value calculated from simple Hook's law relation (dash dotted line)

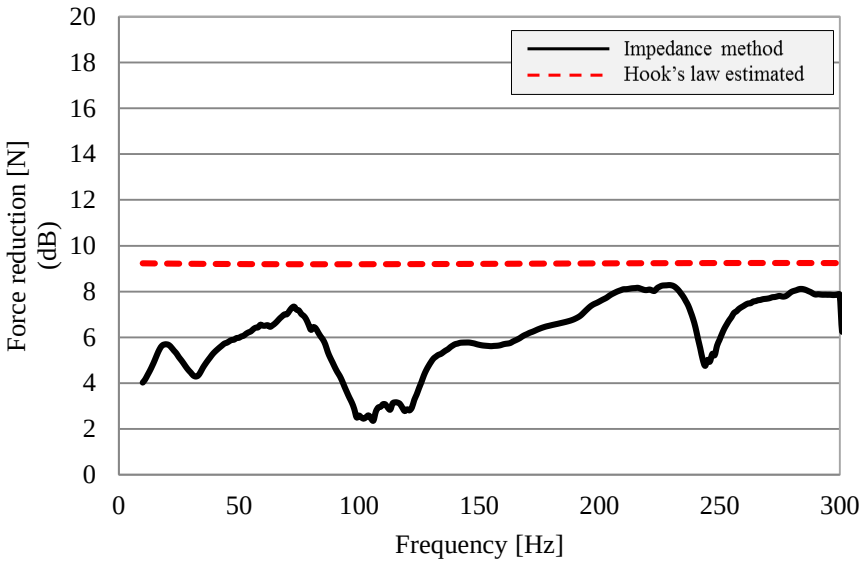

Figure 4.24 Lateral arm's force deviation estimation on the actual vehicle: Estimated (solid line) and possible maximum deviation value calculated from simple Hook's law relation (dotted)

4.7 Summary

In this chapter, a suspension coupled to a vehicle body via an elastomer is modeled by linearly connecting each component which is represented with mechanical impedance. The model is empirically validated under actual road excitation within two different suspension systems: McPherson strut type suspensions in the lateral arm Y direction and Multilink type rear suspension in the front mount X direction. Additionally, a numerical case study is performed

to investigate the potential misleading influences of using the suspension rig in relation to the full vehicle, as well as to find out the cases where the force reduction is difficult to achieve when taking 'softening the connecting bush' as a counter measuring solution. The findings from this chapter can be summarized as follows:

1) Utilizing the Thévenin's equivalent system, the excitation transmission is characterized and it is found that the achievable force reduction deviates with different combinations of all three components (chassis, bush, and body) within a system: The least force reduction is expected with a relatively stiff bush in combination with a relatively soft body, while the most force reduction is expected with a relatively soft bush and stiff body.

2) It is also found that a considerable deviation potentially occurs at a path where the chassis is connected to the body via a relatively stiff bush under rig measurement and the actual vehicle measurement due to their difference in body's dynamic stiffness.

3) It is demonstrated that substituting the knuckle's signal for the free velocity for road noise application is a valid assumption and that the estimated force reduction with such an assumption (calculated solely in terms of the combination of parts' dynamic stiffness) shows acceptable results if the road excitation is reproducible.

4) Within an actual vehicle application, assuming that only one variable is being modified and the excitation is maintained identical, the dynamic stiffness requirement for that particular modified component can be accurately drawn by defining the desirable target force at that transfer path.

CHAPTER 5

DERIVATION OF ROAD NOISE IMPROVEMENT FACTOR WITHIN A SUSPENSION SYSTEM USING THE INVERSE SUBSTRUCTURING METHOD

5.1. Introduction

After obtaining the force distribution and contribution, it is still necessary to identify which component of the suspension is most practical and inexpensive in terms of maintaining the ride and handling quality (as too much of softening joint bushings negatively influences the vehicle's dynamic behavior). Therefore, it is essential to derive the most effective and practical solution for the road noise improvement factor. Another consideration that needs to be taken into consideration using the rig is that it is inevitable to consider the suspension to rig coupling effect in order to more precisely bring the countermeasures driven from the rig measured data to the actual full vehicle system. In response to these caveats, in the present study, the frequency response function-based substructuring (FBS) method is applied, as it is a well-known typical approach for solving structure-related problems.

FBS is a method to predict the dynamic characteristics of a target system by relating those of individual subcomponents and those of an assembly system. The studies concerning FBS are far-reaching in various fields. Among the variety of different approaches within the FBS method, the most common approach uses the Receptance Coupling method, also known as the RC method, which synthesizes the FRF of an assembly system with the use of two independent substructures. In this chapter, the feasibility of using this method to suspension improvement factor derivation is assessed.

5.2. Theoretical background

5.2.1 Frequency response function based sub-structuring modeling

5.2.1.1 Modeling of single degree of freedom single path system

Within a suspension, the components are categorized into the following general terms: the active, passive, and joint bushing. The active side is where the external force is entering and the passive side is the body side where the operational force is transmitted to (see Figure 5.1-(a)). If the conditions of the force equilibrium and displacement compatibility are satisfied, the equal but

opposite reaction force to both active and passive side, R, can be used to obtain the following relation (see Eq. (5.1)-(5.2)):

$$\mathrm{x}^{B} = \mathbf{H}^{B}\mathrm{R}, \tag{5.1}$$

$$\mathrm{x}^{A} = -\mathbf{H}^{A}\mathrm{R} + \mathbf{H}_{oi}^{A}\mathrm{F}. \tag{5.2}$$

In Eq. (5.1) and (5.2), x^{A} and x^{B} represent the respective displacement of active side and passive side, respectively. $\mathbf{H}^{A}$ and $\mathbf{H}^{B}$ are the frequency response characteristic functions for each substructure: A and B, respectively. F is the external force and $\mathbf{H}_{oi}^{A}$ is the transfer function due to the external force F at the point of i to substructure A measured at the point of o.

Taking the FRF of the elastomer bush $\mathbf{H}^{I}$ into account, the relationship between reaction force and displacement of interface can be written as follows (see Eq. (5.3)):

$$\mathrm{x}^{A} - \mathrm{x}^{B} = -\mathbf{H}^{I}\mathrm{R}. \tag{5.3}$$

Substituting Eq. (5.1) and (5.2) into Eq. (5.3) and relocating for the external force and the reaction force term to the right side of the equation give Eq. (5.4).

$$(\mathbf{H}^{A} + \mathbf{H}^{B} + \mathbf{H}^{I})R = \mathbf{H}_{oi}^{A}\mathrm{F}. \tag{5.4}$$

When the external force is regarded as the two separate input forces caused by right- and left-wheel for the application of this model to an actual vehicle (see Figure 5.1-(b)), the equation for the reaction force can be expressed as follows (see Eq. (5.5)-(5.6)):

$$\mathrm{R} = (\mathbf{H}_{11}^{I} + \mathbf{H}_{11}^{A} + \mathbf{H}_{11}^{B})^{-1}[\mathbf{H}_{1f_1} \quad \mathbf{H}_{1f_2}][\mathrm{F}_1 \quad \mathrm{F}_2]^{T}, \tag{5.5}$$

$$\mathrm{R} = (\mathbf{H}_{11}^{I} + \mathbf{H}_{11}^{A} + \mathbf{H}_{11}^{B})^{-1}\left(\mathbf{H}_{1f_1}\mathrm{F}_1 + \mathbf{H}_{1f_2}\mathrm{F}_2\right). \tag{5.6}$$

In Eq. (5.5) and (5.6), the subscription represents the excitation and response point of the measured FRF and the superscription represents the substructure component (i.e. $\mathbf{H}_{11}^{A}$ is the FRF measured on response point 1 within the substrcutre A due to the excitation at that same point 1). Similarly, $\mathbf{H}_{1f_1}$ represents the FRF from the point where the external force acts to the response point 1, F_1. Considering the scenario where the joint bushing is modified and the other structures remain the same, the changed reaction force, due to the modification of bush dynamic property, R', can be written as follows (see Eq. (5.7)):

$$\mathrm{R}' = \left(\mathbf{H}_{11}^{I}{}' + \mathbf{H}_{11}^{A} + \mathbf{H}_{11}^{B}\right)^{-1}\left(\mathbf{H}_{1f_1}\mathrm{F}_1 + \mathbf{H}_{1f_2}\mathrm{F}_2\right). \tag{5.7}$$

Consequently, the reaction force of a system can be predicted from Eq. (5.6). Using Eq. (5.6) and (5.7), the transmissibility of body input force can be defined as follows (see Eq. (5.8)):

$$\mathrm{TR} = \frac{\mathrm{R}'}{\mathrm{R}} = \frac{\mathbf{H}_{11}^{I} + \mathbf{H}_{11}^{A} + \mathbf{H}_{11}^{B}}{\mathbf{H}_{11}^{I}{}' + \mathbf{H}_{11}^{A} + \mathbf{H}_{11}^{B}}. \tag{5.8}$$

Using the transmissibility of the input force above, it is possible to evaluate the characteristics of body input force due to the bush modification within a single path system.

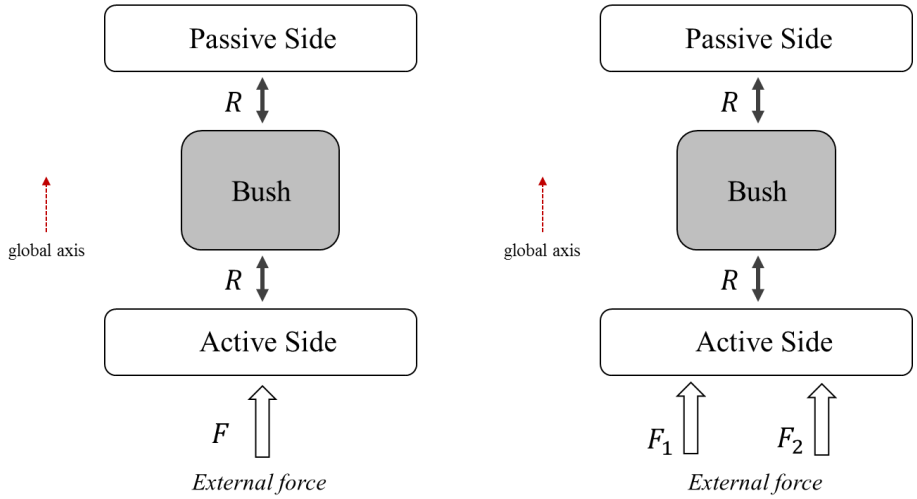

(a) (b)

Figure 5.1 Schematic diagram of the force transmitted system with a single path: (a) single external force system; (b) two external force systems

5.2.1.2 Modeling of a multi-path system

When expanding the modeling to multiple pathway system, the cross terms of matrix form should be considered. As a pathway or a degree of freedom increases, the matrix becomes more complex, but the basic principle remains the same. For example, having two pathways within a system (see Figure 5.2) can be expressed as follows (see Eq. (5.9)):

$$\begin{bmatrix} \mathbf{H}_{11}^{I} + \mathbf{H}_{11}^{A} + \mathbf{H}_{11}^{B} & \mathbf{H}_{12}^{A} + \mathbf{H}_{12}^{B} \\ \mathbf{H}_{21}^{A} + \mathbf{H}_{21}^{B} & \mathbf{H}_{22}^{I} + \mathbf{H}_{22}^{A} + \mathbf{H}_{22}^{B} \end{bmatrix} \begin{bmatrix} \mathrm{R}_1 \\ \mathrm{R}_2 \end{bmatrix} = \begin{bmatrix} \mathbf{H}_{1f_1} & \mathbf{H}_{1f_2} \\ \mathbf{H}_{2f_1} & \mathbf{H}_{2}f_2 \end{bmatrix} \begin{bmatrix} \mathrm{F}_1 \\ \mathrm{F}_2 \end{bmatrix}. \tag{5.9}$$

Solving for the reaction force, Eq. (5.9) can be rewritten as follows (see Eq. (5.10)):

$$\begin{bmatrix} \mathrm{R}_1 \\ \mathrm{R}_2 \end{bmatrix} = [\mathbf{H}]^{-1} \begin{bmatrix} \mathbf{H}_{1f_1} & \mathbf{H}_{1f_2} \\ \mathbf{H}_{2f_1} & \mathbf{H}_{2}f_2 \end{bmatrix} \begin{bmatrix} \mathrm{F}_1 \\ \mathrm{F}_2 \end{bmatrix}, \tag{5.10}$$

where

$$[\mathbf{H}] = \begin{bmatrix} \mathbf{H}_{11}^{I} + \mathbf{H}_{11}^{A} + \mathbf{H}_{11}^{B} & \mathbf{H}_{12}^{A} + \mathbf{H}_{12}^{B} \\ \mathbf{H}_{21}^{A} + \mathbf{H}_{21}^{B} & \mathbf{H}_{22}^{I} + \mathbf{H}_{22}^{A} + \mathbf{H}_{22}^{B} \end{bmatrix} = \begin{bmatrix} \mathbf{H}_{11} & \mathbf{H}_{12} \\ \mathbf{H}_{21} & \mathbf{H}_{22} \end{bmatrix}. \tag{5.11}$$

The $\mathbf{H}$ matrix consists of receptance FRF matrix which corresponds to the interface of each pathway. The substructure components $\mathbf{H}^{\mathrm{I}}$, $\mathbf{H}^{A}$ and $\mathbf{H}^{B}$ represent the receptance of bush, active side, and passive side, respectively.

Therefore, for the case where the bushing of the pathway number 1 is modified, Eq. (5.10) can be rewritten as shown in Eq. (5.12)-(5.13).

$$\begin{bmatrix} \mathrm{R}_1{}' \\ \mathrm{R}_2 \end{bmatrix} = [\mathbf{H}']^{-1} \begin{bmatrix} \mathbf{H}_{1f_1} & \mathbf{H}_{1f_2} \\ \mathbf{H}_{2f_1} & \mathbf{H}_{2}f_2 \end{bmatrix} \begin{bmatrix} \mathrm{F}_1 \\ \mathrm{F}_2 \end{bmatrix}, \tag{5.12}$$

$$[\mathbf{H}'] = \begin{bmatrix} \mathbf{H}_{11}^{I}{}' + \mathbf{H}_{11}^{A} + \mathbf{H}_{11}^{B} & \mathbf{H}_{12}^{A} + \mathbf{H}_{12}^{B} \\ \mathbf{H}_{21}^{A} + \mathbf{H}_{21}^{B} & \mathbf{H}_{22}^{I} + \mathbf{H}_{22}^{A} + \mathbf{H}_{22}^{B} \end{bmatrix} = \begin{bmatrix} \mathbf{H}'_{11} & \mathbf{H}_{12} \\ \mathbf{H}_{21} & \mathbf{H}_{22} \end{bmatrix} \tag{5.13}$$

where the superscript $'$ represents the modified dynamic property.

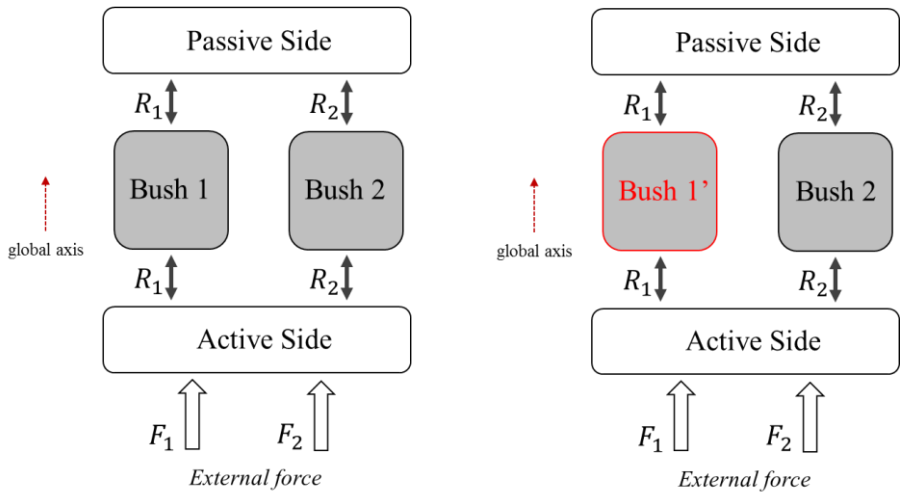

(a) (b)

Figure 5.2 Schematic diagram of the force transmitted system with double paths: (a) single external force system; (b) two external force systems

5.2.2 Input force estimation

Eq. (5.10) and (5.12) lead to the following definition of the transmissibility of reaction force (see Eq. (5.14)):

$$\mathrm{TR}_n = \frac{\mathrm{R}'_n}{\mathrm{R}_n}. \tag{5.14}$$

The reaction forces R'_n and R_n which take place in the n-th path of the system are dependent on the relations of FRF of subcomponents in each system.

The force change due to the bush modification scenario shown in Figure 5.2 thus can be written as follows (see Eq. (5.15)-(5.16)):

$$\begin{aligned} \mathrm{TR}_1 &= \frac{\mathrm{R}_1'}{\mathrm{R}_1} \\ &= \frac{D(\mathbf{H})[\mathbf{H}_{22}\left(\mathbf{H}_{1f_1}\mathrm{F}_1 + \mathbf{H}_{1f_2}\mathrm{F}_1\right) - \mathbf{H}_{12}(\mathbf{H}_{1f_1}\mathrm{F}_1 + \mathbf{H}_{1f_2}\mathrm{F}_2)]}{D(\mathbf{H}')[\mathbf{H}_{22}\left(\mathbf{H}_{1f_1}\mathrm{F}_1 + \mathbf{H}_{1f_2}\mathrm{F}_1\right) - \mathbf{H}_{12}(\mathbf{H}_{1f_1}\mathrm{F}_1 + \mathbf{H}_{1f_2}\mathrm{F}_2)]} \end{aligned} \tag{5.15}$$

$$\begin{aligned} \mathrm{TR}_2 &= \frac{\mathrm{R}_2'}{\mathrm{R}_2} \\ &= \frac{D(\mathbf{H})[\mathbf{H}_{11}'\left(\mathbf{H}_{2f_1}\mathrm{F}_1 + \mathbf{H}_{2f_2}\mathrm{F}_2\right) - \mathbf{H}_{21}(\mathbf{H}_{1f_1}\mathrm{F}_1 + \mathbf{H}_{1f_2}\mathrm{F}_2)]}{D(\mathbf{H}')[\mathbf{H}_{11}\left(\mathbf{H}_{2f_1}\mathrm{F}_1 + \mathbf{H}_{2f_2}\mathrm{F}_2\right) - \mathbf{H}_{21}(\mathbf{H}_{1f_1}\mathrm{F}_1 + \mathbf{H}_{1f_2}\mathrm{F}_2)]}, \end{aligned} \tag{5.16}$$

where

$$D(\mathbf{H}) = |\mathbf{H}|. \tag{5.17}$$

$D(\mathbf{H})$ indicates the determinant of the matrix $\mathbf{H}$. From Eq. (5.17), one can intuitively notice that the transmissibility can be predicted if dynamic characteristics of substructure component properties are known.

5.2.3 Inverse sub-structuring method

Within the general FBS formulation for practical application, the dynamic characteristics properties of sub systems are measured separately and synthesized together to predict the total system. However, the joint bushing and the suspension system is a coupled system that cannot be easily separated, as it requires special press which might cause damage or permanent deformation of

the bush when using it. Therefore, the inverse formulation approach is deployed. Since the dynamic characteristics of individual component cannot be obtained directly, the sub component's dynamic properties are inversely calculated using the method originally introduced by Lim et al. The feasibility of deriving the road noise improvement factor by deploying this method to the suspension model to inversely calculate the properties of mount bushing attached to the sub-frame is studied.

Figure 5.3 illustrates the bush to sub-frame coupling mount in a single-degree-of-freedom model substituting the bushing with a simple spring. From this model, the following equations are drawn (see Eq. (5.18)-(5.19)):

$$\mathrm{F}_a = \mathbf{H}_{aa}^{A\ -1}\mathrm{x}_a + \mathbf{K}_{ab}(\mathrm{x}_a - \mathrm{x}_b), \tag{5.18}$$

$$\mathrm{F}_b = \mathbf{H}_{bb}^{B\ -1}\mathrm{x}_b + \mathbf{K}_{ab}(\mathrm{x}_b - \mathrm{x}_a). \tag{5.19}$$

F_a and F_b represent the force applied to the bush interface of substructure A and substructure B, respectively. x is the resultant displacement, K represents the dynamic stiffness of the bushing from the coupled system, and $\mathbf{H}$ is receptance of the bush. The subscripts a and b indicate components of substructure A and B, respectively. The two formula can be expressed in the form of matrix (see Eq. (5.20)).

$$\begin{vmatrix} \mathbf{H}_{aa} & \mathbf{H}_{ab} \\ \mathbf{H}_{ba} & \mathbf{H}_{bb} \end{vmatrix} \tag{5.20}$$

=

$$\begin{vmatrix} \mathbf{H}_{aa}^{A\ -1} + \mathrm{K}_{ab} & -\mathbf{K}_{ab} \\ -\mathbf{K}_{ab} & \mathbf{H}_{bb}^{B\ -1} + \mathbf{K}_{ab} \end{vmatrix}^{-1} \begin{vmatrix} \mathbf{H}_{bb}^{B\ -1} + \mathbf{K}_{ab} & \mathbf{K}_{ab} \\ \mathbf{K}_{ab} & \mathbf{H}_{aa}^{A\ -1} + \mathbf{K}_{ab} \end{vmatrix} \begin{Bmatrix} \mathrm{F}_a \\ \mathrm{F}_b \end{Bmatrix}.$$

Solving for K_{ab}, the following is obtained (see Eq. (5.21)):

$$\mathbf{K}_{ab} = \frac{\mathbf{H}_{ab}}{\mathbf{H}_{aa}\mathbf{H}_{bb} - \mathbf{H}_{ab}^2}. \tag{5.21}$$

The Eq. (5.21) shows that the dynamic stiffness property of the joint bushing is expressed using assembled system's FRF. Expanding the Eq. (5.21) to the system with a multi-coordinate coupling model, the following is obtained.

$$\mathbf{K}_{ab} = \left([\mathbf{H}]_{aa}[\mathbf{H}]_{ab}^{-T}[\mathbf{H}]_{bb} - [\mathbf{H}]_{ab}\right)^{-1} = [\mathbf{H}^I]^{-1}. \tag{5.22}$$

Similarly, the FRF of the connecting point is obtained

$$\mathbf{H}_{aa}^X = \frac{\mathbf{H}_{aa}\mathbf{H}_{bb} - \mathbf{H}_{ab}^2}{\mathbf{H}_{xx} - \mathbf{H}_{ab}}, \tag{5.23}$$

where

$$X = A, B, \qquad x = \begin{cases} b & \text{when} \quad X = A \\ a & \text{when} \quad X = B \end{cases}.$$

Thus, all information necessary for calculating the transmissibility is obtained.

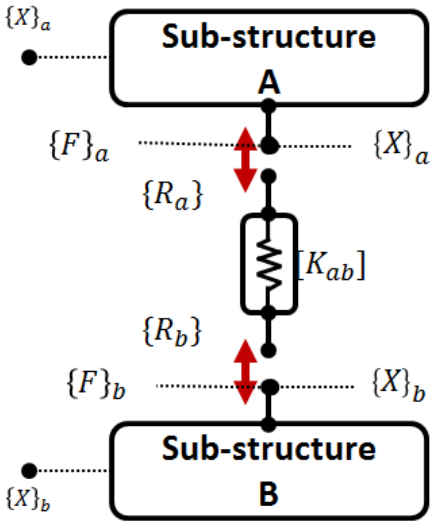

Figure 5.3 The model of two substructures connected with a single joint

5.3 Cross member mount points modeling

Cross member becomes a channel by which vibro-acoustic energy is transmitted from the road excitation to the vehicle body. The typical cross member consists of total four mounting points (see Figure 5.4). The rubber mounts that couples the vehicle and suspension works as the vibration isolator and, therefore, are most often tackled parts when it comes to ameliorating the NVH performance of the suspension. The schematic diagram of modeled cross member is shown in Figure 5.5.

Figure 5.4 Rear cross member

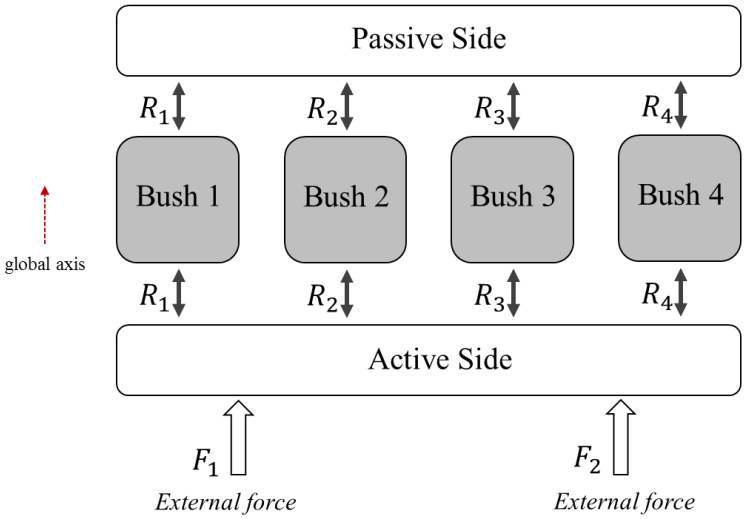

(a)

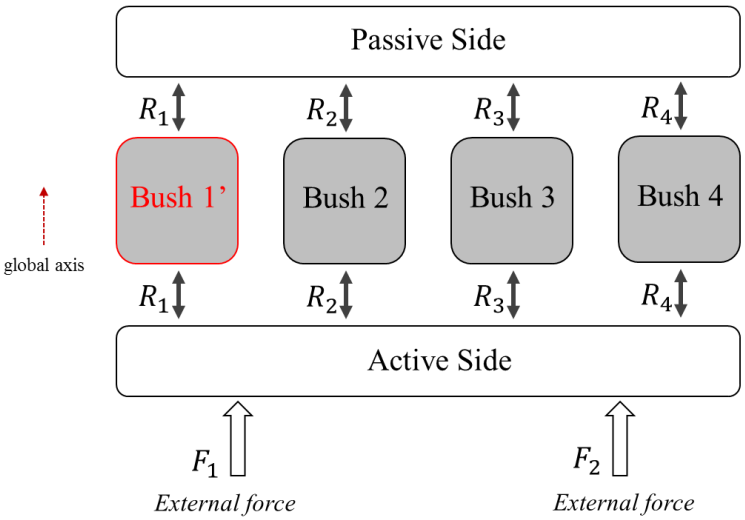

(b)

Figure 5.5 Schematic diagram of the rear suspension and body combined system (a) with original bush, (b) with tuned bush.

Expanding Eq. (5.10) for four pathway system for cross member model, Eq. (5.24) is obtained.

$$\begin{bmatrix} \mathrm{R}_1 \\ \mathrm{R}_2 \\ \mathrm{R}_3 \\ \mathrm{R}_4 \end{bmatrix} = [\mathbf{H}]^{-1} \begin{bmatrix} \mathbf{H}_{1f_1}^A & \mathbf{H}_{1f_2}^A \\ \mathbf{H}_{2f_1}^A & \mathbf{H}_{2f_2}^A \\ \mathbf{H}_{3f_1}^A & \mathbf{H}_{3f_2}^A \\ \mathbf{H}_{4f_1}^A & \mathbf{H}_{4f_2}^A \end{bmatrix} \begin{bmatrix} \mathrm{F}_1^A \\ \mathrm{F}_2^A \end{bmatrix}, \tag{5.24}$$

where

$$[\mathbf{H}] = \begin{bmatrix} \mathbf{H}_{11}^I + \mathbf{H}_{11}^A + \mathbf{H}_{11}^B & \mathbf{H}_{12}^A + \mathbf{H}_{12}^B & \mathbf{H}_{13}^A + \mathbf{H}_{13}^B & \mathbf{H}_{14}^A + \mathbf{H}_{14}^B \\ \mathbf{H}_{21}^A + \mathbf{H}_{21}^B & \mathbf{H}_{22}^I + \mathbf{H}_{22}^A + \mathbf{H}_{22}^B & \mathbf{H}_{23}^A + \mathbf{H}_{23}^B & \mathbf{H}_{24}^A + \mathbf{H}_{24}^B \\ \mathbf{H}_{31}^A + \mathbf{H}_{31}^B & \mathbf{H}_{32}^A + \mathbf{H}_{32}^B & \mathbf{H}_{33}^I + \mathbf{H}_{33}^A + \mathbf{H}_{33}^B & \mathbf{H}_{34}^A + \mathbf{H}_{34}^B \\ \mathbf{H}_{41}^A + \mathbf{H}_{41}^B & \mathbf{H}_{42}^A + \mathbf{H}_{42}^B & \mathbf{H}_{43}^A + \mathbf{H}_{43}^B & \mathbf{H}_{44}^I + \mathbf{H}_{44}^A + \mathbf{H}_{44}^B \end{bmatrix}. \tag{5.25}$$

Assuming that the excitation force to the body through the knuckles on the right and left wheels are the same, considering that the cross member is perfectly symmetric structure, Eq. (5.26) is satisfied.

$$\mathbf{H}_{2f_1}\mathrm{F}_1 + \mathbf{H}_{2f_2}\mathrm{F}_2 = \mathbf{H}_{1f_1}\mathrm{F}_1 + \mathbf{H}_{1f_2}\mathrm{F}_2. \tag{5.26}$$

Applying this assumption, the transmissibility is represented with sole terms of $D(\mathbf{H})$ and $D(\mathbf{H}')$ (see Eq. (5.27)).

$$\mathrm{TR}_1 = \frac{D(\mathbf{H})}{D(\mathbf{H}')}. \tag{5.27}$$

In Eq. (5.27), $D(\mathbf{H}')$ is the determinant only when the dynamic property of pathway 1 bushing is changed. The FRF $\mathbf{H}'$ when the busing of the pathway 1 is changed is as follows (see Eq. (5.28)):

$$[\mathbf{H}'] = \begin{bmatrix} \mathbf{H}_{11}^{I\,\prime} + \mathbf{H}_{11}^{A} + \mathbf{H}_{11}^{B} & \mathbf{H}_{12}^{A} + \mathbf{H}_{12}^{B} & \mathbf{H}_{13}^{A} + \mathbf{H}_{13}^{B} & \mathbf{H}_{14}^{A} + \mathbf{H}_{14}^{B} \\ \mathbf{H}_{21}^{A} + \mathbf{H}_{21}^{B} & \mathbf{H}_{22}^{I} + \mathbf{H}_{22}^{A} + \mathbf{H}_{22}^{B} & \mathbf{H}_{23}^{A} + \mathbf{H}_{23}^{B} & \mathbf{H}_{24}^{A} + \mathbf{H}_{24}^{B} \\ \mathbf{H}_{31}^{A} + \mathbf{H}_{31}^{B} & \mathbf{H}_{32}^{A} + \mathbf{H}_{32}^{B} & \mathbf{H}_{33}^{I} + \mathbf{H}_{33}^{A} + \mathbf{H}_{33}^{B} & \mathbf{H}_{34}^{A} + \mathbf{H}_{34}^{B} \\ \mathbf{H}_{41}^{A} + \mathbf{H}_{41}^{B} & \mathbf{H}_{42}^{A} + \mathbf{H}_{42}^{B} & \mathbf{H}_{43}^{A} + \mathbf{H}_{43}^{B} & \mathbf{H}_{44}^{I} + \mathbf{H}_{44}^{A} + \mathbf{H}_{44}^{B} \end{bmatrix}. \tag{5.28}$$

Similarly, TR_2 becomes

$$\begin{aligned} \mathrm{TR}_2 &= \mathrm{TR}_1 + \mathrm{TR}_1 \frac{\mathbf{H}'^{I}_{11} - \mathbf{H}^{I}_{11}}{\mathbf{H}_{11} - \mathbf{H}_{21}} \\ &= \mathrm{TR}_1 + \mathrm{TR}_1 \frac{\frac{1}{\alpha} - 1}{(1 + \frac{\mathbf{H}_{11}^{A}}{\mathbf{H}_{11}^{I}} + \frac{\mathbf{H}_{11}^{B}}{\mathbf{H}_{11}^{I}}) - (\frac{\mathbf{H}_{21}^{A}}{\mathbf{H}_{11}^{I}} + \frac{\mathbf{H}_{21}^{B}}{\mathbf{H}_{11}^{I}})}. \end{aligned} \tag{5.29}$$

where α represents the ratio of the original and modified dynamic characteristic of the active side component within the system. That is, as shown in Eq. (5.30),

$$\mathbf{K}'_{bush} = \alpha \mathbf{K}_{bush}. \tag{5.30}$$

Thus, the FRF relation becomes as follows (see Eq. (31)):

$$\mathbf{H}_{11}^{I\,\prime} = \frac{1}{\alpha}\mathbf{H}_{11}^{I}. \tag{5.31}$$

Similarly, β is used for representing the deviation ration between the original and the modified dynamic stiffness at the passive side (see Eq. (5.32)-(5.33)).

$$\mathbf{K}'_{passive} = \beta \mathbf{K}_{passive}, \tag{5.32}$$

$$\mathbf{H}_{11}^{B\,\prime} = \frac{1}{\beta}\mathbf{H}_{11}^{B}. \tag{5.33}$$

Relating this information to solve for α, Eq. (5.34) is obtained.

$$\alpha = \frac{\mathbf{H}_{11}^{I}}{\mathbf{H}_{11}^{B}\left(\frac{1}{\mathrm{TR}_1} - \frac{1}{\beta}\right) + \mathbf{H}_{11}^{A}\left(\frac{1}{\mathrm{TR}_1} - 1\right) + \mathbf{H}_{11}^{I}\frac{1}{\mathrm{TR}_1}}. \qquad (5.34)$$

Using this relation, by choosing desired TR value, it is possible to derive the dynamic stiffness requirement of bush in order to achieve that particular TR level. From Eq. (5.33), it is also evident that efficiency in changing β is very low to achieve the same amount of TR level in comparison to that can be achieved with changing α.

Within the cross member example, the stiffness of bush is much smaller than the cross member frame. Therefore, the following assumption can be made (see Eq. (5.35)):

$$\mathbf{H}_{ij}^{I} \gg \mathbf{H}_{kk}^{X}, \qquad (5.35)$$

Where $i, j, k = 1,2,3,4 \ \ and \ \ X = A, B$.Therefore, Eq. (5.28) can be simplified as shown in Eq. (5.36).

$$\mathrm{TR}_2 = \mathrm{TR}_1\left(1 + \frac{\left(\frac{1}{\alpha} - 1\right)\mathrm{P}_2}{\mathrm{Q}_2 + \mathrm{P}_2}\right), \qquad (5.36)$$

Similarly, as shown in Eq. (5.37)-(5.38),

$$\mathrm{TR}_3 = \mathrm{TR}_1\left(1 + \frac{\left(\frac{1}{\alpha} - 1\right)\mathrm{P}_3}{\mathrm{Q}_3 + \mathrm{P}_3}\right), \qquad (5.37)$$

$$\mathrm{TR}_4 = \mathrm{TR}_1\left(1 + \frac{\left(\frac{1}{\alpha} - 1\right)\mathrm{P}_4}{\mathrm{Q}_4 + \mathrm{P}_4}\right), \qquad (5.38)$$

where

$$\begin{aligned} \mathrm{P}_l = \mathbf{H}_{11}^I \mathbf{H}_{mm}^I (\mathbf{H}_{nn}^A + \mathbf{H}_{nn}^B) \\ + \mathbf{H}_{11}^I \mathbf{H}_{nn}^I (\mathbf{H}_{mm}^A + \mathbf{H}_{mm}^B) \\ - \mathbf{H}_{11}^I \mathbf{H}_{mm}^I (\mathbf{H}_{mn}^A + \mathbf{H}_{mn}^B) \\ - \mathbf{H}_{11}^I \mathbf{H}_{nn}^I (\mathbf{H}_{mm}^A + \mathbf{H}_{mm}^B), \end{aligned} \tag{5.39}$$

$$\begin{aligned} \mathrm{Q}_l = \mathbf{H}_{11}^I \mathbf{H}_{mm}^I \mathbf{H}_{nn}^I + \mathbf{H}_{mm}^I \mathbf{H}_{nn}^I (\mathbf{H}_{11}^A + \mathbf{H}_{11}^B) \\ - \mathbf{H}_{mm}^I \mathbf{H}_{jj}^I (\mathbf{H}_{1m}^A + \mathbf{H}_{1m}^B), \\ (l, m, n = 2, 3, 4, \quad l \neq m \neq n \\ \neq l). \end{aligned} \tag{5.40}$$

5.4. Experimental validation

5.4.1 Test setup

For the validation of checking the feasibility of applying inverse formulation approach for deriving the road noise improvement factor, the estimated transmissibility from the model should be compared with the experimental data. In this regard, a special cross member kit that enables easy access of modifying bushes is developed. The target system is illustrated in Figure 5.6. As shown in Figure 5.6, the cross member kit is developed as the

detachable mount bush in order to modify the dynamic stiffness of mount bushing against the general cross member.

Figure 5.7 illustrates the location where each FRF is obtained for the estimation. In addition, the detailed setup for the specially developed kit and the location for acquiring FRFs is shown. Prior to carrying out the inverse formulation, the settings for comparing the FRF differences at the attachment areas between the bush and the cross member are depicted in Figure 5.7(a). In this case, the accelerometers, which are set up in the attachment area between the cross member cylindrical mounting bracket and the bushing interface, measure the dynamic property at the each four adjacent points. From this setup, $\mathbf{H}^A$ can be obtained by using a cross member kit.

The passive side mount FRF is measured while the rig is floated on the air bellow which acts as a soft spring, and the active side cross member's FRF is obtained under the mimicked free-free boundary using a soft elastic rope (see Figure 5.8). In this setup, the passive side FRF, $\mathbf{H}^B$, is measured as depicted in Figure 5.7(b). The $\mathbf{H}^I$ is calculated by using measured $\mathbf{H}_{aa}$, $\mathbf{H}_{ab}$, $\mathbf{H}_{ba}$ and $\mathbf{H}_{bb}$ shown on Figure 5.7(c). The measurement of FRF in the assembly system for evaluating the estimation force is shown in Figure 5.9, where PCB 260A02 tri-axial force sensor is installed to measure the direct force. In the entire

process undertaken in the present study, LMS SCADAS Mobile FFT analyzer was used to measure the signals.

For the validation experiment, The FRF of the cross member kit, $\mathbf{H}^A$, the FRF of the mounting point of force rig, $\mathbf{H}^B$, and the FRF of the assembled bush, $\mathbf{H}^I$, are measured using a B&K 2806-002 impact hammer. In addition, PCB 333B32 uni-axial accelerometers are used to obtain transfer functions for all FRF measurements. These accelerometers are installed for each pathway on both active and passive sides, and the hammer excitation point is created using an aluminum cubical block weighing less than 20 g for accurate vertical excitation (see Figures 5.6-5.9). For the external forces, the burst random excitation up to 1,000 Hz using B&K 4825 shaker and PCB force transducer 2080C02 at the predetermined location on the cross member is created (see Figure 5.9).

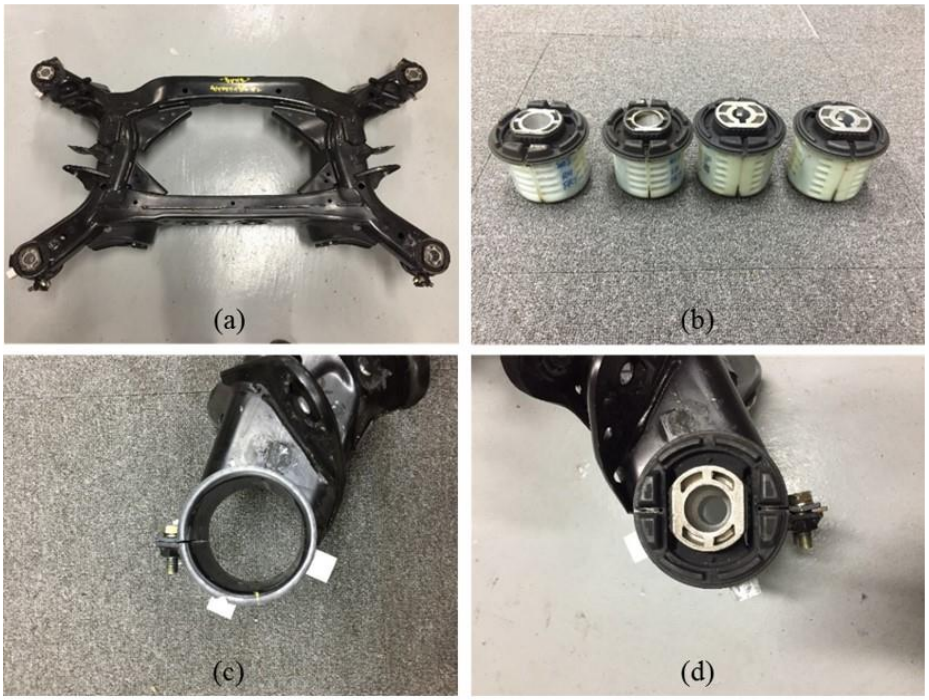

Figure 5.6 Composition of the bush kit: (a) cross member bush kit; (b) mount bushes; (c) mounting point when bush is removed; (d) mounting point when bush is installed

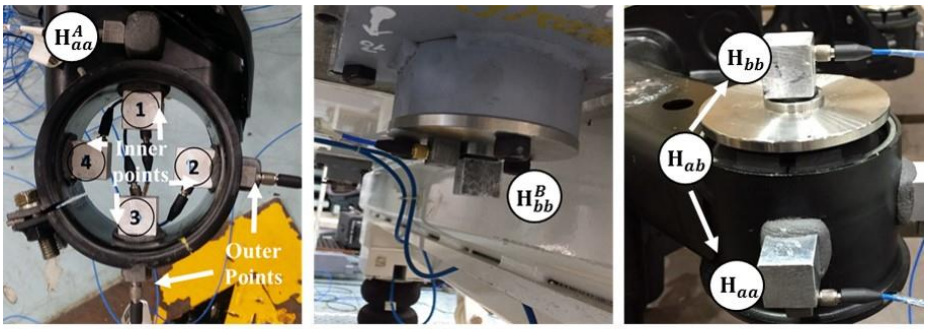

Figure 5.7 The points of accelerometer installation and excitation for measuring FRF measurement: (a) experimental setup for getting active side FRF $\mathbf{H}^{A}$; (b) mount block to measure the passive side FRF $\mathbf{H}^{B}$; (c) experimental setup for estimating the $\mathbf{H}^{I}$

Figure 5.8 (a) Suspension rig measurement setup on air bellows; (b) cross member FRF measurement in the free-free boundary condition

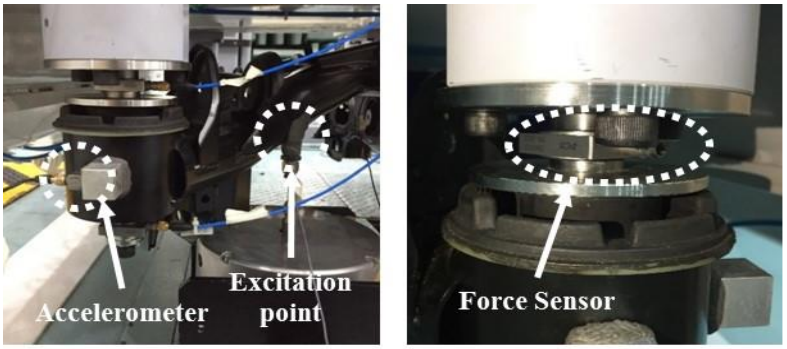

Figure 5.9 (a) Experimental setup for measuring the external force and comparing with estimation force; (b) installed force sensor at the mounting point

5.4.2 Bushing property extraction

Within an actual suspension cross member from a vehicle, it is difficult to acquire the dynamic characteristics of sole joint bushing, as the joint bushing itself is secured on the cross member, requiring right tools and effort to be separated. Accordingly, the inverse formulation method is applied to deliver the joint bushing property using the data obtained from assembled system—that is, without having the joint bushing forcibly separate from the cross member. In order to seize the potential error when deriving the dynamic stiffness of the bushing by using FRF obtained from the assembled system,

FRFs are obtained and compared from four surrounding locations where the bushing and the cross member mounting couples. This result is plotted in Figure 5.10. The comparison results suggest that all curves are nearly identical at both the resonance and the anti-resonance regions up to the frequency range of interest. Hence, the coupling point's FRF is represented with one single FRF.

Accordingly, the derived dynamic stiffness with only one-point's FRF (Single coordinate coupling calculation) and two-point derived calculation (multi-coordinate coupling calculation) results are compared in Figure 5.11. The results show that the deviation in the derived dynamic stiffness value appears to be negligibly small. As it was seen in Figure 5.10, the FRF properties around the mount brackets do not deviate considerably. Therefore, the dynamic stiffness of the original and substituted bushing is derived using a single coordinate calculation for the final transmissibility estimation. The calculated dynamic stiffness of the original and substituted bushing results are plotted in Figure 5.12. This result shows that the modified bush increased by 45 % as compared to the original bush.

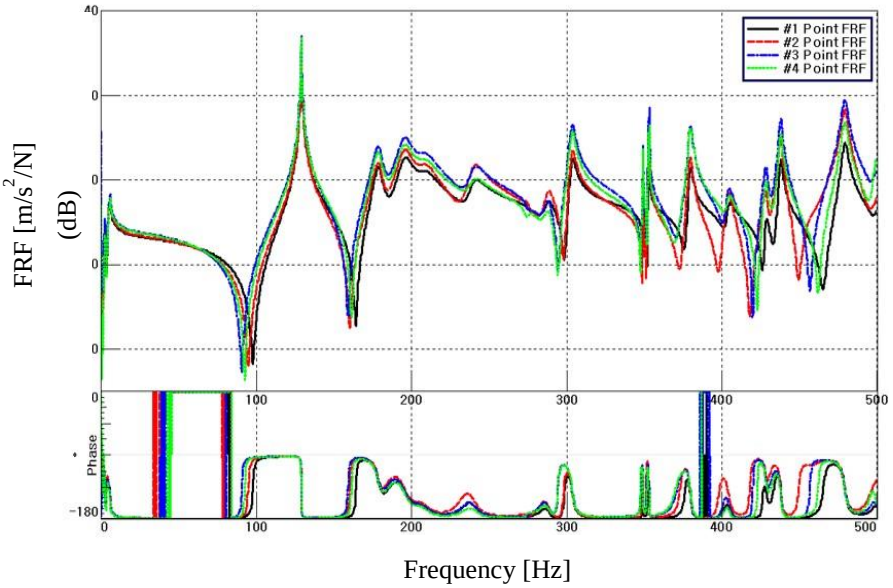

Figure 5.10　Comparison of the FRF trends at the points of the suspension bush kit depicted in Figure 5.7

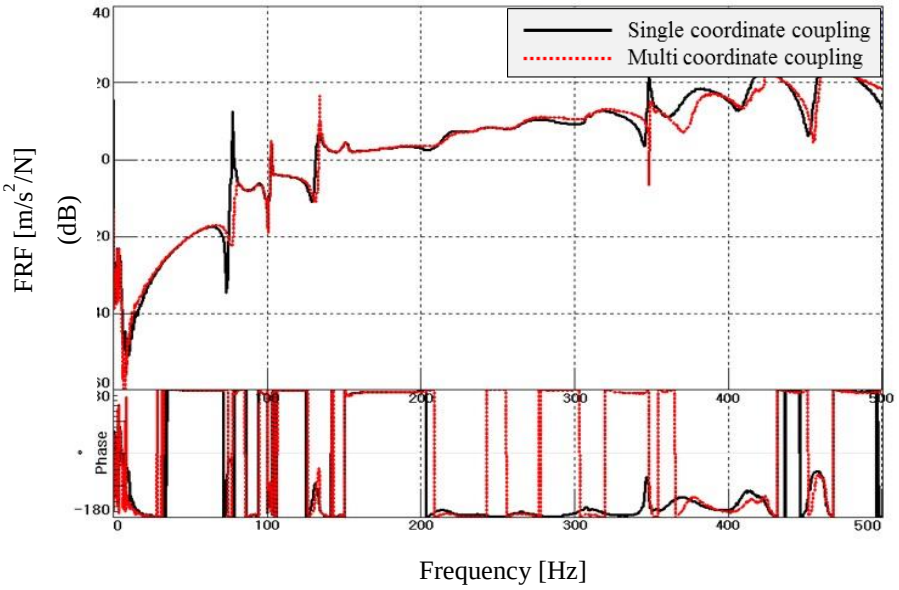

Figure 5.11 The results of bush inertance FRF calculation using the single- and multi-coordinate coupling methods (solid line: the single coordinate coupling method, dotted line: the multi-coordinate coupling method)

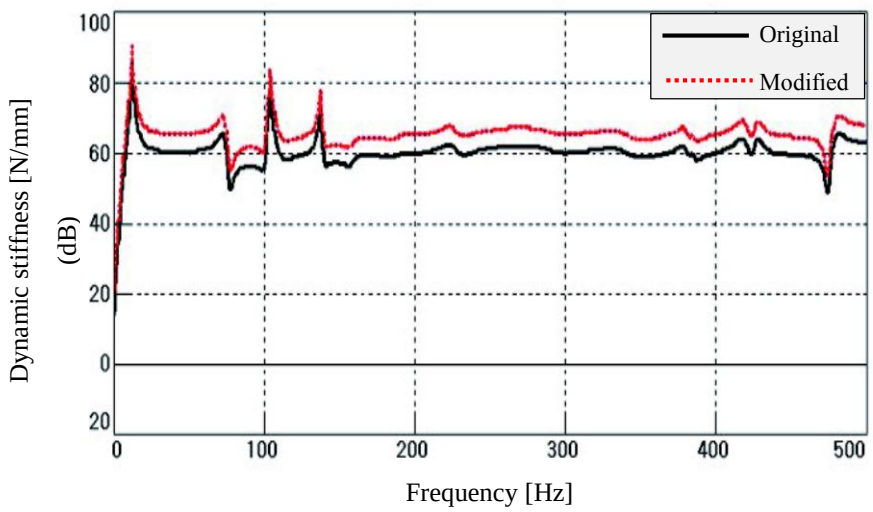

Figure 5.12 Comparison of dynamic stiffness between original and tuned bush (solid line: original bush, dotted line: modified bush)

5.5. Validation results

The calculated reaction force (with original bushing) derived using the inverse substructuring method is compared with that of the directly measured body input force in Figure 5.13.

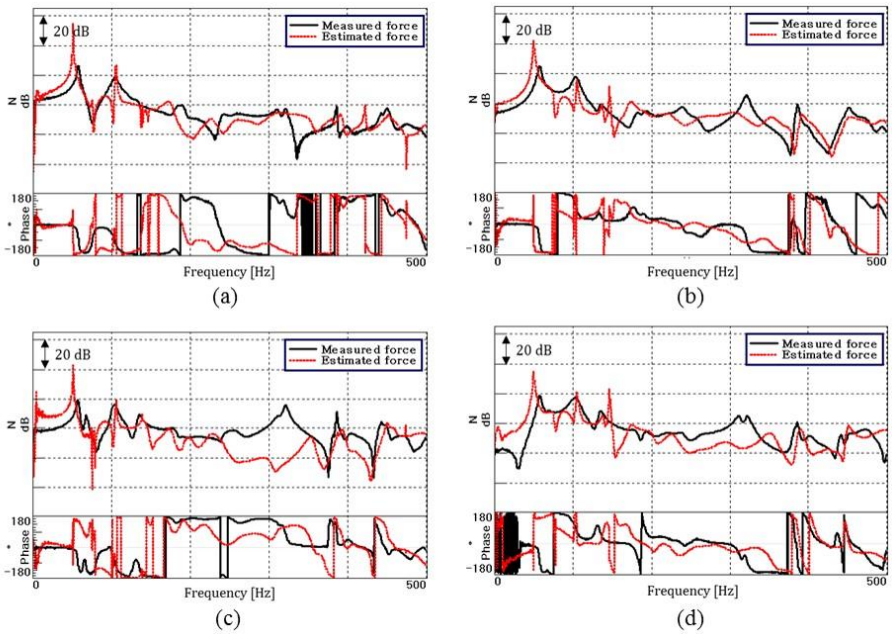

Figure 5.13 Comparison of measured force and estimated force at each mount points using cross member bush kit (solid line: measured force / dotted line: estimated force) ((a): left front mount, (b): right front mount, (c): left rear mount, (d): right rear mount)

When the stiffness of the left front mount bush increases (i.e. when $\mathbf{H}_{11}^{I}{}'$ decreases), the proportional increase of transmissibility force in the measured value and the estimated value for each frequency band becomes similar to the one shown in Figure 5.14. For intuitive comparison purposes, the x-axis frequency bands is categorized into 4: booming 1(40 ~ 100 Hz), booming 2(100~200 Hz), cavity (200~300 Hz), rumble (300~500 Hz). The results show

a very accurate force transmissibility estimation, or the ratio of change of body input force. Specifically, the changing ratio of force transmissibility at the left front mount, the point where the bush is modified, estimation accuracy was very high.

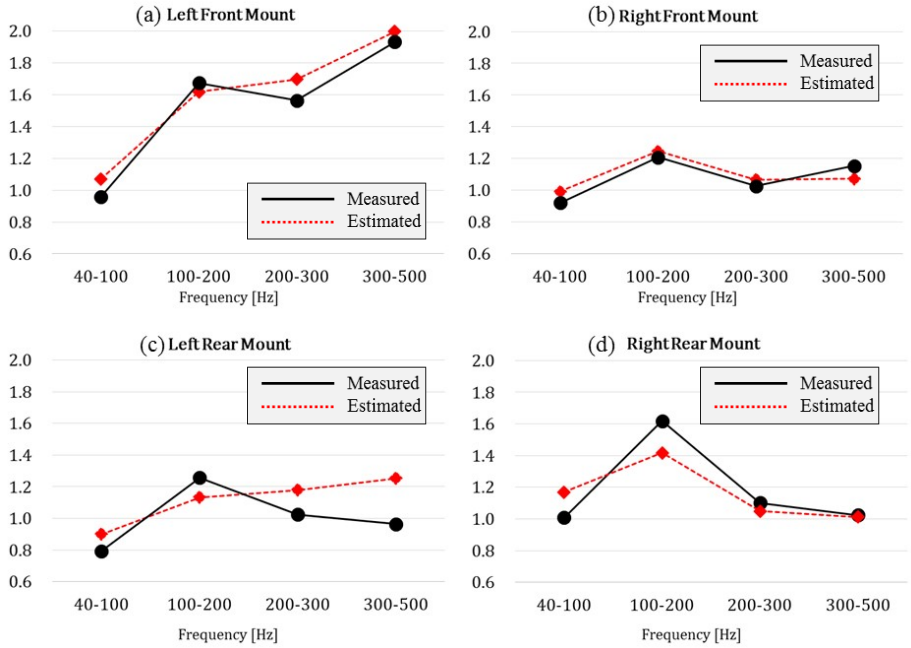

Figure 5.14 Force transmissibility at the suspension mounting points (full line: measured force transmissibility, dotted line: estimated force transmissibility)

5.6. Summary

In this chapter, the feasibility of using the inverse formulation method for deriving the road noise improvement factor on a simple cross member application is validated. For the validation test, the road excitation is simply substituted with a shaker excitation in vertical direction and a previously developed suspension rig which enables for a direct measurement of the body input force at the coupling points and a specially developed cross member jig is used for the validation test. The comparison of the estimated and directly measured body input force results shows reasonable accuracy. The transmissibility comparison between the estimated and measured values is also made for the case where one of the bushes from the cross member is modified. The high estimation accuracy in transmissibility with the modified system suggests that this model can be further extended for the actual suspension application.

CHAPTER 6

CONCLUSIONS

A special suspension rig has been developed to measure direct operational forces primarily for estimating the structure-borne cabin noise prior to the production proto vehicle. The rig has been verified by cross-referencing the knuckle acceleration spectrum measured on the baseline vehicle and the forces calculated by indirect methods up to 250 Hz. The comparison between the knuckle acceleration spectrum of the baseline vehicle and the suspension rig illustrates that the signal is almost identical in both vertical and longitudinal directions.

Directly obtained forces using the force rig are then compared to the calculated forces using two different indirect methods (dynamic stiffness and the full matrix inversion method). The results of the comparison clearly demonstrate that the forces obtained with the direct measurement method are almost identical to those obtained with the dynamic stiffness method applied on the suspension rig. When this dynamic stiffness method is applied on the baseline vehicle, some deviations are observed due to the influence of the vehicle body.

The third degree polynomial curve fitting technique is used for smoothing out the dynamic stiffness curve and peak hold technique is used for where not much deflection has occurred at the mount. Theses extracted mount dynamic stiffness values allow NVH engineers to seize improvement factors for road noise NVH performance of developing suspension and make a smarter compromise with R&H engineers possible.

In chapter 3, the precision CNC-milled road surface dyno excitation method is validated up to 500 Hz through a comparative study with actual road excitation. In addition, a coherence study has been included, as one of its intended purposes includes circumventing typical multiple coherent input problem for road noise TPA and ODS. The major conclusions drawn from this chapter are:

1) An excellent reproducibility is achieved for all measurements with the proposed detachable road shell dyno excitation method in combination with the one-point fixing device.
2) Constant speed operation on dyno with the proposed excitation method creates rippled signal due to the repeated excitation of revolution of the roller. Run up/run down operation has to be carried out in order to alleviate this phenomenon.

3) Hence, constant speed actual road measurement is compared with run-up/rundown on dyno and a significantly good match between 100 km/h actual road excitation and 20-120 km/h run-up dyno excitation is observed.

4) For smooth surface dyno excitation, 32nd dyno order dominants the excitation characteristics causing overestimation around 80 to 100 Hz. This is due to the effect of the plate bolts (2 bolts per plate and total 16 plates, which is designed to be flushed with the surface) that becomes prominent as the excitation from smooth surface is low. Yet, an excellent match is observed from 100 – 500 Hz.

5) When the rear axle is set on the smaller roller (1.68 mØ), it tends to overestimate lateral and vertical knuckle acceleration as high as up to 4 dB within 300 to 400 Hz band compared to that of the larger dyno roller (3.18 mØ).

6) Up to 400 Hz, 0.7coherence is achieved between the left and right wheel with the proposed excitation method, when the vehicle is set exactly at the center of the road profile shell for both smaller and larger rollers.

In chapter 4, a suspension coupled to a vehicle body via an elastomer is modeled by linearly connecting each component which is represented with mechanical impedance. The model is empirically validated under actual road excitation within two different suspension systems: McPherson strut type

suspensions in the lateral arm Y direction and Multilink type rear suspension in the front mount X direction. Additionally, a numerical case study is performed to investigate the potential misleading influences of using the suspension rig in relation to the full vehicle, as well as to find out the cases where the force reduction is difficult to achieve when taking 'softening the connecting bush' as a counter measuring solution. The findings from this chapter can be summarized as follows:

1) Utilizing the Thévenin's equivalent system, the excitation transmission is characterized and it is found that the achievable force reduction deviates with different combinations of all three components (chassis, bush, and body) within a system: The least force reduction is expected with a relatively stiff bush in combination with a relatively soft body, while the most force reduction is expected with a relatively soft bush and stiff body.
2) It is also found that a considerable deviation potentially occurs at a path where the chassis is connected to the body via a relatively stiff bush under rig measurement and the actual vehicle measurement due to their difference in body's dynamic stiffness.
3) It is demonstrated that substituting the knuckle's signal for the free velocity for road noise application is a valid assumption and that the

estimated force reduction with such an assumption (calculated solely in terms of the combination of parts' dynamic stiffness) shows acceptable results if the road excitation is reproducible.

4) Within an actual vehicle application, assuming that only one variable is being modified and the excitation is maintained identical, the dynamic stiffness requirement for that particular modified component can be accurately drawn by defining the desirable target force at that transfer path.

In chapter 5, the feasibility of using the inverse formulation method for deriving the road noise improvement factor on a simple cross member application is validated. For the validation test, the road excitation is simply substituted with a shaker excitation in vertical direction and a previously developed suspension rig which enables for a direct measurement of the body input force at the coupling points and a specially developed cross member jig is used for the validation test. The comparison of the estimated and directly measured body input force results shows reasonable accuracy. The transmissibility comparison between the estimated and measured values is also made for the case where one of the bushes from the cross member is modified. The high estimation accuracy in transmissibility with the modified system

suggests that this model can be further extended for the actual suspension application.

As for the future work, the feasibility of using the inverted FRF based substructuring formulation as a methodology for optimizing the joint bushing combination for enhancing vibro-acoustic performance of an actual suspension system would be desirable for consideration. Within an actual vehicle system, the boundary condition and the installation of the position of the accelerometers ought to be throughly considered and a methodology of directly installing dynamic force transducers on a vehicle system is required in order to carry out the feasibility validation experiement.

REFERENCES

1. Dobson, B. and E. Rider, A review of the indirect calculation of excitation forces from measured structural response data. *Proceedings of the Institution of Mechanical Engineers, Part C: Journal of Mechanical Engineering Science*, 1990. **204**(2): p. 69-75.

2. Thite, A. N., and D. J. Thompson. "The quantification of structure-borne transmission paths by inverse methods. Part 1: Improved singular value rejection methods."*Journal of Sound and Vibration* 264.2 (2003): 411-431.

3. Thite, A. N., and D. J. Thompson. "The quantification of structure-borne transmission paths by inverse methods. Part 2: Use of regularization techniques." *Journal of Sound and Vibration* 264.2 (2003): 433-451.

4. Plunt, Juha. "Finding and fixing vehicle NVH problems with transfer path analysis." *Sound and vibration* 39.11 (2005): 12-17.

5. Gajdatsy, P., *et al*., Application of the transmissibility concept in transfer path analysis. *Mechanical Systems and Signal Processing*, 2010. **24**(7): p. 1963-1976.

6. Douville, H., P. Masson, and A. Berry, On-resonance transmissibility methodology for quantifying the structure-borne road noise of an automotive suspension assembly. *Applied acoustics*, 2006. **67**(4): p. 358-382.

7. Elliott, A., *et al*., In-situ source path contribution analysis of structure borne road noise. *Journal of Sound and Vibration*, 2013. **332**(24): p. 6276-6295.

8. Mas, P., P. Sas, and K. Wyckaert. Indirect force determination based upon matrix inversion: A study on statistical and deterministic accuracy. In *Proceedings of the International Conference on Noise and Vibration Engineering*. 1994.

9. Kim, S. and S. Lee, Prediction of interior noise by excitation force of the powertrain based on hybrid transfer path analysis. *International Journal of Automotive Technology*, 2008. **9**(5): p. 577-583.

10. Heißing, B. and M. Ersoy, Chassis Handbook: Fundamentals, Driving Dynamics, Components, Mechatronics, Perspectives. X: *Springer Science & Business Media*, 2010.

11. Coster C, Nagahata D, (2010). ISMA 2010 - International Conference on Noise and Vibration Engineering. *On the accuracy reciprocal and direct vibro-acoustic transfer-function measurements on vehicles for lower and medium frequencies.* Interleuvenlaan 68; B-3001 Leuven, Belgium.

12. J. S. Arora, E. J. Haug, Methods of design sensitivity analysis in structural optimization, *AIAA Journal* **17** (9) (1979) 970-974.

13. Kindt P, De Coninck F, Sas P, Desmet W. Test setup for tire/road noise caused by road impact excitations: first outlines. *Proceedings of ISMA* 2006. 2006:4327-36.

14. Leister G. Fahrzeugreifen und Fahrwerkentwicklung. *Wiesbaden: Vieweg+ Teubner Verlag*. 2009.

15. Bathelt H, Kolm H, Schammer K. New road noise testing techniques. *ATZ live Automotive Acoustics Conference; Zürich Switzerland: Springer;* 2015.

16. Sandberg U, Ejsmont JA. Tyre/road noise reference book2002.

17. Zehner M. Fahrzeugfesselung auf Rollenprüfständen. *Patents;* 2006.

18. Kang YJ, Kim HS, Song DP, Min D. Dynamic behavior observations with two different methods of constraining vehicle on a chassis dynamometer. *Korean Society for Noise and Vibration Engineering*. 2014;*Transactions of the Korean Society for Noise and Vibration Engineering*:1000-3.

19. Brandt A. Noise and vibration analysis: signal analysis and experimental procedures: *John Wiley & Sons*; 2011.

20. Sakata T, Morimura H, Ide H. Effects of tire cavity resonance on vehicle road noise. *Tire Science and Technology.* 1990;18(2):68-79.

21. Zeller P. Handbuch Fahrzeugakustik. Vieweg+ Teubner, GWV Fachverlage GmbH, Wiesbaden. 2009.

22. Wang X. *Vehicle noise and vibration refinement: Elsevier;* 2010.

23. Kromulski J, Hojan E. An application of two experimental modal analysis methods for the determination of operational

deflection shapes. *Journal of Sound and Vibration.* 1996;196(4):429-38.

24. Song DP, Min D, Kang YJ, Cho M, Kim HG, Ih KD. A methodolgy for evaluating the structure-borne road noise prior to a prototype vehicle using direct force measured on a suspension rig. *Noise Control Engineering Journal.* 2016;64(3):295-304.

25. Bastow D, Howard G and Whitehead JP. *Car suspension and handling*. SAE international Warrendale, 2004.

26. Kim KC and Kim C-M. A study on the body attachment stiffness for the road noise. *Journal of Mechanical Science and Technology*. 2005; 19: 1304-12.

27. Ko K-H, Heo S-J and Kook H. Evaluation of road-induced noise of a vehicle using experimental approach. *International Journal of Automotive Technology*. 2003; 4: 21-30.

28. Kim K-C and Kim C-M. A Study on the Development of High Stiffness Body for Suspension Performance. *Transactions of the Korean Society for Noise and Vibration Engineering*. 2005; 15: 799-805.

29. Dorny CN. *Understanding dynamic systems: Approaches to modeling, analysis, and design*. Prentice Hall, 1993.

30. Reid JG. *Linear system fundamentals: continuous and discrete, classic and modern*. McGraw-Hill College, 1983.

31. K Shearer JL, Murphy AT and Richardson HH. *Introduction to system dynamics*. Addison-Wesley Reading, 1967.

32. Hynna P, Klinge P and Vuoksinen J. Prediction of structure-borne sound transmission in large welded ship structures using statistical energy analysis. *Journal of sound and vibration*. 1995; 180: 583-607.

33. Kubota Y. Asymptotic modal analysis and statistical energy analysis of dynamical systems. *Journal of applied mechanics*. 1985; 52: 949.

34. Otte D, Leuridan J, Grangier H and Aquilina R. Coupling of structures using measured FRF's by means of SVD-based data reduction techniques. *Proc of 8th IMAC*. 1990, p. 213-20.

35. Otte D, Leuridan J, Grangier H and Aquilina R. Prediction of the dynamics of structural assemblies using measured FRF-data: some improved data enhancement techniques. *Proceedings of the Ninth International Modal Analysis Conference*. London, 1991, p. 909-18.

36. Zhen J, Lim TC and Lu G. Determination of system vibratory response characteristics applying a spectral-based inverse sub-structuring approach. Part I: analytical formulation. *International Journal of Vehicle Noise and Vibration*. 2004; 1: 1-30.

37. Kang, Yeon June, et al. "Experimental evaluation of direct measurement for excitation forces acting on the hard-points of suspension system to predict road-noise performance."

Transactions of the Korean Society for Noise and Vibration Engineering 25.3 (2015): 184-190.

38. Tsai, J-S., and Y-F. Chou. "The identification of dynamic characteristics of a single bolt joint." *Journal of Sound and Vibration* 125.3 (1988): 487-502.

39. Zhen, Jiantie, Teik C. Lim, and Guangqing Lu. "Determination of system vibratory response characteristics applying a spectral-based inverse sub-structuring approach. Part I: analytical formulation." *International Journal of Vehicle Noise and Vibration* 1.1-2 (2004).

40. Lee, D-H., W-S. Hwang, and C-M. Kim. "Design sensitivity analysis and optimization of an engine mount system using an FRF-based substructuring method." *Journal of Sound and Vibration* 255.2 (2002): 383-397.

41. Guyan, Robert J. "Reduction of stiffness and mass matrices." *AIAA journal* 3.2 (1965): 380.

APPENDIX

FORMULATION FOR PIVOT POINT ROTATIONAL INFLUENCE

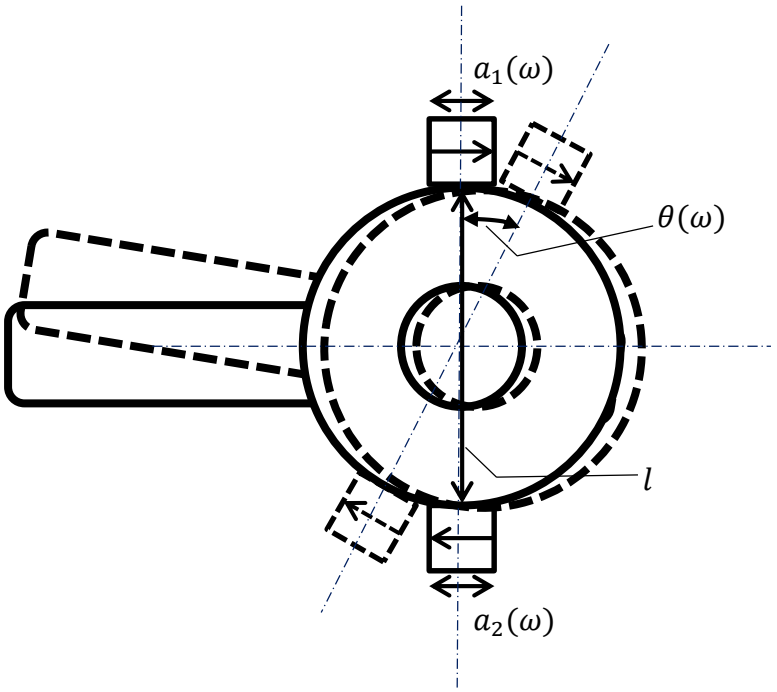

$a_1(\omega)$ acceleration obtained from the top pivot point

$a_2(\omega)$ acceleration obtained from the bottom pivot point

$a_r(\omega)$ rotational acceleration

$a_t(\omega)$ translational acceleration

$k_{\theta(\omega)}$	the rotational stiffness of the pivot system
l	the length between the top and bottom accelerometer
$\mathrm{M}(\omega)$	the moment created at pivot point
$\ddot{\theta}(\omega)$	the angular acceleration due to rotation
$\theta(\omega)$	the angular displacement due to rotation

The moment exerted to the body due to rotational movement on the pivot point of the link is

$$\mathrm{M}(\omega) = k_{\theta(\omega)}\theta(\omega). \quad (1)$$

The rotational component is calculated by adding two acceleration signals obtained from off centered accelerometers positioned as it is shown from above figure. First, the translational acceleration component is seperated and subtracted from the origianl signal

$$\{a_1(\omega) + a_2(\omega)\}/2 = a_t(\omega), \quad (2)$$

$$a_r(\omega) = a_1(\omega) - a_t(\omega). \quad (3)$$

The angular acceleration is then,

$$\ddot{\theta}(\omega) = \frac{2}{l} a_r(\omega). \quad (4)$$

By double integrating, the angular displacement can be estimated

$$\theta(\omega) = \ddot{\theta}(\omega)/-\omega^2. \quad (5)$$

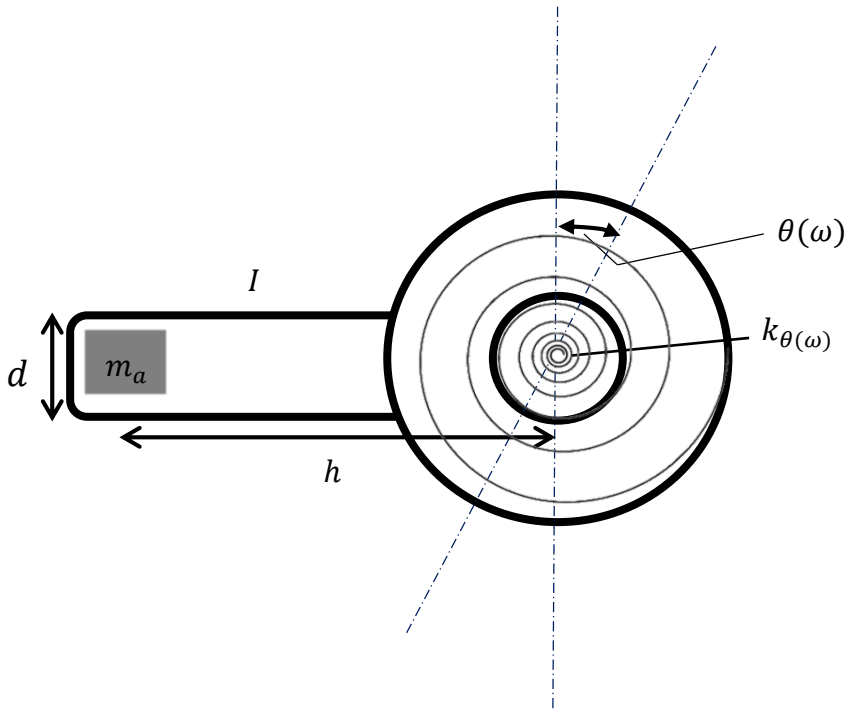

d	the diameter of solid cylinder bar link
$\mathrm{F}(\omega)$	force applied to the system
h	the distance between the center of the pivot point and additional mass
I	the moment of inertia of the pivot system
m_a	additional mass for shifting the system's resonance frequency
ω_{o_n}	the natural frequency of the original pivot system
ω_{a_n}	the natural frequency of the pivot system with added mass

The rotational stiffness is drived from the equation of motion

$$I\ddot{\theta} + k_\theta \theta = M, \tag{6}$$

The rotational stiffness can be expressed as follows

$$k_\theta = I\omega_{o\_n}^2. \tag{7}$$

The moment of inertia is derived usintg the additional mass and resonance shift relations

$$I = \frac{m_a h^2}{\omega_{o\_n}^2/\omega_{a\_n}^2 - 1}. \tag{8}$$

The requirement for choosing m_a, the moment of inertia created by the additional mass needs to be larger than the polar moment of inertia for the link (solid cylinldrical bar)

$$\frac{m_a h^2}{\omega_{o\_n}^2/\omega_{a\_n}^2 - 1} > \frac{\pi d^2}{32}. \tag{9}$$

The rotatioanl stiffness term (eq. 7) can be rewritten as

$$k_\theta = \frac{m_a h^2}{\omega_{o\_n}^2/\omega_{a\_n}^2 - 1}\omega_{o\_n}^2. \tag{10}$$

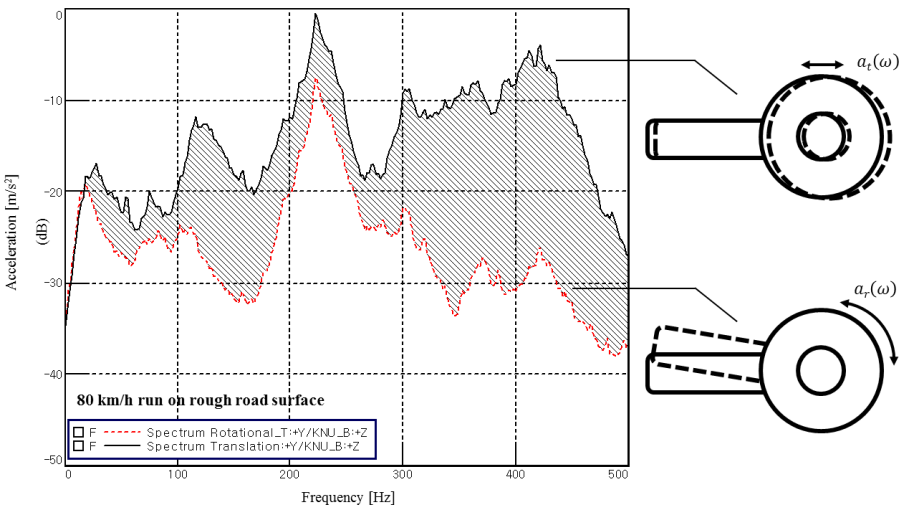

The rotational influence observed from the passive side can be obtained by using two synchronized shaker with in-phase excitation. The figure down below.

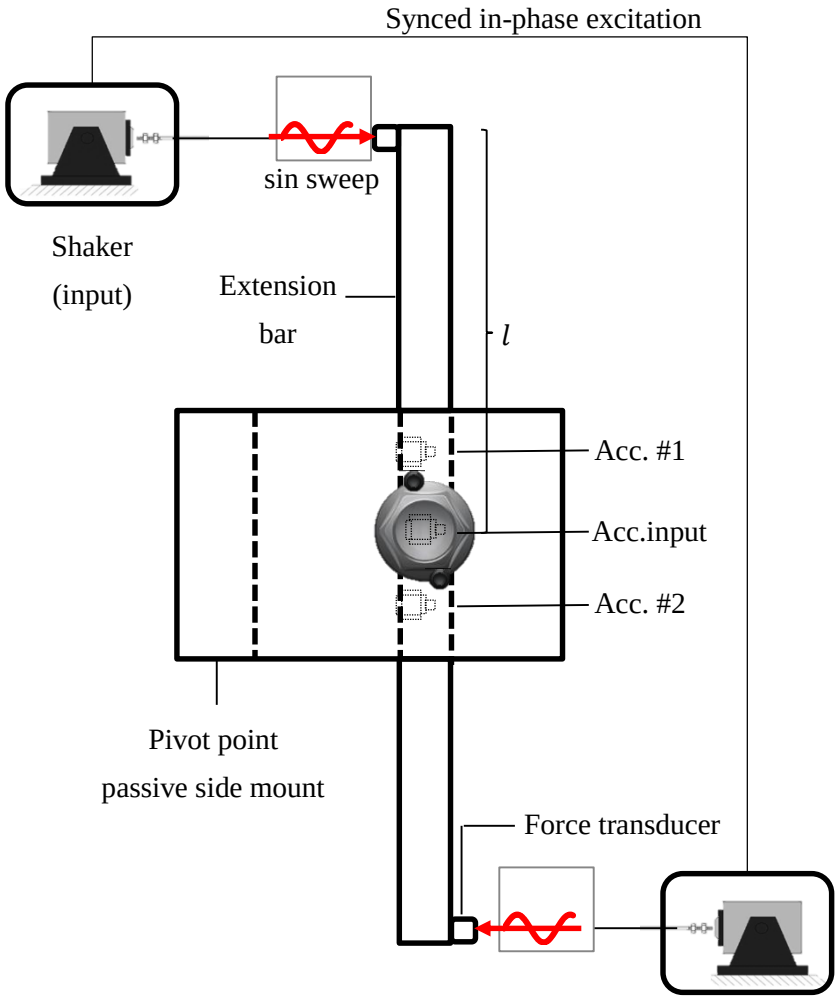

Torsional Input Point Inertance (TIPI) due to exerted moment is expressed as

$$\text{TIPI} = \frac{a_{input}(\omega) - \{(a_1(\omega) + a_2(\omega))/2\}}{2 * (\text{F}(\omega) * l)}. \qquad (11)$$

국 문 초 록

기존 전달 경로 분석 법을 이용한 로드 노이즈 성능 평가에서는 주행 중 차체 전달 힘을 주파수 응답 함수와 주행 중 가속도 값을 이용하여 계산하게 된다. 또한, 로드 노이즈 성능에 차체와 서스펜션 각각이 미치는 영향을 파악하기 어렵다. 본 논문에서는 직접적으로 서스펜션으로부터 차체로 전달되는 포스를 측정함으로써 구조기인 로드노이즈 성능을 평가할 수 있는 리그를 제작하여 새로운 평가 및 개선 방안 도출 방법을 연구하였다. 마운팅 체결부의 강성평가 및 ODS 분석, 절연 성능 평가 및 무게와 댐핑 영향을 평가하여 리그를 검증하였고, 동강성 법과 역행렬 법을 이용하여 계산된 포스와의 비교를 통해 차체의 이펙트와 계산으로부터 야기 될 수 있는 오차를 확인하였다. 실 도로 노면 가진을 재현하기 위한 다이노 롤러를 이용한 가진 방법 및 신호처리 방법이 연구되었고 서스펜션 벤치마킹 분석법을 적립하였다. 또한, 임피던스 모델링 방법과 역 부분 구조 합성법을 이용하여 절연 고무의 개선인자 선정 방법 및 정량적인 동특성 제안 방법론을 적립하였다. 제안된 방법을 실 차량 개발에서의 부시 변경 시나리오에 적용함으로써 연구의 유효성과 신뢰성을 확인하였다.

주요어 : 구조기인 로드노이즈, 전달 경로 분석, 서스펜션 모듈평가 리그, 임피던스 방법, 다이노 가진, FRF 기반 하위 구조 역 배합 방법

학 번 : 2014-30338